

Understanding the variation of Reflected Solar Radiation: A Latitude- and month-based Perspective

Ruixue Li¹, Bida Jian¹, Jiming Li¹, Deyu Wen¹, Lijie Zhang¹, [Yang Wang¹](#), [Yuan Wang¹](#)

5 ¹Key Laboratory for Semi-Arid Climate Change of the Ministry of Education, College of Atmospheric Sciences, Lanzhou University, Lanzhou 730000, China

Correspondence to: Bida Jian (jianbd16@lzu.edu.cn) and Jiming Li (lijiming@lzu.edu.cn)

Abstract. ~~The hemispheric symmetry of planetary albedo (PA) is crucial for the Earth's energy budget. However, our understanding of hemispheric albedo is still limited, particularly regarding its variations at finer spatial and temporal scales. Using 21 years of radiation data from CERES EBAF, this study quantifies the contribution rates of different latitudes to the hemispheric reflected solar radiation and examines their seasonal variations. Statistical results show that the northern latitudinal zones of 0° to 40° contribute more reflected radiation than the corresponding southern latitudes, but the southern latitudinal zones of 50° to 90° compensate for this. From the equator to 40°, the latitudinal contribution to the hemisphere is high in autumn and winter and low in spring and summer; however, after 50°, the situation is reversed. And even during extreme cases, anomalies of the cloud component contribution play a dominant role in anomalies of the total reflected radiation contribution of the latitudinal zone in most latitudinal zones. Additionally, this study evaluates the performance of four radiation data (including: satellite and reanalysis data) in reproducing hemisphere albedo and its hemispheric symmetry compared to CERES EBAF data. Under different symmetry criteria, the applicability of different datasets to hemispheric symmetry of PA studies varies. Note that the Cloud_cci AVHRR performs better in capturing hemispheric symmetry. However, none of these datasets can decompose the different components of reflected radiation well. These results contribute to advancing our understanding of hemispheric symmetry variations and compensation mechanisms, reducing the uncertainty of model simulations, and improving algorithms for different radiation datasets.~~
Hemispheric and interannual variations of reflected solar radiation (RSR) may mask the inter-month and region-specific signals, limiting the investigation of spatiotemporal mechanisms and hemispheric symmetry projections. This drives us to explain RSR characteristics from latitude- and month-based perspectives. The study also attempts to reproduce hemispheric symmetry of RSR using longer-record radiation datasets to understand

30 its temporal changes. Statistics indicate that the largest decreasing trends in Northern and Southern
Hemispheres (NH and SH) occur in mid-spring and are dominated by (clear-sky atmospheric and cloud
components), and cloud component only, respectively. The interannual negative trend in NH mainly
derived from 30°-50°N latitude zones, attributed to decrease in clear-sky atmospheric component caused
35 fraction caused by increased sea surface temperature and unstable marine boundary layer, leading to
reduced cloud component. In SH, the significant decreasing trend is widespread in 0°-50°S latitude zones,
closely related to the decrease in cloud component caused by the decrease in cloud cover over the tropical
western Pacific and Southern Ocean, partially compensated by the increase in clear-sky atmospheric
component. A new data evaluation system and uncertainty analysis reveal that only AVHRR outperforms
40 in reproducing hemispheric differences of RSR due to offsetting biases among different components, and
achieves hemispheric RSR symmetry criteria within its uncertainty, making it suitable for studying long-
term RSR hemispheric symmetry changes. Furthermore, ISCCP reproduces hemispheric asymmetry of
cloud component well and can help to study the corresponding long-term changes and mechanisms.

45 **1 Introduction**

Planetary albedo (PA) refers to the fraction of incoming solar radiation that is reflected back into space by the Earth's atmosphere, clouds, and surface. It plays a crucial role in regulating the Earth's energy budget and global climate change (Wielicki et al., 2005; Stephens et al., 2015) by determining the amount of solar energy absorbed and distributed ~~throughout by~~ the Earth-atmosphere system (Fu et al., 50 2000; Stephens et al., 2015). Studies have shown that a 5% change in PA can lead to an average global temperature change of approximately 1K (North et al., 1981), while a 0.01 change in PA can have a radiative forcing effect equivalent to carbon dioxide doubling ~~the amount of carbon dioxide~~ in the atmosphere (Wielicki et al., 2005; Bender et al., 2006). Even small variations in PA ~~could be sufficient to~~
~~have significant implications~~ for the development of Quaternary glaciations (Budyko, 1969). Therefore,
55 it is crucial to quantify the basic statistical properties of PA, ~~as well as understand and clarify~~ the major principles ~~and mechanisms~~ governing its spatial-temporal changes and long-term trends at various scales, including annual, global, and even finer spatial-temporal scales (e.g., regional and monthly scales).

Nowadays, satellite data and model simulations have been widely ~~used~~ utilized to investigate the climatology (George and Bjorn, 2021; Jönsson and Bender, 2022), spatial and temporal distribution characteristics (Loeb et al., 2007; Pang et al., 2022), and long-term trends of PA (Diamond et al., 2022; Stephens et al., 2022; Xiao et al., 2023), as well as the contributions of different components (~~e.g., such as~~ cloud, clear-sky atmosphere, and surface) to PA (Stephens et al., 2015; Jönsson and Bender, 2022). Long-term satellite records have indicated that the current PA maintains a relatively stable value of approximately 0.29 (Bender et al., 2006). Surprisingly, the annual mean reflected solar radiation (RSR) in the Northern Hemisphere (NH) and Southern Hemisphere (SH) is ~~nearly the~~ almost same within measurement uncertainty, which is referred to as hemispheric symmetry (Loeb et al., 2009; Voigt et al., 2013; Stephens et al., 2015; Jönsson and Bender, 2022). However, although satellite observations have demonstrated the symmetry of hemispheric PA-RSR on inter-annual scales, state-of-the-art models still struggle to reproduce this essential feature due to inadequate representation of the underlying physical mechanisms for PA-RSR variation, particularly the poor modeling of compensatory effects of asymmetric clouds (Voigt et al., 2013; Stephens et al., 2015; Jönsson and Bender, 2022). As a result, mean hemispheric asymmetries persist in all-sky reflections from CMIP phase 3 to CMIP phase 6, with considerable spread among the General Circulation Models (GCMs) within each CMIP phase (Crueger et al., 2023). Additionally, models also fail to capture the observed decreasing trend in ~~reflected shortwave radiation~~ RSR in both hemispheres. These limitations may stem from the inability of models to accurately simulate the components of PA-RSR and their respective contributions to the hemispheric symmetry of RSR/PA. In ~~fact~~ particular, the annual mean RSR/reflected solar radiation at the hemispheric scale is ~~comprised~~ consisted of the RSR/reflected radiation at finer spatial and temporal scales (such as regional and monthly scales). But, those signals of latitudinal and monthly variations are easily masked by studies at hemispheric or annual scales. It means that if models cannot accurately ~~account~~ simulate ~~for~~ the contribution of each component to hemispheric albedo/RSR at finer temporal and spatial scales, it will be bound to limit our ability in ~~it hinders our ability to~~ identifying potential regional maintenance or compensation mechanisms for hemispheric symmetry in PA-RSR. Finally/Furthermore, above RSR bias at finer temporal and spatial scales will exacerbate the ~~it introduces significant~~ uncertainties in model simulations of RSR/PA at annual and hemispheric scales.

Indeed, decomposing the hemispheric annual RSR to finer spatial and temporal scales can help to

identify the regional-scale influence and maintenance mechanism for hemispheric symmetry of RSR and further improve the model simulation of the radiative fluxes. Previous numerous studies have already demonstrated the importance of the regional compensation and influencing mechanism maintaining the hemispheric symmetry. Indeed, the contributions of different latitudinal zones to PA vary significantly spatially and temporally due to variations in water vapor, aerosols, vegetation, and clouds (Hu and Stamnes, 1993; Loeb et al., 2007; Voigt et al., 2014; Letu et al., 2018; Li et al., 2018; Zhao et al., 2019; Yang et al., 2020). These changes in contribution are also influenced by local climate and large scale circulation patterns. For example, as one of the important conjectures of the compensating mechanism for the hemispheric symmetry of PA (Voigt et al., 2013; Voigt et al., 2014; Stephens et al., 2015), the Intertropical Convergence Zone (ITCZ) plays an important role in regulating cloudiness in the 10°S-10°N region, with its location and intensity varying seasonally (Waliser and Gautier, 1993; Hu et al., 2007). Based on the hemispheric-scale model simulations, early study conjectured that the ITCZ is the important compensating mechanism for the hemispheric symmetry of RSR by shifting it towards the darker surface hemisphere (Voigt et al., 2014). However, the presence of tropical clouds alone may not be the primary factor compensating for the determining hemispheric albedo asymmetry of RSR, because the NH not only has the higher clear-sky albedo, but also the maximum tropical cloudiness as the maximum in tropical cloudiness is located in the NH along with higher contributions from the surface and clear sky atmosphere of the NH (Jönsson and Bender, 2023). Nevertheless, based on finer temporal scales (such as monthly-scale) studies, it was found that variations in tropical clouds, especially those associated with the nonneutral phases of El Niño–Southern Oscillation (ENSO), are critical in regulating the asymmetry of hemispheric RSR (Jönsson and Bender, 2022). This suggests the importance of examining mechanisms influencing and maintaining hemispheric symmetry on finer spatial and temporal scales. However, the presence of tropical clouds alone may not be the primary factor determining hemispheric albedo symmetry, as the maximum in tropical cloudiness is located in the NH along with higher contributions from the surface and clear sky atmosphere of the NH (Jönsson and Bender, 2023). Furthermore, instead, extra-tropical cloudiness, particularly in the SH, has been highlighted as an important factor in maintaining the symmetry of the annual mean hemispheric albedo (George and Bjorn, 2021; Rugenstein and Hakuba, 2023). Recent-In addition, recent studies have emphasized the impact of the distinct land-sea distribution between hemispheres, which leads to enhanced baroclinic activities

~~oblique pressure activity~~ at mid-latitudes in the SH, [resulting in an increase in baroclinic synoptic systems](#) (Hadas et al., 2023). This activity results in intensified storm tracks, increased cloud cover, and higher cloud albedo in the extratropical regions of the SH (George and Bjorn, 2021). These clouds effectively compensate for the ~~asymmetries~~ [asymmetry](#) in clear-sky albedo between the NH and SH. The [baroclinic activity](#)~~oblique pressure activity~~ at mid-latitudes exhibits a distinct seasonal cycle, with winter storm tracks in the NH being almost three times longer than summer storm tracks, and seasonal meridional shifts occurring in the SH (Verlinden et al., 2011). [Besides, regional volcanic eruptions and forest fires also significantly affect local atmospheric transmissivity and underlying surface albedo, even affect the albedo of polar snow cover remotely \(Cole-Dai, 2010; Pu et al., 2021\). These events typically occur during the summer and autumn \(Fan et al., 2023\) in certain regions, but they have significant impacts on the interannual hemispheric symmetry of RSR.](#)

~~In particular, It is important to note~~ that the contributions of different latitudinal zones to hemispheric ~~PA-RSR~~ are not independent of each other. ~~Changes-Variations~~ in the contributions of different latitudinal zones can offset or amplify each other, resulting in an energy balance or imbalance between the two hemispheres ([hemispheric symmetry or asymmetry](#)). For example, anthropogenic emissions from Asia not only enhance the local clear-sky atmospheric component of ~~reflected radiation~~[RSR](#) through direct aerosol effects but also significantly increase aerosol optical thickness in the northwestern Pacific through long-range transport. This, in turn, increases the amount of deep convective clouds due to the indirect effects of aerosols ([Zhang et al., 2007; Wang et al., 2014](#)). The increased deep convective clouds can strengthen the storm track in the Pacific Ocean and increase the contribution of the cloud component (Wang et al., 2014). [However, most of these studies are based on specific regions or components. Systematic studies on the distribution and changes of RSR and its components at finer temporal and spatial scales have received far less attention.](#) Therefore, a comprehensive analysis of the contributions of different components at different latitudes and their monthly variations would help to better understand the mechanism of hemispheric ~~PA-RSR~~ symmetry and reduce uncertainties in model simulations of ~~PARSR~~.

Currently, satellite remote sensing products from the CERES mission, which are based on broad-band measurements, are invaluable for studying the energy balance of the Earth-atmosphere system (including changes in [RSR PA](#) and hemispheric symmetry) and climate change (Loeb et al., 2018b). [In](#)

145 [fact, researchers are still debating whether the hemispheric symmetry of RSR is an incidental outcome](#)
[or an inherent feature of the Earth-atmosphere system. Based on CERES observations, a recent study](#)
[found a decreasing trend in RSR in both hemispheres, while the hemispheric differences in RSR have](#)
[not significantly changed \(Jönsson and Bender, 2022\), indicating that the hemispheric symmetry remains](#)
[robust. Rugenstein and Hakuba \(2023\) suggested that hemispheric symmetry is a characteristic of the](#)
150 [current climate state and will be disrupted in future scenarios. However, the CERES observational record](#)
[is relatively limited \(2000-present\), we cannot determine how hemispheric symmetry changes over time.](#)
[Therefore, there is an urgent need for us to use longer and more reliable radiation records to verify the](#)
[symmetry feature and find out the potential maintenance or compensation mechanisms of RSR symmetry.](#)
~~[However, the relatively limited observation record of CERES \(2000-present\) makes it challenging to](#)~~
155 ~~[study hemispheric PA symmetry on longer time scales.](#)~~ In recent years, satellite radiometric products and
reanalysis data with longer time coverage and finer spatial resolution have been released, and numerous
assessments have been conducted by researchers (Cao et al., 2016; Schmeisser et al., 2018; Loeb et al.,
2022). The Cloud_cci version 3 radiative flux dataset has been shown to be in good agreement with the
CERES EBAF dataset at a global scale (Stengel et al., 2020). Zhao et al. (2022) systematically assessed
160 the applicability and accuracy of the Cloud_cci radiative flux dataset over the Tibetan Plateau (TP) and
found that although the AVHRR can better describe the spatial and temporal characteristics of top-of-
atmosphere (TOA) radiative fluxes over the TP, it does not capture the long-term trend of cloud radiative
effects well. Furthermore, the spatial and temporal distributions of global TOA reflected [solar](#)
[radiation](#)~~[radiance](#)~~ from MERRA-2 and ERA5 have been compared with those from CERES (Lim et al.,
165 2021), revealing that ERA5 shows better agreement with CERES than MERRA-2 in terms of seasonal
fluxes. However, most of these assessments focus on the spatial and temporal reproducibility of these
data in terms of global or regional radiative flux, while their performance in terms of hemispheric
symmetry remains unknown. To understand the mechanisms maintaining hemispheric symmetry of
[RSRPA](#) on longer time scales, it is essential to systematically ~~[quantify evaluate](#)~~ the ~~[performance usability](#)~~
170 of long-term radiative flux products in describing interhemispheric differences in TOA ~~[reflected radiation](#)~~
[RSR](#) and its components [at hemispheric and finer temporal-spatial scales. Additionally, identifying](#)
[deficiencies and gaps between the datasets can provide a reference basis for improving algorithms and](#)
[parameterizations of radiation.](#)

To enhance future investigations into the potential maintenance mechanisms of hemispheric symmetry and to reduce uncertainties in model simulations, this study aims to ~~use~~ utilize long-term satellite observations of radiative flux (e.g., CERES-EBAF ed4.2) to quantify the contributions of clear-sky atmospheric, surface, and cloud components to ~~PA-RSR~~ at finer spatial-temporal scales (e.g., regional and monthly scales). Additionally, we aim to analyze the spatial-temporal variability characteristics of these contributions. ~~Furthermore, we will examine the variation of controlling factors in extreme anomaly years of reflective radiation contribution at different latitudes. Furthermore~~In particular, we will comprehensively evaluate the ~~performance reproducibility of various satellite and reanalyzed radiation datasets (including Cloud cci AVHRR PM v3, ISCCP-FH, MERRA-2, and ERA5) in reproducing hemispheric differences and symmetry of CERES observed RSR and its components at hemispheric and finer temporal-spatial scales. inter-hemispheric reflected radiation and its components using various satellite and reanalyzed radiation datasets (including Cloud_cci AVHRR PM v3, ISCCP FH, MERRA-2, and ERA5), with a focus on comparing them to CERES EBAF radiation products.~~ The paper is structured as follows: Section 2 describes the data and methods used in the study; Section 3 presents the overall characterization ~~(including: average and variability of RSR at different spatial and temporal scales, latitudinal zone distribution, seasonal variations), and driving factors of reflected radiative flux and its components in extreme anomaly years,~~ as well as the ~~systematic~~ assessment of different radiation datasets; and finally, Section 4 provides the conclusions ~~and discussion.~~

2 Datasets and Methodology

2.1 Datasets

2.1.1 CERES ~~EBAF and MODIS~~

The Terra and Aqua satellites of the NASA were launched into Earth orbit in 1999 and 2002, respectively. Here, we use the products from ~~two instruments (Clouds and the Earth's Radiant Energy System (CERES) instrument and Moderate-Resolution Imaging Spectroradiometer (MODIS))~~ flying on both the Terra and Aqua satellites to provide the monthly mean radiative flux, ~~cloud properties and parameters of the underlying surface.~~

CERES ~~utilizes~~ provides satellite-based observations to measure the Earth's radiation budget and clouds (Wielicki et al., 1996; Loeb et al., 2018b). The CERES instrument is a scanning broadband

radiometer that ~~provide captures~~ radiation data across three channels: the shortwave channel (0.3–5 μ m), the infrared window channel (8–12 μ m), and the total channel (0.3–200 μ m). ~~In our study, we focus on filtered radiances within the shortwave spectrum (0.3–5 μ m). The radiance received by the CERES instrument is first converted from digital counts to calibrated "filtered" radiances. This is then These radiances are first~~ converted to unfiltered radiances ~~to correct for imperfections in the spectral response of the instrument~~ (Loeb et al., 2001), and then transformed into TOA ~~instantaneous radiation radiative fluxes~~ using an empirical angular distribution model (Su et al., 2015). Instantaneous fluxes are converted to daily-averaged fluxes using sun-angle dependent diurnal albedo models (Loeb et al., 2018b). Surface irradiances are independently calculated using aerosols, clouds, and thermodynamic properties derived from satellite observations and reanalysis products. These calculations are constrained by the TOA irradiance (Kato et al., 2013; Kato et al., 2018).

~~Based on the work of~~Following Stephens et al. (2015) and Jönsson and Bender (2022), ~~we have the study selected chooses~~ the TOA and surface shortwave (SW) radiative fluxes from the CERES ~~EBAF~~Energy Balanced and Filled (EBAF) product to analyze the contributions of different components. The CERES EBAF product employs an objectively constrained algorithm (Loeb et al., 2009) that adjusts the TOA SW and longwave (LW) fluxes within their uncertainties to ~~eliminate remove~~ inconsistencies between the global mean net TOA fluxes and the heat storage in the Earth-atmosphere system (Johnson et al., 2016). We use CERES EBAF, edition 4.2 (Loeb et al., 2018b), for monthly mean radiative fluxes (incoming solar radiation, upwelling SW radiation at TOA, and both upwelling and downwelling SW radiation at the surface) during all-sky and clear-sky conditions between March 2001 and February 2022 (21 years) on a 1 $^{\circ}$ ×1 $^{\circ}$ resolution grid. Note that EBAF data prior to June 2002 are Terra records only. In order to minimize flux discontinuities between the Terra-only record and the Terra&Aqua record, the CERES EBAF Ed4.2 product applies regional climate adjustments to the Terra-only record.

~~The cloud property parameters (Cloud Fraction (CF), Cloud Visible Optical Depth (CVOD), Ice Water Path (IWP) and Liquid Water Path (LWP)) for this study from March 2001 to February 2022 are obtained from CERES_SSF1deg_Ed4.1. This product provides MODIS derived cloud properties and auxiliary data from the observed transient footprint SSF Ed4A fluxes and clouds (Minnis et al., 2020). Daytime cloud properties are calculated from the MODIS visible and infrared channels. To keep consistency with the EBAF data and to minimize the errors due to the diurnal cycle of clouds, we have~~

235 averaged the cloud properties data from the Terra and Aqua sources over their overlapped time period (2002.7-2022.2). However, since Aqua data are not available prior to July 2002, this may result in a little bit uncertainty. In addition, the Ice/snow Coverage (ISC) data of CERES SSF is also used in this study. Snow and ice daily coverage is derived from the NSIDC (National Snow and Ice Data Center) near real-time SSM/I SSMIS EASE Grid Daily Global Ice Concentration and Snow Extent products, which are then interpolated to monthly average products.

240 In addition to snow and ice coverage, local vegetation coverage is also one of the important factors to influence the change of land surface albedo (Betts, 2000; Sandholt et al., 2002). To indicate vegetation greenness, the Normalized Difference Vegetation Index (NDVI) used in this study is the Terra MODIS NDVI 0.05 degree monthly product (MOD13C2-collection061), which is based on spatial and temporal averages of 16-day 1-kilometre NDVI. The NDVI is calculated as the ratio between TOA reflectance of a red band around 0.66 μm and a near-infrared (NIR) band around 0.86 μm . In general, higher values of NDVI indicate a higher density of green vegetation.

2.1.2 ISCCP-FH

245 The International Satellite Cloud Climatology Project (ISCCP) aims to provide global cloud coverage and cloud radiation characteristics (Schiffer and Rossow, 1983). As part of the ISCCP project, the ISCCP-FH radiation product contains SW radiation fluxes at five levels from the surface to the TOA (surface-680hPa-440hPa-100hPa-TOA) under all-sky, clear-sky and overcast-sky conditions as well as the diffuse and direct SW fluxes at the surface. ISCCP-FH is not produced using direct instrumental
250 observations, but rather the ISCCP H series of data products that are derived from geostationary and polar-orbiting satellites (Young et al., 2018), adopting a complete radiative transfer model developed from the GISS GCM ModelE. As a third-generation product, ISCCP-H has become more advanced and has other improvements in radiation quality control, calibration, cloud detection (especially high clouds, thin clouds and polar clouds), cloud and surface properties retrievals (Zhang et al., 2023). The ISCCP-FH product consists of five sub-products, of which the PRF (surface-to-TOA flux profile) sub-product
255 can provide 34 years of global radiative flux data from July 1983 to June 2017 with a spatial resolution of up to 1° and a temporal resolution of 3 hours. In order to be consistent with CERES EBAF data, this study uses the diurnal mean of monthly mean of 3-hour upward and downward SW radiative flux at the TOA and surface under all-sky and clear-sky conditions provided by the MPF (monthly average of PRF)

260 sub-product.—

2.1.3 AVHRR

The Cloud_cci project ~~is part of~~ covers the cloud component of the European Space Agency (ESA) Climate Change Initiative (CCI) program and ~~aims to provide~~ has generated a long-term and consistent cloud property dataset (Hollmann et al., 2013). The Cloud_cci dataset is ~~generated using~~ based on the state-of-the-art retrieval system called "the Community Cloud retrieval for Climate" (CC4CL), which employs optimal estimation (OE) techniques and is applied to passive imaging sensors from current and past European and non-European satellite missions (Sus et al., 2018). ~~In our study, we have chosen~~ The Cloud_cci AVHRR-PMv3 dataset, which ~~offers~~ contains comprehensive cloud and ~~radiation radiative~~ flux properties ~~on a global scale~~ ly from 1982 to 2016, is chosen for the comparison with CERES EBAF.
270 These properties are ~~retrieved~~ derived from measurements obtained by the Advanced Very High Resolution Radiometer (AVHRR) instrument onboard the afternoon (PM) satellite of the US National Oceanic and Atmospheric Administration's (NOAA) Polar Operational Environmental Satellite (POES) mission (Stengel et al., 2020). To account for the diurnal cycle of the solar zenith angle, all samples of the SW flux are rescaled and averaged to represent a 24-hour average for each pixel. ~~This~~ The monthly average value is then determined (More details can be found in ESA Cloud_cci Algorithm Theoretical
275 Baseline Document v6.2). ~~It is important to note~~ that the radiation broadband flux is determined ~~by~~ using ~~combining~~ exported cloud characteristics combined with reanalysis data (Stengel et al., 2020). However, there are some ~~differences~~ discrepancies in this product for the years 1994 and 2000 due to the unavailability of AVHRR data. Therefore, data from these years are not ~~utilized~~ used in this study. We
280 use the monthly mean global 0.5° grid data (Level-3C) from Cloud_cci, which includes TOA and surface upward and downward SW radiative fluxes under both all-sky and clear-sky conditions. ~~We and~~ and interpolate this data to a 1° grid to ~~maintain~~ keep consistency with CERES.

2.1.4 Reanalysis datasets

In this study, we select two state-of-the-art reanalysis data to evaluate their applicability in the study
285 of hemispherical symmetry: Modern-Era Retrospective Analysis for Research and Applications, version 2 (MERRA-2) and ERA5 reanalysis datasets.

~~The Modern Era Retrospective Analysis for Research and Applications, version 2 (MERRA-2),~~ is

the latest atmospheric reanalysis of the modern satellite era produced by NASA's Global Modeling and Assimilation Office (GMAO) with version 5.12.4 of the Goddard Earth Observing System (GEOS) atmospheric data assimilation system (Gelaro et al., 2017). It is the first long-term global reanalysis to assimilate space-based observations of aerosols and represent their interactions with other physical processes in the climate system. MERRA-2 can provide long-term radiative ~~and aerosol~~ products with a spatial resolution of $0.5^\circ \times 0.625^\circ$ from 1980. Here, ~~the radiative product from MERRA-2 is used for comparative assessment with CERES data, as well as the aerosol product and land surface product are used as the main influence factors of the clear sky atmospheric component and surface component of the PA, respectively.~~ M2TMNXRAD (or tavgM_2d_rad_Nx) monthly mean ~~radiation~~ radiative flux data, including the incident and net downward SW radiative fluxes at the TOA and the surface under all-sky and clear-sky conditions, ~~M2TMNXAER (or tavgM_2d_aer_Nx) 550nm total aerosol extinction optical depth (AOD) monthly data, and M2TMNXLND (or tavgM_2d_lnd_Nx) surface soil moisture (SM) monthly data from 2001 to 2021~~ are used for comparative assessment with CERES data selected in this investigation.

ERA5 is the fifth-generation atmospheric reanalysis of the global climate from January 1940 to present by the European Centre for Medium-Range Weather Forecasts (ECMWF). ERA5 combines model data with observations from around the world to form a globally consistent dataset that replaces the previous ERA-Interim reanalysis. 4D-var data assimilation technique in the Integrated Forecasting System (IFS) Cycle 41r2 is used to ensure a significant improvement in prediction accuracy and computational efficiency (Jiang et al., 2019; Hersbach et al., 2020). It provides hourly estimates of a large number of atmospheric, land and oceanic climate variables with a spatial resolution of $0.25^\circ \times 0.25^\circ$ (Hersbach et al., 2020). The monthly average surface and TOA radiation budget products are used in this study. ~~The total column water vapor (TCWV) data also come from ERA5.~~

In order to ~~ensure~~ maintain data consistency, ~~we resample~~ the monthly mean diurnal averaged radiative fluxes ~~and other meteorological parameters~~ from MERRA-2 and ERA5 datasets are resampled to match the $1^\circ \times 1^\circ$ resolution of CERES.

~~It's important to n~~Note that for a more accurate comparison with CERES EBAF, ~~we utilize~~ the other radiative flux data mentioned above (SW radiative flux from ISCCP-FH, AVHRR, ERA5, and MERRA-2) have been selected for their overlapping time period ~~of from~~ March 2001 to February 2016.

2.2 Methodology

2.2.1 Decomposition of ~~planetary albedo~~ reflected solar radiation contribution

To investigate the main drivers of the PARSR, we use the similar model as Stephens et al. (2015) to decompose the RSRPA into the contributions of the surface and atmospheric components. Assuming that surface and atmospheric ~~scattering have~~ reflection and absorption processes are isotropyisotropic, planetary albedo R is defined as:

$$R = \frac{F_{TOA}^{\uparrow}}{S} \quad (1)$$

Among them, the F_{TOA}^{\uparrow} is reflected SW (upwelling) flux at the TOA, S is the solar incoming (downwelling) flux. The transmittance T of the whole ~~earth~~ Earth-atmosphere system is defined as:

$$T = \frac{F_S^{\downarrow}}{S} \quad (2)$$

Where, F_S^{\downarrow} is the downwelling SW radiation at the surface. The surface albedo α is calculated as follows:

$$\alpha = \frac{F_S^{\uparrow}}{F_S^{\downarrow}} \quad (3)$$

Where F_S^{\uparrow} is the upwelling SW radiation at the surface. The term F_S^{\downarrow} can be expressed as:

$$F_S^{\downarrow} = tS + rF_S^{\uparrow} \quad (4)$$

Here, r and t represent atmospheric intrinsic reflectivity (that is, PA purely contributed by the atmosphere ~~when surface albedo is assumed to be 0~~) and atmospheric transmittance, respectively. The r and t are calculated separately, so absorption and forward scattering are included in t. F_{TOA}^{\uparrow} can be represented as:

$$F_{TOA}^{\uparrow} = rS + tF_S^{\uparrow} \quad (5)$$

By combining the above equations, R and T can be expressed by r, t and α :

$$R = r + \frac{\alpha t^2}{1 - r\alpha} \quad (6)$$

$$T = \frac{t}{1 - r\alpha} \quad (7)$$

According to the above equation, the values of r and t can be written:

$$r = R - t\alpha T \quad (8)$$

$$t = T \frac{1 - \alpha R}{1 - \alpha^2 T^2} \quad (9)$$

It can be seen that the planetary albedo R is composed of two parts: atmospheric contribution r and

surface contribution $\frac{\alpha t^2}{1-r\alpha}$. These two parts are multiplied by the incoming solar ~~radiation-radiative~~ flux S respectively, and the respective contribution values of the atmosphere and the surface to the ~~RSR_{SW}~~ ~~upwelling flux~~ at the TOA ($F_{\text{TOA}}^{\uparrow}$) can be obtained, namely $F_{\text{atm}}^{\uparrow}$ and $F_{\text{surf}}^{\uparrow}$ (unit: W m^{-2}).

$$F_{\text{atm}}^{\uparrow} \equiv Sr \quad (10)$$

$$F_{\text{surf}}^{\uparrow} \equiv S \frac{\alpha t^2}{1-r\alpha} \quad (11)$$

Following Jönsson and Bender (2022), we further decompose the atmospheric component into clear-sky atmospheric and cloud contributions. The difference between the all-sky atmospheric contribution $F_{\text{atm}}^{\uparrow}$ and the clear-sky atmospheric contribution $F_{\text{atm,clear}}^{\uparrow}$ is considered as the cloud contribution $F_{\text{cloud}}^{\uparrow}$. That is,

$$F_{\text{TOA}}^{\uparrow} = F_{\text{atm}}^{\uparrow} + F_{\text{surf}}^{\uparrow} = F_{\text{cloud}}^{\uparrow} + F_{\text{atm,clear}}^{\uparrow} + F_{\text{surf}}^{\uparrow} \quad (12)$$

$$F_{\text{cloud}}^{\uparrow} = F_{\text{atm}}^{\uparrow} - F_{\text{atm,clear}}^{\uparrow} \quad (13)$$

2.2.2 Regional mean and contribution rate

In calculating regional averages radiative flux, the study employs a geodesic weighting method consistent with the official CERES product. This method assumes Earth's oblate spheroid shape and takes into account the annual cycle of the Earth's declination angle and the sun-Earth distance (details about the method can be found in the website: "https://ceres.larc.nasa.gov/documents/GZWdata/zone_weights.f"). The regional averaged TOA ~~RSR_{reflected-SW} flux~~ F_k is spatially aggregated using the following calculation formula (Huang et al., 2012):

$$F_k = \frac{\sum_{i=1}^{N_k} W_{ki} \cdot F_{ki}}{\sum_{i=1}^{N_k} W_{ki}} \quad (14)$$

Here, N_k is the number of grid samples in region k , and F_{ki} is the ~~RSR_{reflected-SW} flux~~ corresponding to grid i in the region k . Moreover, $W_{ki} = \cos\left(\frac{\theta_i - \pi}{180.0}\right)$, where θ_i is the latitude of grid i is the geodetic zonal weight for the grid i , which can be obtained from "https://ceres.larc.nasa.gov/documents/GZWdata/zone_weights_lou.txt". Regional averages for other variables are calculated according to the similar weighting equation.

In order to explore the contribution of different regions to the total ~~hemispheric RSR_{reflected} radiation at a hemispheric scale~~, the global latitude is divided into 18 latitude zones in the unit of 10° , that is, $90^\circ\text{N}-80^\circ\text{N}$, $80^\circ\text{N}-70^\circ\text{N}$, ..., $70^\circ\text{S}-80^\circ\text{S}$, $80^\circ\text{S}-90^\circ\text{S}$. For example, the ~~contribution-rate~~ of the

cloud component [contribution](#) C_{cloud} of each latitude zone to its hemispheric [RSRreflected solar radiation](#) can be calculated by the following formula:

$$C_{\text{cloud}} = \left(\frac{\text{total_latzone_cloud}}{\text{total_hem_R}} \right) \times 100\% \quad (15)$$

~~Here, $\text{total_latzone_cloud}$ and total_hem_R are calculated from the molecular part of Eq.(14).~~

375 Where $\text{total_latzone_cloud}$ refers to the sum of the [latitude-weighted RSR of cloud component cloud contribution of reflected solar radiation](#) from all grid [points](#) in the given latitude zone, total_hem_R is the sum of [latitude-weighted total RSR reflected solar radiation](#) from all grid [points](#) in the hemisphere in which the latitude zone is located ~~(both taking into account the geodetic latitudinal weights of the different grids)~~. The contribution of surface and clear-sky atmospheric components to hemispheric [RSRreflected radiation](#) in different latitudinal zones can be derived by the similar method.

380

2.2.3 Time average

For the average contribution over time, we consider March to the following February as a complete year. Following the CERES EBAF Ed4.1 Data Quality Summary (2020), the monthly average data is weighted by the number of days in each month to obtain the annual average data (Wielicki et al., 1996; 385 Loeb et al., 2009; Rugenstein and Hakuba, 2023). For example, the annual average value of TOA [RSR&W reflected radiation flux](#) in a certain year is:

$$F_{\text{Year}} = \sum_{i=1}^{i=12} \frac{\text{DAY}_{\text{mon}}(i)}{\text{DAY}_{\text{year}}} F_{\text{mon}}(i) \quad (16)$$

where DAY_{year} is the total number of days in the given year, $\text{DAY}_{\text{mon}}(i)$ is the number of days in the current month, and $F_{\text{mon}}(i)$ is the monthly averaged [RSRradiation flux](#). The annual average values 390 of all variables are also obtained by this method.

2.2.4 CCHZ-DISO data evaluation system

To find out whether other radiation datasets can exhibit the similar hemispheric symmetry of [RSRPA](#), the CCHZ-DISO data evaluation system is also used. This method uses the Euclidean Distance between indices of simulation and observation (DISO) to evaluate the combined quality or overall 395 performance of data from different models (Hu et al., 2019; Zhou et al., 2021; Hu et al., 2022). DISO has the advantage of quantifying the combined accuracy of different models compared to Taylor diagram (Kalmár et al., 2021). Moreover, the statistical indicators chosen for the Taylor diagram are fixed,

whereas those in DISO can be taken and discarded according to the needs of the study (Hu et al., 2022). In particular, Taylor diagrams only provide statistical metrics on two-dimensional plots, DISO not only provides distances in three-dimensional space to quantify the comprehensive performance of a simulation model, but also allows a single statistical metric to capture different aspects of model performance (Hu et al., 2019).

In this paper, ~~the difference of TOA reflected radiation flux between the NH and SH from CERES-EBAF during March 2001-February 2016-2~~ is taken as the observed dataset, while AVHRR, ISCCP, MERRE-2, ERA5 are considered as the model datasets. ~~For the observed time series and the model-simulated time series, their correlation coefficient (CC), absolute error (AE), and root mean square error (RMSE) are obtained from Eqs. (17-19), respectively.~~

~~The correlation coefficient (CC), normalized absolute error (NAE) and normalized root mean square error (NRMSE) are used to construct the CCHZ-DISO 3D evaluation system. The smaller the value of DISO, the closer this model dataset is to the observed data, i.e., the better its composite performance.~~

$$CC = \frac{\sum_{k=0}^n (a_{ki} - \bar{a})(b_{ki} - \bar{b})}{\sqrt{\sum_{k=0}^n (a_{ki} - \bar{a})^2} \sqrt{\sum_{k=0}^n (b_{ki} - \bar{b})^2}} \quad (17)$$

$$AE = \frac{1}{n} \sum_{k=0}^n |b_{ik} - a_{ik}| \quad (18)$$

$$RMSE = \sqrt{\frac{1}{n} \sum_{k=0}^n (b_{ki} - a_{ik})^2} \quad (19)$$

The CCHZ-DISO 3D evaluation system is then constructed using NCC, NAE and NRMSE, which are normalized CC, AE and RMSE, respectively. Please note that the metrics are normalized to be between 0 and 1, using the normalization formula following Chen et al. (2024) as:

$$NS_a = \frac{S_a - \min(S)}{\max(S) - \min(S)} \quad (20)$$

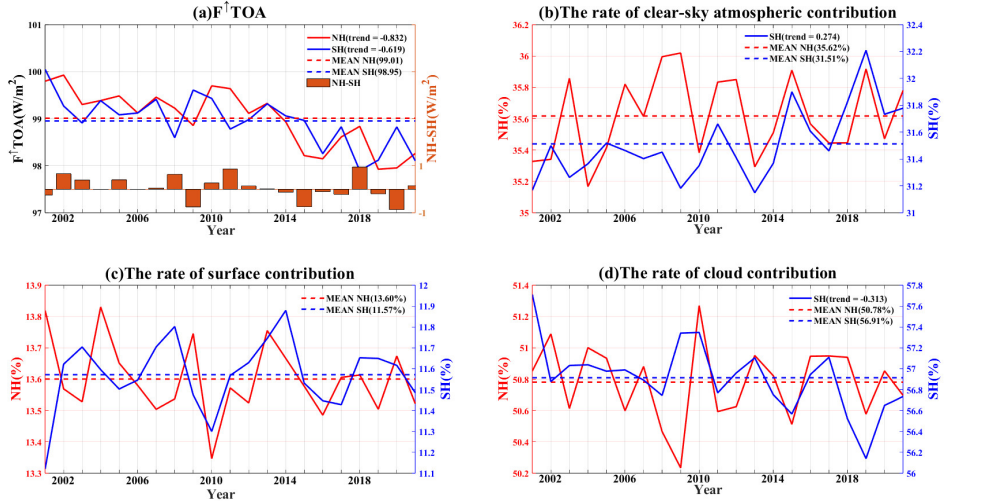
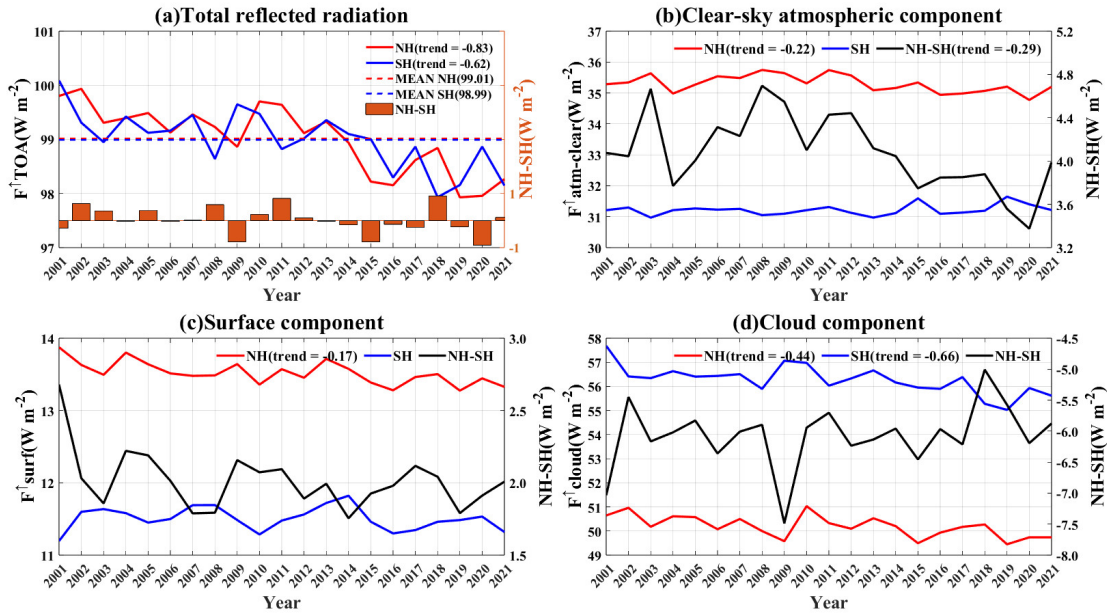
Where S indicates the metric (CC, AE, and RMSE). Here, a=0, 1, ..., m, "0" indicates the observed data, and m is the total number of model data used for comparison.

$$DISO_i^{xj} = \sqrt{(CC_i - CC_0)^2 + (NAE_i - NAE_0)^2 + (NRMSE_i - NRMSE_0)^2} \quad (21)$$

Where i and xj represent the i th model and j th variable. The subscript "0" in Eq. 21 represents statistical parameters of variable xj from observation data (here refers to CERES EBAF). A smaller/larger $DISO_i^{xj}$ values indicates better/worse performance of model i in simulating variable xj .

3 Results and discussion

3.1 Temporal variation of contribution of PARSR components in different latitudinal zones



430

Figure 1: (a) The interannual variability-mean time series of (a) total upwelling SW radiative flux reflected solar radiation at the TOA and its (b) clear-sky atmospheric, (c) surface, and (d) cloud components in the-NH and SH from 2001 to 2021 (the left axis), as well as and the annual-mean difference between hemispheres NH and SH (orange columns on the right axis) from 2001 to 2021. Interannual variation in the contribution rate of (b) the clear-sky atmospheric component, (c) the surface component, and (d) the cloud component to the SW upward radiative flux at the TOA in the NH (the left axis) and SH (the right axis); note Note that the scales of the two y-axes are not the same. The red line is for the NH, the blue line is for the SH, the orange bars and black line are for hemispheric difference (NH-SH), and the dashed line in (a) is the 21-year average

435

~~values. The trends labeled-marked in the upper right corner passes the 99.95% significance test in units of $\text{W m}^{-2} (10\text{a})\text{decade}^{-1}$ for (a) and $\% (10\text{a})^{-1}$ for (b) (d). Unlabeled trends do not pass the test of significance.~~

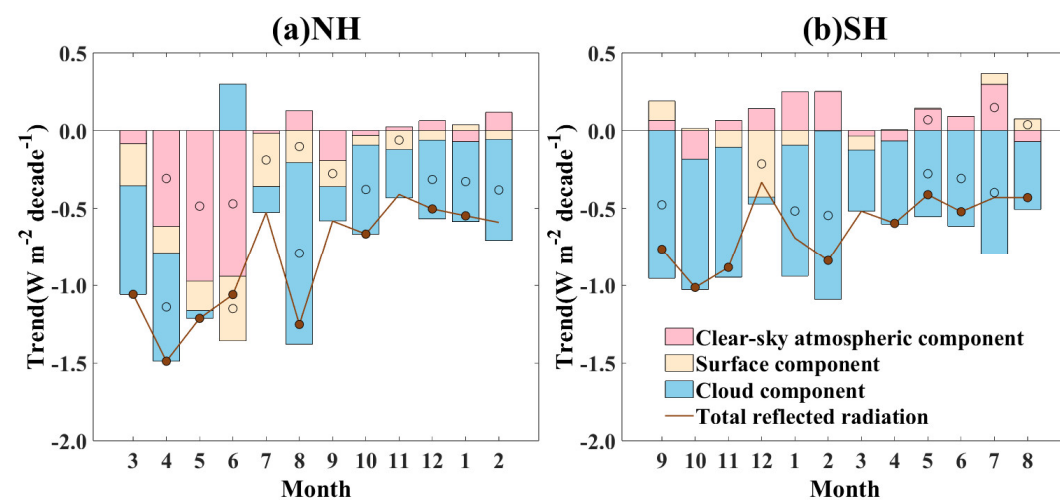
440 Firstly, we examine the general characteristics of reflected radiation in the NH and SH on an annual average scale. Figure 1 illustrates the interannual variability of ~~SW upwelling radiative flux~~ RSR at the TOA and ~~the contribution rates of~~ its three components in the NH and SH during the period of 2001-2021, based on CERES EBAF data. ~~Supplementary materials (Fig. S1) provide further details on the interannual changes of reflected radiative flux by the three components.~~ The RSR in both hemispheres
445 shows symmetry in term of multi-year averages (21-year average difference: 0.02 W m^{-2}) and the long-term trends. In a recent study, George and Bjorn (2021) argued that the symmetry of albedo cannot be established on an annual or sub-annual scale, but rather on larger spatial and temporal scales. In line with previous research (Stephens et al., 2015; Jönsson and Bender, 2022), our investigation ~~demonstrates a clear symmetry in the total reflected radiation. This symmetry is evident in both the multi-year average~~
450 ~~of reflected radiation and the long-term trend of the annual average. The difference in the annual average total reflected radiant flux between the hemispheres is less than 1 W m^{-2} , and the 21-year average difference approaches zero, indicating a nearly equal distribution of reflected SW radiation between the NH and SH.~~ Figure S1d illustrates the cumulative year to year averaging of hemispheric differences in reflected radiation. It shows that the hemispheric differences in total reflected radiation and its
455 ~~components are decreasing or tending to stabilize over time, except for the clear sky atmospheric component. The clear sky atmospheric component exhibits a strong perturbation over time, which is closely tied to human activities, particularly the highly variable emissions of anthropogenic aerosols.~~

~~The reflected SW radiation at the TOA in b~~ Both hemispheres exhibits a consistent decreasing trend (Trend_NH= $-0.832 \text{ W m}^{-2} (10\text{a})\text{decade}^{-1}$; Trend_SH= $-0.61962 \text{ W m}^{-2} (10\text{a})\text{decade}^{-1}$), indicating
460 simultaneous darkening of both hemispheres as observed from space, with the NH darkening at a faster rate. Moreover, ~~the interannual variability of hemispheric differences is increasing, and the perturbations are intensifying.~~ To investigate whether these trends in reflected radiation RSR are linked to changes in incident solar radiation, we also present the interannual variations of incident solar radiation and PA (Fig. S2S1). The results indicate that the interannual variations of incident solar radiation at TOA in both
465 hemispheres do not exhibit a significant clear-trend, with the hemispheric difference following a stable multi-year cycle. However, PA in both hemispheres shows a consistent decreasing trend (Trend_NH= $-2.4 \times 10^{-3} (10\text{a})\text{decade}^{-1}$; Trend_SH= $-1.8 \times 10^{-3} (10\text{a})\text{decade}^{-1}$), suggesting a decrease in reflected solar

~~radiation~~RSR by the Earth as a whole and an increase in absorbed solar radiation. However, the same response in both hemispheres is driven by different component changes. The darkening of the SH can be primarily attributed to a decrease in ~~reflected radiation~~RSR from the cloud component ($-0.66 \pm 0.04 \text{ W m}^{-2} \text{ decade}^{-1}$) (Fig. S1e). In contrast, the ~~reflected radiative fluxes~~RSR by all three components in the NH all show a decreasing trend, with the cloud component exhibiting the largest decrease ($-0.448 \text{ W m}^{-2} \text{ decade}^{-1}$), followed by the clear-sky atmospheric component ($-0.219 \pm 0.022 \text{ W m}^{-2} \text{ decade}^{-1}$), and the smallest decrease is for the surface component showing the smallest decrease ($-0.159 \pm 0.017 \text{ W m}^{-2} \text{ decade}^{-1}$). Moreover, the hemispheric asymmetry (NH-SH) of the clear-sky atmospheric component is decreasing ($-0.29 \text{ W m}^{-2} \text{ decade}^{-1}$) around 2008 year, which is mainly influenced by the declining reflection of the clear-sky atmosphere in the NH due to the reduced scattering of aerosol particles (Loeb et al., 2021a; Stephens et al., 2022). However, there is no clear trend in the proportion of their contributions over the NH (Fig. 1). The decreasing trend of reflected radiation from the surface component in the NH mainly originates from changes in snowpack and sea ice at the poles, but its impact on the global average appears to be insignificant (Stephens et al., 2022). Additionally, the decreasing trend of reflected radiation in the NH can be attributed to reduced scattering of aerosol particles (Loeb et al., 2021a; Stephens et al., 2022) and a decrease in low cloud cover (Loeb et al., 2018a; Loeb et al., 2020). The decrease in low cloudiness may be linked to a shift in the Pacific Decadal Oscillation (PDO) phase from negative to positive, resulting in warmer sea surface temperatures (SSTs) in parts of the eastern Pacific, which significantly reduces low cloud cover and reflected solar radiation (Andersen et al., 2022). To further investigate the inter-hemispheric differences in Earth's energy balance, we also calculate the trends of outgoing longwave radiation and net radiation at the TOA (figure not shown). A significant increasing trend of longwave radiation emitted to space is found in the NH ($0.324 \text{ W m}^{-2} (10a)^{-1}$), while no significant trend is observed in the SH. Loeb et al. (2021b) noted that the increase in outgoing longwave radiation is primarily due to the increasing global surface temperature and changes in clouds, although it is partly compensated by the increase in water vapor and trace gases. However, the overall increase in outgoing longwave radiation does not outweigh the decrease in reflected shortwave radiation, resulting in a positive trend in the net radiative flux in both hemispheres (indicating that the Earth is absorbing more energy) (Raghuraman et al., 2021). This positive trend in the Earth's energy imbalance (EEI) will exacerbate global warming, sea level rise, increased internal heating of the oceans, and melting

of snow and sea ice (IPCC, 2013; Von Schueckmann et al., 2016; Loeb et al., 2021b). Indeed, a recent study based on long-term homogenized radiosonde data indicated that the atmosphere has become increasingly unstable in the NH during the period 1979–2020 (Chen and Dai, 2023).

500 In Fig. 1, the contributions of the three components to the PA exhibit varying degrees of hemispheric asymmetry. Among the three components, clouds contribute the most, accounting for over 50%, followed by the clear sky atmosphere, and the surface with the least contribution. The cloud contribution in the SH is approximately 6.13% higher than that in the NH, which can be attributed to the presence of more abundant and brighter cloudiness in the SH. The clear sky atmospheric contribution is 4.11% higher in the NH compared to the SH, possibly due to greater anthropogenic aerosol emissions resulting from human activities in the NH. The clear sky atmospheric contribution rate in the SH shows an increasing trend of 0.274% per decade, which may be attributed to a decrease in the cloud component contribution of -0.313% per decade. This is because there is no clear trend in the reflected radiative flux by the clear sky atmosphere in the SH, but there is a significant decrease in the cloud component (Fig. S1c). However, from a radiative flux perspective, the hemispheric asymmetry of the clear sky atmosphere is decreasing (Fig. S1a), primarily influenced by the declining reflection of the clear sky atmosphere in the NH, which is associated with the recent reduction of anthropogenic aerosols in eastern North America, Europe, and East Asia (Raghuraman et al., 2021; Quaas et al., 2022; Stephens et al., 2022). In comparison to the SH, the NH exhibits a 2.03% higher surface contribution (Fig. 1c). Although the NH has a greater land distribution, the higher ice albedo in Antarctica partially compensates for the lack of land area in the SH, resulting in a less significant difference in surface contribution between the hemispheres.



520 Figure 2: The hemispheric averaged trends in reflected solar radiation and its components in the (a) NH and (b) SH for different month from 2001-2021. Pink, yellow and blue bars indicate trends in the clear-sky atmospheric component, surface component and cloud component, respectively. The brown line indicates the trend of total reflected solar radiation. Dots of different colours indicate that the hemispheric averaged trend of the corresponding variable is significant at the 95% confidence level.

525 The analysis presented above is based on the results of annual average RSR. Note that the symmetry of RSR between hemispheres is a characteristic observed at interannual scales. However, certain natural and human activities (e.g., the Pinatubo eruption, Australian bushfires, societal response to the COVID-19 pandemic) that strongly influence albedo or compensate for hemispheric asymmetry are seasonal or even occur only in specific months of the year (Minnis et al., 1993; Hirsch and Koren, 2021; Diamond et al., 2022). They can generate significant perturbations on interannual scales due to strong signals in specific seasons. To further clarify the variations of these mechanistic signals by resolving RSR and its
530 components at finer temporal scale (e.g., monthly), Figure 2 resolves the long-term trends in RSR for both hemispheres into different months. The results indicate that the significant decreasing trends in hemispheric RSR for both hemispheres are generally observed throughout the year, with an obvious reduction from spring to winter. This is related to seasonal changes in trends with different components. In addition, there is no significant trend in the RSR of the NH for July and the SH for December. This
535 may due to the fact that the decreasing trends observed in different months are regulated by different components at different latitudes, thus not showing consistent changes.

In the NH, the decreasing trends of RSR are highest in the months of March to June and August, being more than twice as large as the trends in winter months. The peak value of the decreasing trend occurs in April, which is influenced by both the clear-sky atmospheric and cloud components. The trend
540 from April to June is primarily driven by the clear-sky atmospheric component. Here, we further decompose the results of the monthly trend into different latitude zones (Fig. S2, S3), the statistical results show that the significant decreasing trend of the clear-sky atmospheric component in the NH during April-June is mainly contributed by the mid-latitude regions (30°N-60°N). The vital dust belt is located in these regions, serving as the major emission source of dust, typically peaking in spring and early
545 summer (Yang et al., 2022). However, due to reduced local wind speeds and increased soil moisture, dust activity frequencies in regions such as West Asia, and Central Asia have experienced varying degrees of decline (Shao et al., 2013; Shi et al., 2021; Zhou et al., 2023). Particularly, the frequency of dust storms in China has significantly decreased due to increased vegetation cover (Zhao et al., 2018; Jiao et al.,

2021). Moreover, in regions with concentrated industrial and anthropogenic aerosol emissions, such as Europe, eastern and central China and North America, effective emission reduction policies have led to a decrease in polluting sulfate aerosols (Zhao et al., 2017; Li et al., 2020; Tao et al., 2020; Yu et al., 2020; Gui et al., 2021; Cui et al., 2022; Tang et al., 2022), weakening the contribution of the clear-sky atmospheric component in RSR. In most months (especially in August, October, December, and January) except the spring, the decreasing trend of RSR in the NH is primarily dominated by the cloud component. The decreasing trend of cloud component reaches its maximum in August, and is mainly influenced by the regions between 50°N-60°N and 0°-10°N. For the 50°N-60°N regions, the low cloud cover over northeast Pacific has decreased significantly over the last 20 years, due to the weakening temperature inversion intensity and increasing sea surface temperature (SST), which has reduced the cloud component of RSR in this region (Andersen et al., 2022). At 0-10°-N, the decreasing trend in RSR is particularly strong over the tropical western Pacific. This is due to the increase in SST, which reduces the stability of the marine boundary layer (MBL), leading to MBL deepening and decoupling between cloud cover and surface moisture supply, thus reduce the cloud cover and corresponding cloud component of RSR (Loeb et al., 2018a). Compared to the other components, the surface component of RSR does not dominate the decreasing trend of NH in a specific month. It decreases most rapidly in June, followed by July, which is primarily located at the region between 70°N-80°N. This decrease may link to the advancement and lengthening melting period of Arctic ice due to the Arctic amplification effect, which can affect changes in surface component of RSR (Noël et al., 2015; Wang et al., 2018; Mika et al., 2022).

In the SH, the cloud component dominates the decreasing trend of RSR for all months except December. This dominant role is mainly contributed by the latitudinal zones from equator to 60°S, although the trends of cloud component in these latitudinal zones may not be significant on a single month. This may be partly attributed to decreasing cloud cover. On the one hand, the low cloud cover over tropics has decreased significantly due to the increasing SST. On the other hand, multi-source satellite cloud climatological data consistently show a significant decreasing trend in total cloud cover over the Southern Ocean (Devasthale and Karlsson, 2023). The maximum value of the RSR decreasing trend occurs in October, while the cloud component of RSR decreases fastest in February. In December, the trend in the SH is dominated by the surface component in the region of 60°S-70°S (see Figure S3),

where is covered with extensive ice and snow coverage. Under the background of global warming, ice and snow are melting rapidly, resulting in significant seasonal changes in ice and snow cover. However, over the Arctic, surface warming is occurring at a rate nearly four times faster than the global warming rate (Mika et al., 2022), leading to a continued decrease in Arctic ice cover. (Raghuraman et al., 2021; Quaas et al., 2022; Stephens et al., 2022)

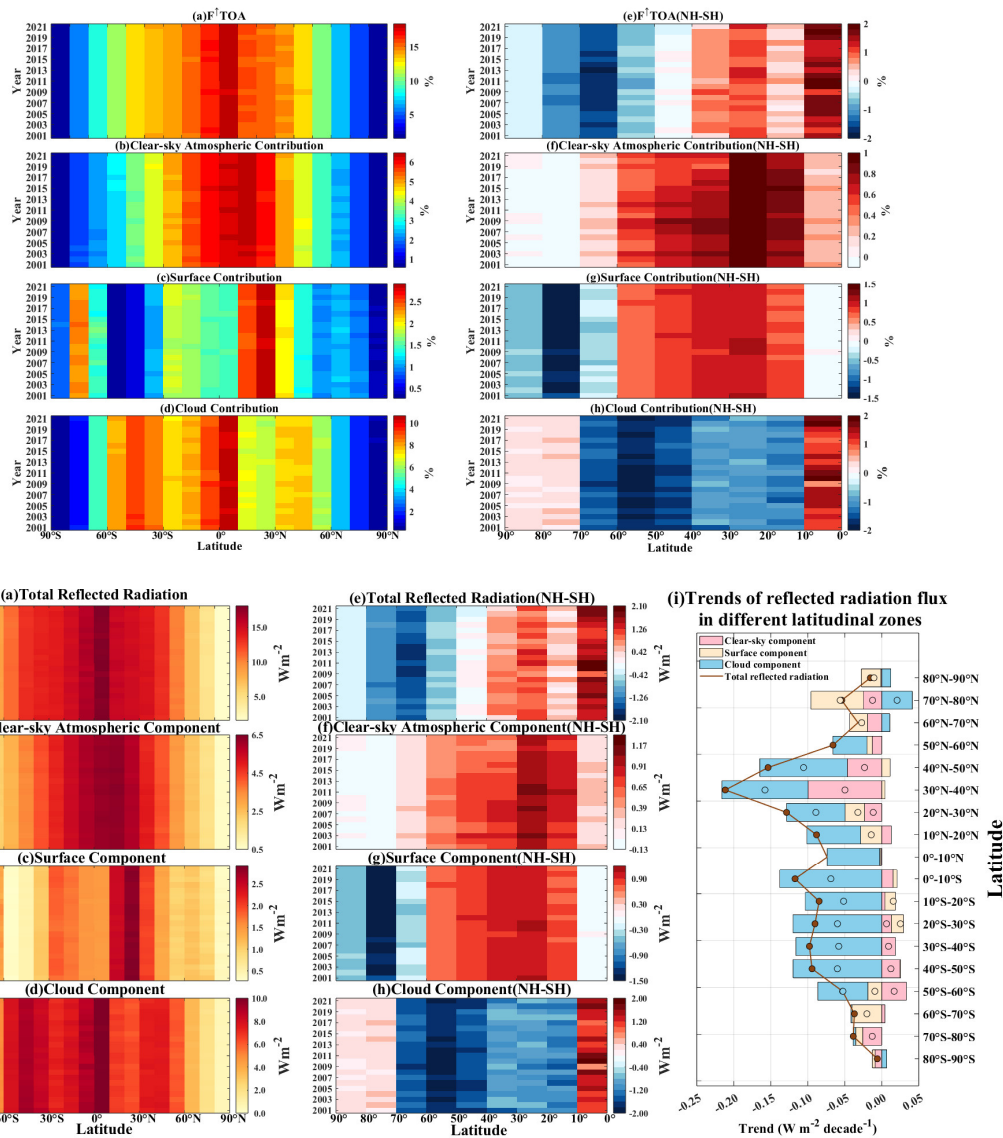


Figure 2: Figure 3: Annual averaged time series of (a) total RSR and its (b) clear-sky atmospheric component, (c) surface component, and (d) cloud component at different latitudinal zones, along with (e-h) the interhemispheric differences (NH-SH) between corresponding zones and (i) the zonal mean trends at different latitudinal zones from 2001 to 2021. Pink, yellow and blue bars indicate trends in the clear-sky atmospheric, surface and cloud components, respectively. The brown line indicates the trend of total RSR. Dots of different colours indicate that the interannual trend of the corresponding variable at the given latitude zone is significant at the 95% confidence level. (a) Contribution of different latitudinal zones to hemispheric total reflected radiation at TOA from 2001 to 2021 and the corresponding components: (b) the clear sky atmospheric component, (c) surface component and (d) cloud component. Contribution differences between

595 ~~the corresponding latitudinal zones of the two hemispheres (NH minus SH) are also given in (e), (f), (g) and (h).~~

600 Large-scale systems or certain compensatory mechanisms that may affect the hemispheric symmetry of PA-RSR do not directly ~~operate-act~~ on a hemispheric scale. Instead, they can compensate for hemispheric energy imbalances by ~~influencing-affecting~~ local or regional climates. For ~~instanceexample~~, ~~baroclinic activityoblique pressure activity~~, although ~~occurring primarily-mainly~~ ~~occurring~~ at mid-latitudes, ~~exerts-has~~ a significant influence on cloud albedo, thereby strongly impacting global albedo (Hadas et al., 2023). While larger regional anomalies in ~~reflected radiative fluxRSR~~ may offset each other when spatially and temporally averaged to calculate global PA-RSR and its interannual variations, these anomalies play a crucial role in regional radiation budgets, subsequent climate change, and the identification of mechanisms that maintain or compensate for PARSR. Therefore, to ~~gain further~~ ~~insight into~~ further deepen the understanding of the regional RSR changes and provide a reference for mechanism research ~~the regional effects of these influencing mechanisms~~, we ~~have divided~~ divide the globe into 18 latitudinal zones in 10° increments. Figure 3a-h show the time series of latitudinal averaged RSR and interhemispheric differences of RSR and their components at different latitudinal zones, where Figure 3i shows the interannual trends of RSR and its components at different latitudinal zones. Note that the RSR and their trends for different latitudinal zones are area-weighted based on Eq. (14) for comparison. Figure 2 illustrates the contribution of each latitudinal zone to the total reflected radiation of its respective hemisphere, where (b) (d) of Fig.2 depict the contribution of the three components to the total reflected radiative energy of the hemisphere in each latitudinal zone.

615 In general, the total RSR in both hemispheres decreases from the equator towards the poles, while the zonal-averaged magnitude of their components of RSR varies. In the SH, the zonal distribution of clear-sky atmospheric components is similar to that of the RSR. In the NH, the extreme values of clear-sky atmospheric components of RSR occur at 10°N-20°N, where has a large amount of dust aerosols from the Sahara Desert. The RSR peak by surface components are located at 70°-80° in the SH and 20°-30° in the NH, respectively, due to the high ice and snow albedo and high surface albedo caused by bare

620 ground. The cloud component reflects the most radiation at 40°S-50°S in the SH and at 0°-10°N in the NH, since these regions are where the storm tracks of Southern Ocean (George and Bjorn, 2021) and the annual average position of ITCZ (Gruber, 1972) are located, respectively.

For the hemispheric differences (Fig. 3e-h), it is shown that ~~the interannual variation in the~~

625 ~~contribution rate of each latitude zone to the total hemispheric reflected radiation is small. However,~~
~~there are still some relatively anomalous years, which will be discussed in detail in the next section (3.2).~~
~~More~~ energy is reflected from the 0°-40° latitude zones in the NH compared to the corresponding
latitude zones in the SH (~~Fig. 2e~~). However, this imbalance is compensated by more reflection from the
SH in the 50°-90° latitude zones. ~~The higher RSR from the 0°-40° latitude zones in the NH stems from~~
~~the higher cloud component from the equator to 10° and the combined effect of clear-sky atmospheric~~
630 ~~and surface components in the 10°-40°. The dominance of the NH mainly arises from the clear sky~~
~~atmospheric contribution between 0°-70°, the surface contribution from 10°-60°, and the cloud~~
~~contribution from the equator to 10°.~~ In contrast, the strength of the SH at middle and high latitudes is
derived from the surface ~~contribution component~~ from 60°-90° and the cloud ~~contribution component~~
from ~~40°-70°~~. ~~At 40°-50°, more radiation from cloud component in the SH offset the more radiation~~
635 ~~from clear-sky atmospheric and surface components in the NH.~~ Regarding ~~the~~ clear-sky atmospheric
~~componente contributions~~, the NH as a whole slightly ~~exceeds higher than~~ the SH (except in the polar
regions), possibly due to the ~~higher presenee~~ ~~large amount~~ of dust aerosols in the NH tropics and
subtropics, as well as more sulfate pollution in the mid-latitudes (Diamond et al., 2022). Notably, the
~~disparity difference~~ in clear-sky atmospheric ~~contributions components~~ between the two hemispheres is
640 greatest at 20°-30° ~~(around 1%)~~, influenced by the combined effect of more dust and sulfate aerosols in
the NH. There are significant hemispheric differences in surface ~~componente contributions~~, with the NH
exhibiting larger ~~RSR from~~ surface ~~componente contributions~~ concentrated in the 10°-60° latitude range,
~~surpassing those in the SH. This discrepancy is expected due t because of~~ the larger land area in the NH.
~~Conversely, And~~ in the region from 60° to the poles, particularly from 70°-80°, the SH shows a ~~greater~~
645 ~~larger~~ surface ~~contribution component~~ due to ~~the~~ higher snow and ice ~~coverage cover~~ in the near-polar
regions, ~~resulting in which reflects~~ more solar radiation ~~reflection~~. ~~However, over the Arctic, surface~~
~~warming is occurring at a rate nearly four times faster than the global warming rate (Mika et al., 2022),~~
~~leading to a continued decrease in Arctic ice cover.~~ ~~For the cloud component, The the~~ SH also exhibits a
~~more significant contribution rate reflection from clouds~~ between 10° and 70°, ~~with the extreme values~~
650 ~~of the hemispheric differences occurring at 50°-60°~~. This is ~~not only~~ attributed to ~~lower contributions~~
~~from the surface and clear sky atmosphere but also to~~ the ~~prevalence of higher~~ subtropical cloudiness and
~~higher~~ cloud albedo at mid-latitudes (Engström et al., 2017). The ~~greater contribution of more radiation~~

from NH clouds near the equator may be due to the persistent presence of the ~~Intertropical Convergence Zone~~ (ITCZ) north of the equator in the eastern Pacific and Atlantic. This observation suggests that the SH heavily relies on extratropical clouds to compensate for clear-sky hemispheric asymmetries, which is consistent with previous studies (George and Bjorn, 2021; Blanco et al., 2023; Hadas et al., 2023; Rugenstein and Hakuba, 2023). Based on the above analyses we can conclude that it is the offsetting of the differences in the different components across the latitudinal zones that leads to the minimal hemispheric differences in total RSR.

In addition, to clarify the variations and hemispheric differences of RSR at finer temporal scale, we further analyze the annual cycle of RSR across different latitudinal zones. Figure S4-S7 illustrate the annual cycle of RSR and its components in different latitudinal zones and their interhemispheric differences. It can be seen that the RSR in different latitudinal zones of both hemispheres presents obvious monthly variations, with the peak values in spring and summer, and low values in autumn and winter, typically reaching maximum values in summer. The annual cycles of RSR and its components are mainly dominated by the monthly variation of incident solar radiation (Fig. S8). However, the surface components in the 40°N-60°N latitudinal zones exhibit enhanced reflectivity in spring (Fig. S6), possibly influenced by surface albedo (Fig. S9). The annual cycle of hemispheric RSR differences is dominated by the cloud component at mid-low latitude and the surface component at high-latitude, rather than by incident solar radiation, which remains relatively stable.

Furthermore, statistical results indicate that the interannual trends of RSR at different latitudinal zones are highly significant (Fig. 3i). It is clear that the hemispheric decreasing trend of RSR is the cumulative result of decreasing trends of RSR across all latitude zones. Fig. S10a-c presents the global distribution of the trends in three components of RSR, which help to identify the key areas and factors influencing the trends. From Fig. 3i, it can be observed that the RSR trends in the NH for different latitude zones below 60°N are widely disparate, whereas the trends in the SH for different latitude zones below 60°S are relatively homogeneous, mainly due to the difference in their dominant components. Most of the downward trends in the NH come from 20°-50°, with the strongest trend coming from 30°-40°, dominated by significant decreases in cloud and clear-sky atmospheric components. Decreasing trends in cloud component are mainly observed over the Northeast Pacific and North Atlantic near North America (Fig. S10c). The decreasing trend in cloud component over the Northeast Pacific may be

685 associated with a shift in the Pacific Decadal Oscillation (PDO) phase from negative to positive, which leads to warmer SSTs in parts of the eastern Pacific, thus significantly reducing low cloud cover and RSR (Loeb et al., 2018a; Loeb et al., 2020; Andersen et al., 2022). The significant decreasing trends for 20° N-50°N in the clear-sky atmospheric component occurs in Europe, central China, the eastern seas of China and the eastern United States (Fig. S10a), which is consistent with previous studies and related to the reduced aerosol particle scattering (Loeb et al., 2021a; Raghuraman et al., 2021; Quaas et al., 2022; Stephens et al., 2022). At 70°N-80°N, the decreasing trend in total RSR is dominated by the surface component, accompanied by a significant decrease in the clear-sky atmospheric component and partially compensated by an increase in the cloud component. The strong downward trend of the surface component can be observed along the northern coast of the Asian and European continents and over the Arctic Ocean (Fig. S10b), which is inseparable from the decrease in albedo caused by the strong retreat of sea ice.

690

695 From the equator to 60°S, there are significant decreasing trends in cloud components, which dominate the trends in RSR (Fig. 3i). The extreme value of the trends in total RSR of SH occurs at 0°-10°S due to the significant reduction in cloud components over the tropical western Pacific (Fig. S10c). From 20°S-60°S, the trends in clear-sky atmospheric component even exhibit significant positive values, especially at 50°S-60°S. The increasing trend of clear-sky atmospheric component in low-latitude zones of SH is primarily observed over Chile and the South Tropical Pacific (Fig. S10a). This trend in the former region stems mainly from the increasing secondary aerosol loading (Miinalainen et al., 2021), while the trend in the latter region may be remotely influenced by biomass burning in South-East Asia and South America (Li et al., 2021). In addition, studies have shown that large amounts of dust and smoke from the 2019-2020 forest fires in Australia significantly affect the aerosol loading over the South Pacific (Yang et al., 2021). At mid and high latitudes, the clear-sky atmospheric components are generally

700 increasing over the Southern Ocean, which may be related to the change of aerosol loading. Based on model simulations, Bhatti et al. (2022) found that the depletion of stratospheric ozone can alter the westerly jet and affect wind-driven aerosol fluxes, hence increasing the aerosol loading over the Southern Ocean, which includes sea salt aerosols and phytoplankton-produced sulfate aerosols.

705

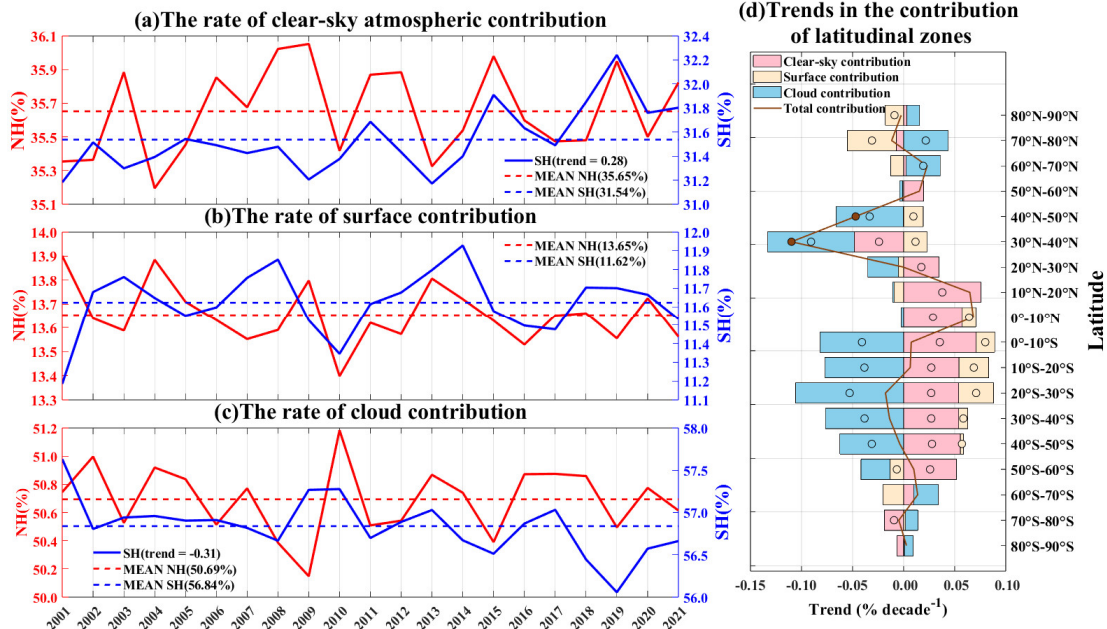
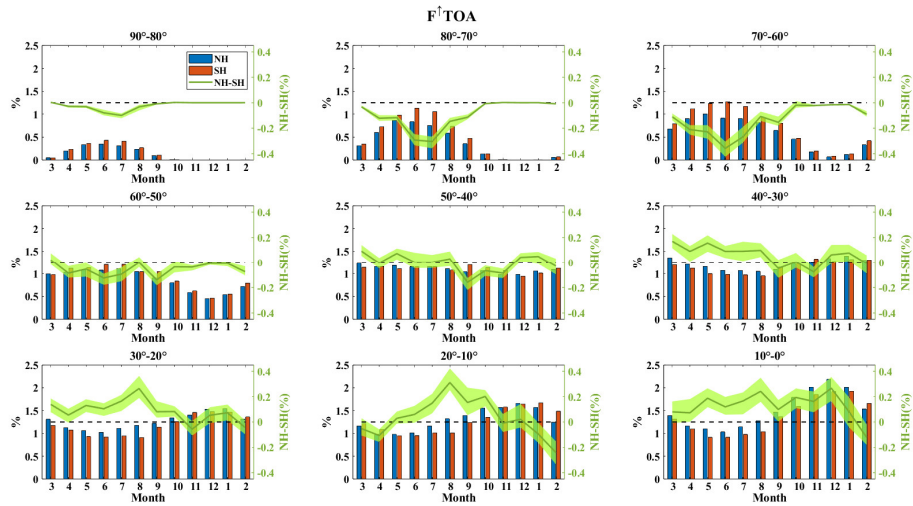


Figure 34: Interannual mean time series of the contribution rate for (a) the clear-sky atmospheric component, (b) the surface component, and (c) the cloud component to the total reflected solar radiation at the TOA in the NH (the left axis) and SH (the right axis) from 2001-2021; note that the scales of the two axes are not the same. The red line is for the NH, the blue line is for the SH, and the red/blue dashed lines are 21-year averaged values of NH/SH. The trends marked in the upper right corner passes the 95% significance test in units of % decade⁻¹. (d) The zonal mean trends in the contribution rate of different latitudinal zones to hemispheric total reflected solar radiation from 2001-2021. Pink, yellow and blue bars indicate trends in the clear-sky atmospheric contribution, surface contribution and cloud contribution, respectively. The brown line indicates the trend of total reflected solar radiation contribution. Dots of different colours indicate that the zonal mean trend of the corresponding variable at the given latitude zone is significant at the 95% confidence level. Monthly variation of the total reflected SW radiation contribution of different latitude zones to the total reflected SW radiation of their hemispheres and their hemispheric differences. The blue bars are for the NH, orange for the SH, corresponding to the left axis; the green line represents the inter-hemispheric difference, corresponding to the right axis, and the green shading indicates the difference spread in hemispheric

725 ~~difference for the corresponding month in that latitude zone during 2001-2021. The months are marked~~
~~according to the NH, corresponding to the SH months of September, October, ..., January, February, ..., and~~
~~August.~~

730 The analysis above is all based on RSR and its components at different latitudinal zones, which can
directly show the variation of their reflected ability to solar radiation. However, they cannot reflect
changes and adjustments in the contribution of different components to the total RSR. So this study
further quantifies the contribution rates of different components to the RSR (Fig. 4a-c) and the
contribution rates of different latitudinal zones to hemispheric RSR based on Eq. (15) (Fig. 4d). There
are clear hemispheric asymmetries in the contributions of the three components to the hemispheric RSR,
which indicates that the relative importance of the three components varies in different hemispheres. For
735 both hemispheres, the cloud component contributes the most to the RSR, accounting for over 50%,
followed by the clear-sky atmospheric component, while the surface component contributes the least.
The cloud contribution rate in the SH is approximately 6.15% higher than that in the NH, which can be
attributed to more and brighter clouds in the SH (Stephens et al., 2015; Datsseris and Stevens, 2021;
Diamond et al., 2022; Jönsson and Bender, 2023). The clear-sky atmospheric contribution rate in the NH
740 is 4.11% higher than that of the SH, possibly due to greater anthropogenic aerosol emissions resulting
from human activities in the NH (Diamond et al., 2022; Jönsson and Bender, 2022). Although all three
components of RSR in the NH show significant decreasing trends, there is no significant trend in the
proportion of their contributions. This means that there is no significant adjustment in the radiation
budget for the NH. The clear-sky atmospheric contribution rate in the SH shows an increasing trend of
745 0.28% per decade, which may be regulated by a decreasing trend of -0.31% per decade in the cloud
component contribution (Fig. 1 and Fig. 4). Compared to the SH, the NH exhibits a 2.03% higher surface
contribution rate. Although the NH has a larger land distribution, the higher ice albedo in Antarctica
partially compensates for the lack of land area in the SH (Fig. S9), resulting in a less significant difference
in surface contribution between the hemispheres (Diamond et al., 2022).

750 The spatial distributions of the contribution rates of the three components (Fig. S10d-f) are generally
consistent with the trends in RSR (Fig. S10a-c), however some regional differences exist. For example,
a strong increasing trend in the clear-sky atmospheric contribution rate is observed in the equatorial
western Pacific, which does not appear in its RSR. This is a moderating result of the decreasing
contribution of the cloud component, indicating an increasing significance of the clear-sky atmospheric

755 component for RSR in this region. In addition, the cloud component contribution rates show a wider distribution of increasing trends over the Arctic compared to the RSR. This is not only due to the increase in RSR from the cloud component, but also closely related to the significant decrease in the surface component at high latitudinal zones (Fig. 3i). This indicates that cloud components are playing an increasingly crucial role in the radiation budget in the Arctic.

760 There is no significant trend in the contribution of each latitudinal zone to the hemispheric RSR, except for a significant decreasing trend from 30°N to 40°N (Fig. 4d). Although the decreasing trend in cloud component of RSR at this latitude zone is greater than that of the clear-sky atmospheric component (Fig. 3i), the significant decreasing trend in the contribution rate of this latitude zone to the hemispheric RSR is mainly due to the reducing clear-sky atmospheric contribution. For the SH, trends in the different
765 components cancel each other out, resulting in no trend in the contribution of the latitudinal zones to the total hemispheric RSR. For example, in the 0°-50°S region, the significant decreasing cloud component's contribution to the hemispheric RSR is offset by increasing clear-sky atmospheric and surface component contributions in the hemispheric RSR.

770 The analysis presented above is based on the results of annual average reflected radiation. It is important to note that the symmetry of PA between hemispheres is a characteristic observed at interannual scales. However, certain natural and human activities that strongly influence albedo or compensate for hemispheric symmetry operate seasonally or even occur only in specific months of the year. These activities can have a significant impact on interannual scales, with their signals being more pronounced during particular seasons. We therefore hope to further clarify the variations of these mechanistic signals by resolving the reflected radiation and its components at finer temporal scale (e.g., monthly).

775 Figure 3 illustrates the monthly changes of contribution from different latitude zones to the total amount of reflected SW radiation and their contribution differences between two hemispheres. It is evident that the total reflected radiation from different latitude zones in both hemispheres exhibits noticeable monthly changes. From the equator to the 40° region, higher contributions are observed during autumn and winter, while lower contributions are seen during spring and summer. Additionally, in most months, the latitude zones in the NH have higher contributions compared to those in the SH. However, from the 50° to the polar region, the annual cycle of contribution rate reverses. Specifically, the contributions during spring and summer become more prominent in these regions. Notably, the latitude
780

785 zones in the SH consistently exhibit higher contributions to the entire hemisphere throughout the year compared to the corresponding latitude zones in the NH. This difference is particularly significant during June and July in the 60°–80° latitude range, primarily due to variations in contributions from the surface and cloud components (Fig. S4–S5). Overall, the annual cycle is primarily determined by seasonal variations in the contributions of the cloud component (Fig. S5) and the clear-sky atmospheric component (Fig. S3) at low and middle latitudes. Additionally, the surface component exerts a strong influence at high latitudes (Fig. S4). The reversal of the annual cycle of the latitudinal zone contribution of reflected radiation after 40° is mainly attributed to similar variability characteristics observed in incident solar radiation (Fig. S6).

790 From 10° to 60°, the surface contribution in the NH consistently exceeds that in the SH, likely due to the larger land area in the NH (Fig. S4). However, there is no clear monthly variation pattern for the interhemispheric differences in surface contributions within these latitudinal zones. At low latitudes, the surface contributions in both hemispheres exhibit similar monthly variations to those observed in the total reflected radiation contribution (Fig. 3). In the 0°–10° range, which is predominantly oceanic, the hemispheric difference in surface contributions is nearly negligible. From 60° to 90°, the dominant role of summer in the SH becomes more pronounced, with a greater contribution from the surface component compared to the cloud component at 70°–90° S. However, in the NH, the cloud component still contributes the most at 60°–90°. Furthermore, in these high-latitude zones, there is no significant annual cycle in the hemispheric differences of incident solar radiation. Therefore, the hemispheric differences in surface contributions are primarily influenced by surface albedo (Fig. S7). These regions are located close to the poles and have extensive ice and snow cover. With global warming, ice and snow melting is occurring at a rapid pace, resulting in noticeable seasonal changes in ice and snow cover. Notably, at 70°–80°, the annual cycle pattern of the hemispheric difference in surface component contribution (Fig. S4) closely resembles that of surface albedo (Fig. S7), albeit with the latter exhibiting extremes 2–3 months later than the former. This discrepancy may arise from the fact that the contribution of the surface component is defined relative to the reflected radiation at the TOA, while surface albedo is influenced by cloud masking and modulation (Qu and Hall, 2005). Additionally, the surface contribution from the NH at 70°–80° peaks in May, one month earlier than in the SH, although both hemispheres experience their incident radiation peak in June (Fig. S6). This discrepancy is related to the distinct patterns of

monthly changes in surface albedo between the two hemispheres and the differential responses of polar snow and ice to global warming. The Arctic melt season is advancing and lengthening due to global warming and the Arctic amplification effect (Noël et al., 2015; Wang et al., 2018). From a hemispheric difference perspective, the annual cycle of total reflected radiation contribution primarily stems from the cloud component contribution in mid-low latitude regions and from surface and cloud contributions in high latitude zones, with the clear sky atmospheric contribution exhibiting relatively weak variability. The interannual spread of the annual cycle of cloud component contribution is significant across all latitudinal zones, whereas the clear sky atmosphere and surface contributions remain relatively stable. This indicates that the interannual variability of the seasonal radiation cycle in different latitudinal zones is predominantly driven by cloud contributions.

3.2 Contribution of different factors to latitudinal zones in extreme years

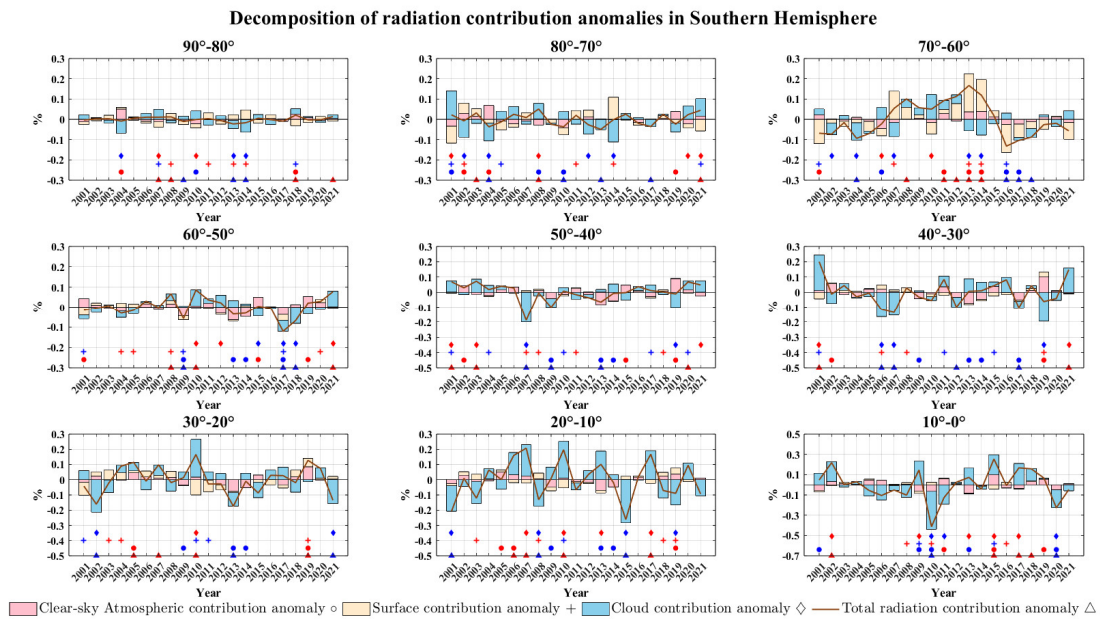


Figure 4: Anomaly time series of contribution rate of total reflected radiation and its three components of each latitude zone to total hemispheric reflected radiation in the SH during 2001 to 2021. The pink is the contribution anomaly of the clear sky atmosphere, the yellow is the contribution anomaly of the surface, the blue is the contribution anomaly of the cloud, and the brown line represents the total contribution anomaly to the total hemispheric reflected radiation. The triangles labeled in the figure indicate that the contribution anomaly of total reflected radiation in this latitudinal zone for the year exceeds one of its standard deviations, i.e., it is an extreme value, with blue indicating extreme lows and red indicating extreme highs. Circles, plus signs, and diamonds indicate extreme values of clear sky atmospheric contribution anomalies, surface contribution anomalies, and cloud contribution anomalies, respectively. Note that the vertical scale is different for different latitudinal zones.

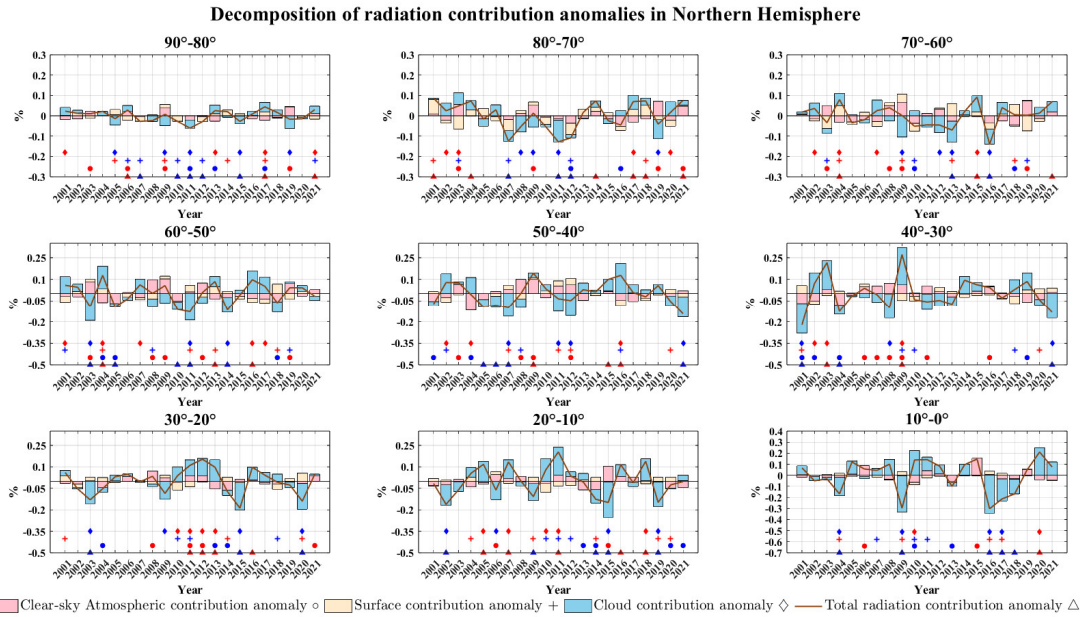


Figure 5: Same as Fig.4, but for the NH.

Different components play distinct roles in each latitudinal zone, and this section further explores which component dominates the variation of reflected radiation contribution under extreme conditions. It would be a valuable improvement if the model could capture the anomaly in contribution from different components across latitudinal zones during such extremes. Thus, we begin by decomposing the yearly contribution anomaly of total reflected radiation for each latitude zone into contribution anomalies of the three components. Subsequently, we identify extreme values of the total reflected radiation contribution anomaly and the three component contribution anomalies for each latitudinal zone by exceeding their respective one standard deviation (indicated in Fig. 4 and Fig. 5 using different symbols). Additionally, we label years with extreme anomalous values of total reflected radiation contribution anomaly as "extreme anomalous years" (represented by triangles in Fig. 4 and Fig. 5). Considering that variations in PA and its components are influenced by atmospheric and surface properties (Loeb et al., 2007; Voigt et al., 2014; Jian et al., 2018), we select surface related factors: ISC, SM, NDVI; cloud related factors: LWP, IWP, CVOD, CF; and clear sky atmospheric related factors: TCWV, AOD. To further correlate the anomalies contributed by different components in different latitudinal zones with changes in the control factors during extreme anomalous years, we calculate the proportion of anomalies in the different factors that fall outside their normal ranges (one standard deviation) (Fig. S8, S9). This proportion is obtained by calculating the annual mean anomaly of each factor in certain latitude zone minus its standard deviation and then dividing by the standard deviation. Importantly, it should be noted that the radiation

855 contributions from different latitudinal zones exhibit varying sensitivities to changes in different factors,
resulting in different magnitudes of response. For instance, in the 10° S–20° S zone, snow formation is
challenging and limited to high altitudes in the Andes Mountains (Saavedra et al., 2017). Therefore,
changes in ISC in this latitudinal zone reflect changes in only a small part of the region and have little
effect on the contribution of reflected radiation from the entire latitudinal zone.

860 Overall, the range of interannual variation in reflected radiation contribution is relatively large in
the middle and low latitudes, while it remains more stable near the poles with minimal fluctuations.
Previous studies have demonstrated that cloud variability dominates the variability of PA (Stephens et
al., 2015; Seinfeld et al., 2016), and this conclusion holds true across different latitude zones. In most
865 latitude zones in both hemispheres, especially in the tropics and subtropics, the radiative contribution
variability is primarily influenced by the cloud component (Jönsson and Bender, 2022). This conclusion
also applies to extreme cases. Globally, 87 % of extreme anomalous years are dominated by contribution
anomalies from the cloud component, 10 % by the surface component, and 3 % by the clear sky
atmospheric component (Fig. S10). However, there is a slight difference between the NH and SH. In the
870 SH, 18 % of extreme years are dominated by anomalies in the surface component contribution, compared
to only 3 % in the NH. Among all events with extreme value occurrences caused by total radiative
contribution anomalies or component contribution anomalies in both hemispheres (Fig. S11), 52 % do
not exhibit extreme values in total radiative contribution due to the cancellation of contribution anomalies
between different components. For example, in the 70° S–80° S latitude zone (Fig. 4), the cloud
contribution in 2001 shows a positive anomaly and is the largest among the 21 years. However, since the
875 contribution from the surface and clear sky atmospheric components are negative anomalies, the total
radiative contribution does not reach extreme levels.

In the latitude zones of 0°–30°, the variability of total radiation contribution is predominantly
influenced by the anomalies in cloud component contribution, confirming previous studies that attribute
tropical albedo variability primarily to cloud variability, especially associated with the El Niño–Southern
880 Oscillation (ENSO) phenomenon (Loeb et al., 2007; Jönsson and Bender, 2022). For instance, in the 0–
10° latitude zone of the SH, the extremely high anomaly in cloud contribution in 2015 can be attributed
to the exceptionally strong and prolonged El Niño event that occurred in the east-central equatorial
Pacific during 2015/2016 (Huang et al., 2016). The persistent anomalous ascending motions and large

amounts of water vapor in the east central equatorial Pacific led to increased cloud formation (Avery et al., 2017; Lim et al., 2017), resulting in higher reflected radiation from the cloud components. Additionally, the significant positive anomaly in clear sky atmospheric contribution can be linked to smoke pollution caused by extensive fires in equatorial Asia during September–October 2015 (Koplitz et al., 2016). It is observed that the combination of positive extreme anomalies in cloud state parameters (C_{VD} and C_F) and clear sky atmospheric parameters (TCWV and AOD) greatly influences the reflected radiation contribution (Fig. S8). Although there are large negative anomalies in SM due to extreme drought in the Amazon region (Jiménez Muñoz et al., 2016), the impact of SM anomalies on the surface component contribution anomaly is limited in this primarily oceanic latitude zone. In 2010, the 20° S–30° S region was affected by a strong La Niña event, leading to anomalously heavy precipitation in Australia and South Africa and extreme positive cloud component contribution (Lim et al., 2016; Shikwambana et al., 2023). It is noteworthy that during this strong La Niña event, both the 0°–10° S and 10° S–20° S latitude zones exhibit dominant cloud contribution anomalies, but with opposite signs. A similar situation is observed during the 2015 El Niño event. This suggests the presence of some complementary mechanism between different latitudinal zones for radiative anomalies caused by such large and complex weather patterns. At 20° S–30° S, the extremely high reflected radiation contribution in 2019 is primarily contributed by the clear sky atmosphere, which may be linked to the significant aerosol emissions from severe forest fires in Australia (Khaykin et al., 2020). This is supported by Fig. S8, which indicates that the anomaly of AOD for this latitude zone in 2019 exceeds 140% of its standard deviation. In the 30° S–40° S latitude zone, although the total reflected radiation contribution is not extreme in 2019, the clear sky atmospheric contribution exhibits a positive extreme anomaly that is counteracted by a negative contribution from the cloud component. This negative anomaly in cloud contribution may be associated with the combined effects of a positive Indian Ocean Dipole (IOD) and a central Pacific El Niño on Australia during that period (Wang and Cai, 2020). At 70° S–90° S, while the surface component contributes the most to the reflected radiation (Fig. 2), it does not contribute as significantly to the variability of reflected radiation as the cloud component. Instead, in the 60°–70° latitude zone of the SH, the variation in reflected radiation contribution is primarily influenced by the surface component contribution, and its anomaly has an opposite effect to that of the cloud component anomaly. This indicates that clouds moderately mitigate the impact of sea ice changes on the total

reflected radiation contribution. The rapid expansion of Antarctic sea ice prior to 2014 results in anomalous ISC and a positive surface component contribution anomaly in this region during 2013–2014 (Riihelä et al., 2021).

The equatorial to 10° N region experiences strong negative anomalies in cloud state parameters (CF, CVOD, LWP) in 2009 (Fig. S9), leading to an extreme anomaly in the cloud component contribution. This is caused by a record-breaking warming in SST in the tropical North Atlantic starting in the summer of 2009. This warming is a typical response to ENSO and is influenced by the negative phase of the North Atlantic Oscillation (NAO) (Hu et al., 2011). In this region, 2016 is an extreme low year characterized by a negative anomaly in cloud component contribution due to the presence of a strong negative IOD and a weak La Niña (Lim and Hendon, 2017). This results in an abnormal decrease in cloudiness in the equatorial-central Pacific region. In the mid-latitudes of the NH (Fig. 5), the contribution of the clear-sky atmosphere is more prominent due to the stronger influence of human activities in this region, with sulfate aerosols being the dominant aerosol component (Diamond et al., 2022). In 2019, the 30° N–40° N latitude zone exhibits a negative anomaly in the contribution of the clear-sky atmospheric component, primarily due to a significant reduction in atmospheric aerosols over much of east-central China. This reduction is a result of emission reductions implemented during the COVID-19 outbreak as part of epidemic control measures in China (Letu et al., 2023). In the Arctic, the contribution of the surface component is minimal (Fig. 2), but it becomes the secondary dominant component in the variation of the total radiative contribution after the cloud component. However, overall, the total radiative contribution anomaly in the Arctic is still primarily influenced by the anomaly in the cloud component contribution.

In conclusion, whether in low or high latitudes, and whether considering long-term perturbations or extreme events, the impact of cloud variability on changes in the contribution of reflected radiation in different latitudinal zones cannot be ignored. Therefore, accurate modeling of the cloud component is crucial. It has been demonstrated that climate projections are sensitive to different parameterization schemes for cloud radiation (Li and Le Treut, 1992; Li et al., 2022). If the cloud parameterization scheme is not well refined, the model will struggle to accurately simulate reflected radiation at the TOA, making it challenging to explore the potential mechanisms behind the hemispheric symmetry of the PA-

3.33.2 Performance of different datasets on hemispheric asymmetry Can other radiation data reproduce hemispheric symmetry of RSR?

As mentioned in the introduction part earlier, AVHRR, ISCCP, MERRA-2, and ERA5 can provide longer-term TOA reflected SW flux RSR data compared to CERES EBAF. If these datasets can reproduce the observed hemispheric symmetry of RSR reflected radiation observed captured by CERES, it would greatly assist in identifying the underlying mechanism responsible for the hemispheric symmetry of PARSR at longer time scales and exploring how the symmetry changes with time using data spanning longer time periods.

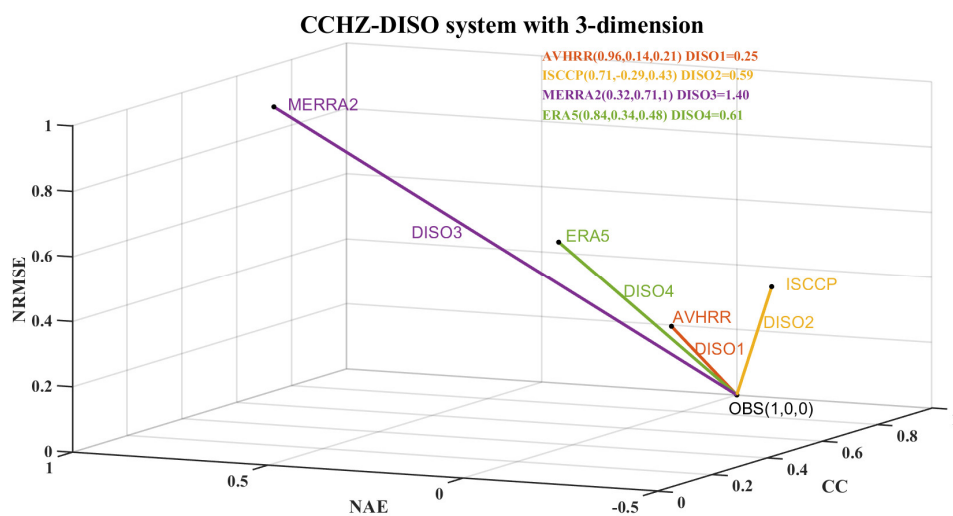
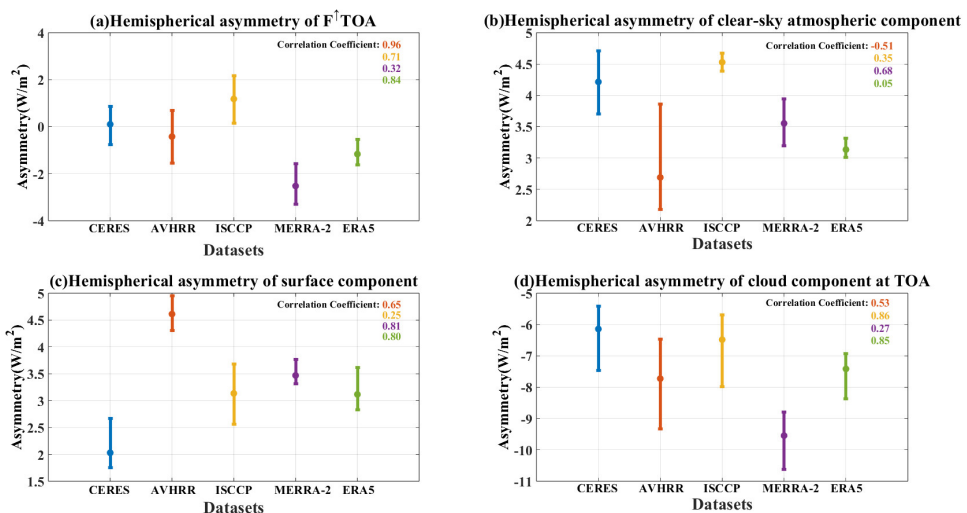
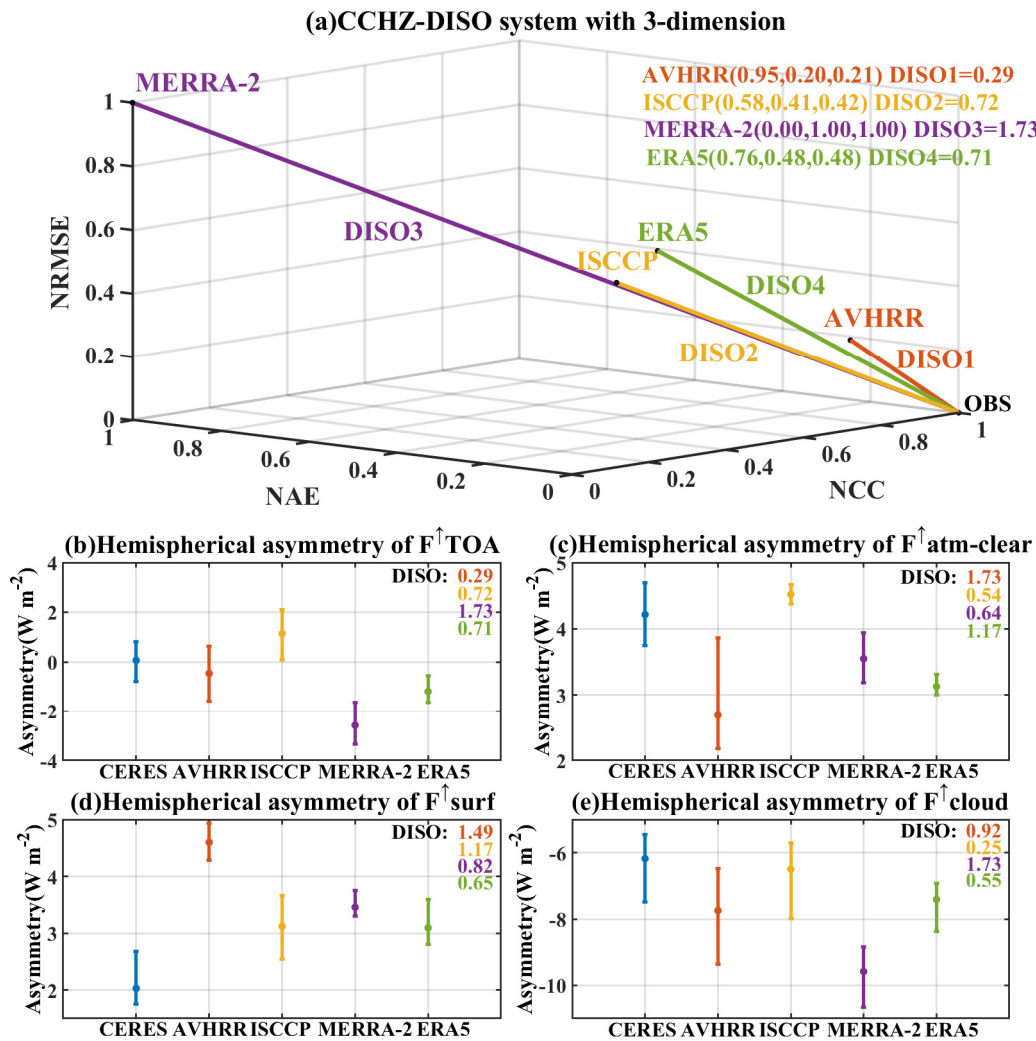


Figure 6: CCHZ-DISO system with 3-dimension. The coordinate axis consists of three statistical indicators, correlation coefficient (CC) for x-axis, normalized absolute error (NAE) for y-axis, and normalized root mean square error (NRMSE) for z-axis. OBS indicates observations, here referred to as CERES EBAF.





955 **Figure 7:** Multi-year averages of hemispheric differences in (a) TOA SW upwelling radiation flux and its (b) clear sky atmospheric, (c) surface, and (d) cloud components for the five datasets from Mar./2001-Feb./2016, with the maximum annual average difference for the dataset at the top of the error bars and the minimum at the bottom of the error bars. Blue for CERES EBAF, orange for Cloud_cci AVHRR, yellow for ISCCP, purple for MERRA-2, and green for ERA5. The numbers in the upper right corner are the correlation coefficients of time series for hemispheric differences of the different datasets with CERES EBAF. **Figure 5:** (a) CCHZ-DISO system with 3-dimension for hemispheric difference of annual-average total RSR between NH and SH. The coordinate axis consists of three statistical indicators, normalized correlation coefficient (NCC) for x-axis, normalized absolute error (NAE) for y-axis, and normalized root mean square error (NRMSE) for z-axis. OBS indicates observations, here referred to as CERES EBAF. Multi-year averages of hemispheric differences between NH and SH in (b) TOA RSR and its (c) clear-sky atmospheric, (d) surface, and (e) cloud components for the five datasets from Mar./2001-Feb./2016, with the maximum annual average difference for the dataset at the top of the error bars and the minimum at the bottom of the error bars. Blue for CERES EBAF, orange for Cloud_cci AVHRR, yellow for ISCCP, purple for MERRA-2, and green for ERA5. The numbers in the upper right corner are the DISO value of time series for hemispheric differences of different components for different datasets.

960

965

970

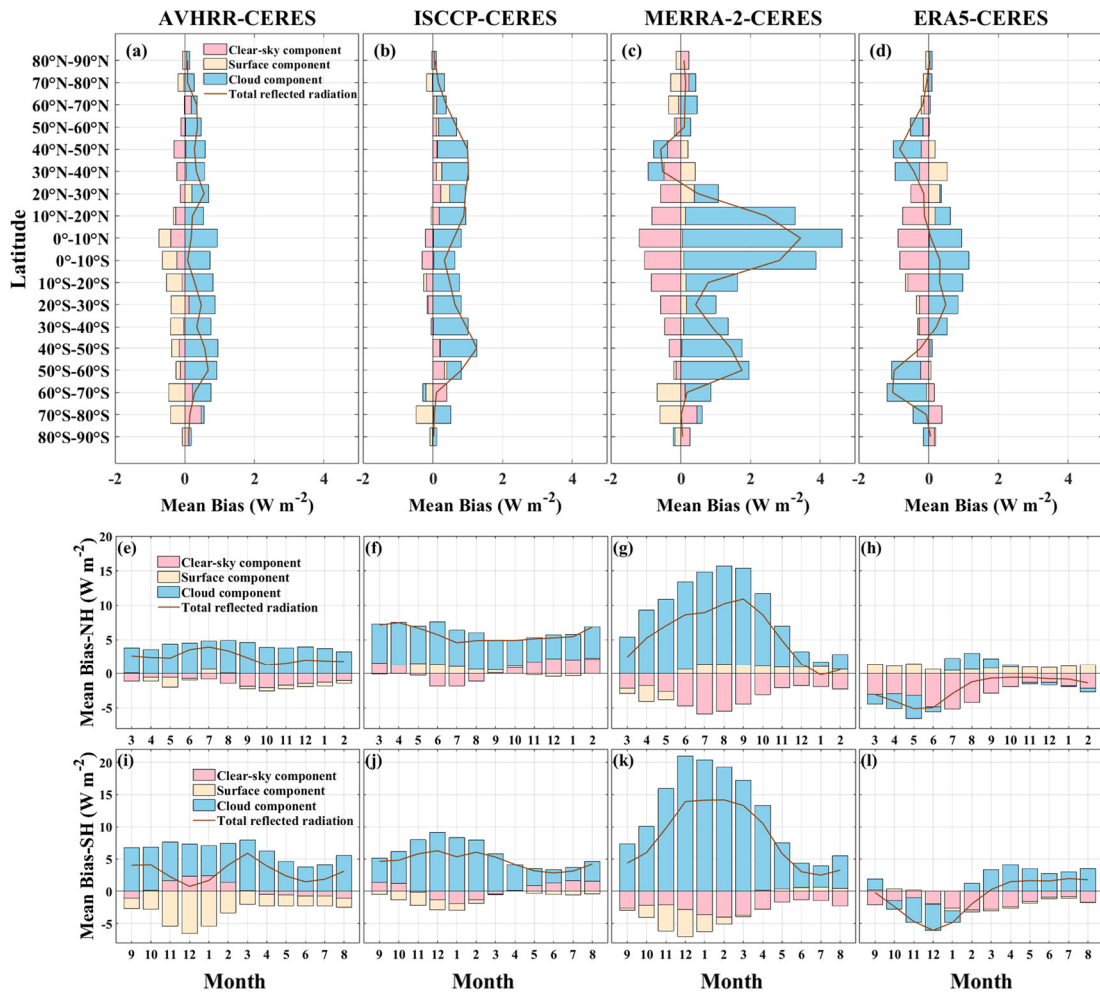


Figure 6: (a-d) Multi-year annual mean biases of total RSR and its components compared with CERES at different latitudinal zones for various datasets. Multi-year monthly mean biases of total RSR and its components compared with CERES in the (e-h) NH and (i-l) SH for different datasets from Mar./2001-Feb./2016. The columns from left to right represent the AVHRR, ISCCP, MERRA-2, and ERA5 datasets.

~~As mentioned earlier, AVHRR, ISCCP, MERRA-2, and ERA5 provide longer-term TOA reflected SW flux data compared to CERES EBAF. If these datasets can reproduce the observed hemispheric symmetry of reflected radiation captured by CERES, it would greatly assist in identifying the underlying mechanism responsible for the hemispheric symmetry of PA using data spanning longer time periods.~~

975 Therefore, ~~+~~In order to comprehensively assess the performance of each dataset for hemispheric symmetry of RSR, Figure 6-5a presents three-dimensional results based on CERES EBAF data using the CCHZ-DISO data evaluation system. ~~Different assessment metrics yield different results (Table S1), highlighting the importance of selecting appropriate assessment metrics based on the specific research needs to obtain the most suitable dataset. In general, the results indicate that AVHRR has the closest DISO value to CERES (DISO1=0.25) and exhibits the best performance in terms of hemispheric~~

980

985

990 symmetry. It is followed by ISCCP (DISO2=0.59) and ERA5 (DISO4=0.61), while MERRA-2 performs the worst (DISO3=1.40). It should be noted that the inclusion of spatial correlation coefficient in the DISO system did not significantly alter the results (Table S1e), so the three recommended metrics (CC, NAE, and NRMSE) are still used. Additionally, AVHRR demonstrates the highest correlation coefficient (0.96) with CERES for the time series of hemispheric differences in total reflected radiation, and their multi year averages are the closest (Fig. 7a). Lim et al. (2021) have shown that ERA5 exhibits good agreement with CERES in simulating the inter annual variation of global TOA SW reflected radiation. Moreover, ERA5 and ISCCP display good correlations with CERES (0.84 and 0.71, respectively), despite slight underestimation and overestimation of NH reflected radiation. Among all the datasets, MERRA-2 995 exhibits the poorest performance in terms of hemispheric symmetry, which may be primarily influenced by cloud cover bias (Lim et al., 2021).

Some datasets perform well in total reflected radiation symmetry, it doesn't mean that they also can accurately reasonably simulate the components. Here, we Figure 5b-e further decompose the TOA total RSR reflected radiation of these datasets into clear-sky atmospheric, surface and cloud components, and compare the performance of the five datasets in terms of multi-year averaged on hemispheric asymmetry (NH-SH) of RSR differences and its components (Fig. 7). Note that the good performance of dataset in hemispheric differences of RSR may also be attributed to a consistent overestimation or underestimation in both hemispheres, effectively offsetting biases between them. Additionally, the poor ability in reproducing hemispheric differences in RSR may also be attributed to biases in specific latitude zones and months. Therefore, we decompose the average biases of total RSR and its components compared with CERES for different datasets into latitude zones (Fig 6a-d) and monthly scales in NH (Fig 6e-h) and SH (Fig 6i-l) to further identify the potential error sources of in their reproduction performance of RSR hemispheric difference.

1000 Different assessment metrics used for CCHZ-DISO system can produce yield different statistical results (Table S1), highlighting the importance of selecting appropriate assessment metrics based on the specific research needs to obtain the most suitable dataset. This means that we must select the most appropriate assessment metrics based on the specific research requirements to ensure the most applicable dataset. In general, the results indicate that AVHRR has the closest DISO value to CERES (DISO1=0.25) and exhibits the best performance in terms of hemispheric symmetry. It is followed by ISCCP 1005 1010

1015 ~~(DISO2=0.59) and ERA5 (DISO4=0.61), while MERRA-2 performs the worst (DISO3=1.40). It should~~
~~be noted~~ that the inclusion of spatial correlation coefficient in the DISO system did not significantly
alter the results (Table S1c), so the three recommended metrics (NCC, NAE, and NRMSE) are still used.
In general, Fig. 5a indicates that AVHRR has the closest DISO value to CERES (DISO1=0.29) and
1020 exhibits the best performance in terms of hemispheric symmetry. It is followed by ERA5 (DISO4=0.71)
and ISCCP (DISO2=0.72), while MERRA-2 performs the worst (DISO3=1.73). The DISO assessment
metrics for the interannual series of hemispheric differences in total RSR and its component are shown
specifically in Table S2.

1025 Even in terms of multi-year average annual mean hemispheric differences (Fig. 5b), AVHRR is the
closest to CERES. In fact, the remarkable ability of AVHRR to reproduce the interannual hemispheric
symmetry of RSR from CERES is attributed to its simultaneous slightly overestimation of RSR in both
hemispheres (Fig. 6a). Biases in hemispheric differences among different components cancel each other
out, explaining this statistical result. It is clear that the hemispheric asymmetry of the three components
of the AVHRR differs significantly from that of CERES. Figure 5c shows that ~~Although AVHRR exhibits~~
1030 ~~well symmetry in the total reflected radiation, it shows considerable deviation biases from CERES in the~~
~~hemispherical asymmetries difference of three components. AVHRR exhibits a brighter SH than that of~~
~~CERES, due to its clear underestimation of the clear sky atmospheric component contribution in the NH~~
~~and an overestimation of the cloud component contribution in the SH. AVHRR significantly~~
~~underestimates the hemispheric asymmetry of the clear-sky atmospheric component, however, the bias~~
1035 ~~of the clear-sky atmospheric component of AVHRR in different latitudinal zones is not as large as that~~
~~of MERRA-2 and ERA5 (Fig. 6). The largest bias in hemispheric asymmetry and the highest DISO value~~
~~for the clear-sky atmospheric component of AVHRR are mainly due to the fact that: (1) the clear-sky~~
~~atmospheric component of AVHRR exhibits a certain bias versus CERES in NH but is minimal in SH,~~
~~resulting in the interhemispheric bias not canceling each other out as observed in other datasets (Fig. 6a);~~
1040 ~~(2) Particularly, it significantly overestimates the surface component of the NH. Interestingly, AVHRR~~
~~also fails to capture the interannual variations in the hemispheric differences of the clear-sky atmospheric~~
~~component as observed by even demonstrates a negative correlation (-0.51) with CERES concerning~~
~~hemispheric differences in the clear sky atmospheric component, and the data itself displays a high~~

1045 degree of annual dispersion. This ultimately leads to poor temporal correlation coefficients in the DISO
calculations (CC=-0.52), resulting in its largest DISO value among all datasets for clear-sky atmospheric
component (DISO=1.73). This bias of clear-sky atmospheric component in AVHRR versus CERES ~~This~~
~~can be attributed, in part, is partly due to the limitations of the current version of AVHRR dataset~~
underestimates the high aerosol loading condition ~~version regarding aerosols, due to~~ The aerosol optical
thickness in this dataset is set at 0.05 (Stengel et al., 2020), which is considered as an underestimation
for high aerosol load situations ~~(Stengel et al., 2020). Furthermore, AVHRR exhibits the poorest~~
performance in terms of hemispheric differences in surface components (Fig. 5d, DISO=1.49). It
overestimates the multi-year average hemispheric differences of surface components by more than twice
compared to CERES (Fig. 5d), which mainly originate from the underestimation of the surface
component by AVHRR only in the SH (Fig. 6a). Furthermore, AVHRR notably overestimates the surface
component due to in the NH. ~~It is mentioned in the The ESA Cloud_cci Product Validation and~~
Intercomparison Report (PVIR) PVIR ~~mentions~~ that the Cloud_cci dataset exhibits higher biases in TOA
upwelling shortwave flux ~~RSR~~ compared to CERES in regions with low vegetation coverage and
typically high surface albedo. In terms of cloud component, AVHRR slightly overestimates it in both
hemispheres, particularly in the SH (Fig. 6a), thus ~~Additionally, AVHRR exhibits obvious~~
bias ~~demonstrates a significant deviation~~ from CERES in the hemispheric differences (Fig. 5e) of the
cloud component. ~~Stengel et al. (2020) highlighted pointed out~~ that AVHRR PMv3 shows a greater bias
in identifying liquid clouds and reducing ice water paths compared to v2.

1065 Although the overall performance of ISCCP in reproducing the hemispheric symmetry of total RSR
is comparable to ERA5 (DISO_ISCCP=0.72; DISO_ERA5=0.71), it is the only dataset that
overestimates the multi-year mean hemispheric difference of total RSR (Figure 5b), because it
overestimates the RSR in NH more than in SH (Figure 6b). Additionally, its the multi-year means of the
hemispheric differences for all three components are closest to that of CERES among the datasets.
However, the time series of annual means for the its annual mean hemispheric difference of in the clear-
sky atmospheric component and the surface component shows poor temporal correlation with CERES
(CC=0.25), thus exhibiting the larger DISO (DISO=1.17). On the other hand, ISCCP performs well best
in evaluating reproducing the hemispheric differences in of the clear-sky atmospheric component
(DISO=0.54) and the cloud component (DISO=0.25), showing close agreement and a strong correlation

with CERES (0.86). Previous studies have indicated that ISCCP employs a visible adjustment to correct for IR emission through thin cirrus clouds, which enhances the accuracy of cloud top pressure retrievals for single layer cirrus clouds (Marchand et al., 2010). Additionally, the inclusion of the Max Planck Institute Aerosol Climatology (MAC) in the treatment of stratospheric and tropospheric aerosols within the ISCCP-H series helps reduce the misidentification of aerosols as clouds (Young et al., 2018), thereby improving the simulation of clear-sky atmospheric components. Moreover, Fig. 6b shows that ISCCP overestimates the cloud component in both hemispheres, the offsetting effect results in a hemispheric difference in cloud component that is closest to CERES. However, the aerosol input dataset MAC v2, despite improving cloud simulation, suffers from significant errors and uncertainties (further details in the 'ISCCP-FH Radiative Flux Profile Product C-ATBD'). This may explain the lack of correspondence between the hemispheric differences in the clear-sky atmospheric components of ISCCP and CERES. Nevertheless, ISCCP still exhibits biases in cloud retrieval. For instance, Boudala and Milbrandt (2021) discovered that ISCCP data overestimates cloud cover in both hemispheres between approximately 40° and 60° latitude, particularly in North America and Europe, but significantly underestimates cloud cover in the tropics and high latitudes in both hemispheres. Furthermore, ISCCP also overestimates the total cloud fraction of TP compared to other space-based lidars (Zhao et al., 2023).

The two reanalysis datasets exhibit quite different performance in simulating hemispheric differences in the total RSR and its three components. Among all the datasets, MERRA-2 exhibits poorest in terms of hemispheric symmetry of RSR (Fig. 5a), which may be primarily influenced by cloud cover bias (Lim et al., 2021). Indeed, MERRA-2 poorly models the hemispheric difference in the cloud component (DISO=1.73), whereas ERA5 demonstrates shows good agreement and correlation with CERES (DISO=0.55). The latitudinal distribution of the RSR bias reveals that although the underestimation of the clear-sky atmospheric component partly offsets the significant overestimation of the cloud component, the total RSR bias of MERRA-2 is still the largest in all datasets, especially in SH (Fig. 6c). Hinkelman (2019) pointed out that the discrepancy in of all-sky RSR reflected SW radiation flux at TOA between MERRA-2 and EBAF is attributed to differences in cloud variables such as cloud fraction or optical depth. In MERRA-2, there is an excessive presence of clouds over tropical oceans and a slight underestimation of clouds in the oceanic stratocumulus region, as well as an overestimation of clouds in the Southern Ocean (Hinkelman, 2019). It has been shown that MERRA-

2 systematically consistently underestimates the total cloud cover across almost all areas of the TP at all times (Deng et al., 2023) and altitudes (Zhao et al., 2023). This bias may stem from a flaw in the cloud parameterization (e.g., cumulus parameterization and convective cloud schemes) within the reanalysis assimilation model (Dolinar et al., 2016; Li et al., 2017). Besides, MERRA-2 also exhibits significant biases in the clear-sky atmospheric component in different latitudinal zones compared to other datasets (Fig. 6c), but the bias of its hemispheric asymmetry is smaller due to the inter-hemispheric cancellation. When assessing the cloud properties of reanalysis data over East Asia, Yao et al. (2020) found that ERA5 and MERRA-2 generally overestimate liquid clouds, with MERRA-2 also overestimating ice clouds over the cyclone center. Nevertheless, ERA5 still exhibits good consistency correlation with CERES, except for the hemispheric difference in the clear-sky atmospheric component (DISO=1.17). Li et al. (2023) demonstrated that the deviation of ERA5's surface solar radiation products from observed values increases with higher aerosol loading, indicating that aerosols have a significantly impact affect on the accuracy of ERA5's radiation products, which may affect the calculation of the clear sky component. Furthermore, the cumulative annual mean time series of hemispheric differences in the cloud component for ISCCP and ERA5 display similar variations to CERES, with ISCCP exhibiting a smaller bias. However, the cumulative annual mean time series of hemispheric differences in the surface component for ISCCP differs from all other datasets, as its hemispheric difference increases after the 5 year average but ultimately converges to a constant at longer time scales as others. The cumulative annual mean of hemispheric differences in the clear sky atmospheric component for AVHRR, ISCCP, and MERRA-2 exhibits similar characteristics to CERES, with a pronounced change, illustrating the irregularity of human activities. In contrast, ERA5 shows a consistent decline.

Compared to other datasets, AVHRR exhibits smaller positive biases versus CERES in the multi-year latitude-zone-averaged total RSR (Fig.6a). It is a result of the widespread overestimation of cloud components across all latitude zones globally, which is offset by the underestimation of clear-sky atmospheric components in the NH and surface components in the SH. In the NH, the AVHRR data may misidentify high aerosol loads as clouds, thus underestimating clear sky atmospheric components in NH with rich dust and anthropogenic aerosol and overestimating the cloud component (more details are described in PVIR). The surface component in the SH shows a significant negative bias compared to that of NH. This is mainly due to the different surface albedo retrieve algorithms and input surface parameters

of AVHRR for land and ocean (more details are described in “ESA Cloud cci Algorithm Theoretical Baseline Document v6.2”). Compared to CERES, AVHRR systematically overestimates the surface albedo of land at low and middle latitudes and underestimates the surface albedo of the oceans and polar regions (Fig. S11). This is why the surface component of AVHRR exhibits a significant underestimation in the SH compared to CERES. In the NH, the surface component biases for land and ocean cancel each other out and therefore contribute little to the total RSR bias. From a monthly scale perspective, the overestimation of cloud components by AVHRR is present in all months in both hemispheres. The underestimation of clear-sky atmospheric components in the NH is particularly pronounced during autumn and winter (Fig. 6e), while the underestimation of surface components in the SH is most significant in November, December, and January (Fig. 6i), which is related to the seasonal variation in the incident solar variation and surface albedo biases.

Compared to CERES, ISCCP exhibits the most significant mean bias in the 40°-50° latitude zones in both hemispheres, primarily driven by the overestimation of cloud component (Fig. 6b). The ISCCP data combines observational data from geostationary satellites in low- and mid-latitude regions, thus the higher viewing zenith angle compared to low-latitude regions introduces greater uncertainty in the retrieval of cloud fractions in mid-latitude regions (Evan et al., 2007; Marchand et al., 2010; Norris and Evan, 2015; Boudala and Milbrandt, 2021), consequently resulting in larger cloud component biases. Boudala and Milbrandt (2021) found that ISCCP overestimates cloud cover between approximately 40° and 60° latitudes in both hemispheres, particularly in North America and Europe. In the NH, the bias from cloud component shows no significant seasonal variation (Fig. 6f) as in the SH, which is larger from late spring to summer (Fig. 6j). Although ISCCP demonstrates minimal average bias in surface components across almost latitude zones except for 70°S-80°S (Fig. 6b), its combined performance in hemispheric differences of surface component is relatively poor (DISO=1.17). This is because DISO is a comprehensive assessment based on three metrics (NCC, NAE, NRMSE), whereas ISCCP's hemispheric difference of surface components exhibit poorer temporal correlation with CERES (CC=0.25), indicating its limited ability to capture the interannual variations of surface components.

For the MERRA-2, the zonal-averaged total RSR exhibit most significant biases compared to other datasets, particularly positive mean bias in the latitude 0-20° in both hemispheres and 30°S-60°S, primarily attributed to a considerable overestimation of cloud component (Fig. 6c). Previous study also

1160 [pointed to excessive cloud cover over tropical oceans and the Southern Ocean has in MERRA-2](#)
[\(Hinkelman, 2019\). The lack of cloud and radiation-related data assimilation also have introduced](#)
[uncertainties in the simulated RSR in MERRA-2 \(Yao et al., 2020\). The significant positive bias in cloud](#)
[component in the mid-latitudes of the SH may be due to the fact that MERRA-2 overestimates the](#)
[frequency of supercooled liquid clouds over the Southern Ocean during the summer \(Kuma et al., 2020\).](#)
1165 [Furthermore, its underestimation of clear-sky atmospheric components is mainly concentrated in the low-](#)
[and mid-latitudes, especially in the tropics, and exhibits a hemisphere-symmetrical bias. This partially](#)
[explains its better performance in reproducing hemispheric differences of clear-sky atmospheric](#)
[components, as the biases between hemispheres can offset each other. The inability to effectively](#)
[distinguish cloudy and clear-sky conditions for high aerosol loadings scenarios \(Trollet et al., 2018\) and](#)
1170 [the lack of emission data in the aerosol model of MERRA-2 \(Buchard et al., 2017\) may lead to a](#)
[significant underestimation of high AOD values, hence underestimate the clear-sky atmospheric](#)
[components. Additionally, the RSR bias from MERRA-2 also shows notable monthly variations \(Fig. 6g,](#)
[and 6k\). On the one hand, it links to the seasonal variation of incident solar radiation mean biases, while](#)
[the temporal correlation of between RSR mean biases and incident solar radiation is 0.68 and 0.64 in NH](#)
[and SH, respectively. On the other hand, the positive mean biases of RSR are driven by the positive cloud](#)
1175 [component biases. The positive cloud component bias in the NH reaches over \$10 \text{ W m}^{-2}\$ from May to](#)
[October, with the peak in late summer \(August, bias= \$14.29 \text{ W m}^{-2}\$ \), while in the SH, the bias generally](#)
[exceeds that of the NH from October to April, with the peak in early summer \(December, bias= \$20.94 \text{ W}\$](#)
[m⁻²\). Moreover, MERRA-2 significantly underestimates surface components in Antarctica during](#)
1180 [melting season \(November to January\), which could be due to biases in the input snow products that](#)
[introduce significant uncertainties in surface albedo \(Jia et al., 2022\).](#)

[For the ERA5, the total RSR between \$10^{\circ}\text{N}\$ and \$40^{\circ}\text{S}\$ is overestimated compared to that of CERES,](#)
[while at other latitudes the RSR is underestimated, which primarily driven by cloud component biases](#)
[\(Fig. 6d\). Previous research indicated that ERA5 systematically overestimates high cloud fraction in the](#)
1185 [tropical convective regions \(Wright et al., 2020\) while underestimating liquid and ice water paths of](#)
[clouds in the Arctic \(Jenkins et al., 2024\). In terms of the hemispheric monthly biases, the overestimation](#)
[of cloud component in the SH mainly occurs during the autumn and winter seasons \(Fig. 6l\). Apart from](#)
[the high latitudes in the SH, ERA5 shows underestimation of clear-sky atmospheric components across](#)

all latitude zones, especially in the tropics, which may be attributed to inadequate representation or simulation of aerosols and aerosol-cloud interactions in ERA5 (Jiang et al., 2020). This may be related to the shortcomings of ERA5's aerosol assimilation process, which only considers aerosol climatology as input, overlooking aerosol variations on interannual time scales (He et al., 2021). Surprisingly, apart from overestimation in the 20°N-50°N region, the multi-year averaged surface component of ERA5 basically the same as CERES. Jia et al. (2022) also pointed that ERA5 captures changes in snow albedo at mid and high latitudes better than other reanalysis data.

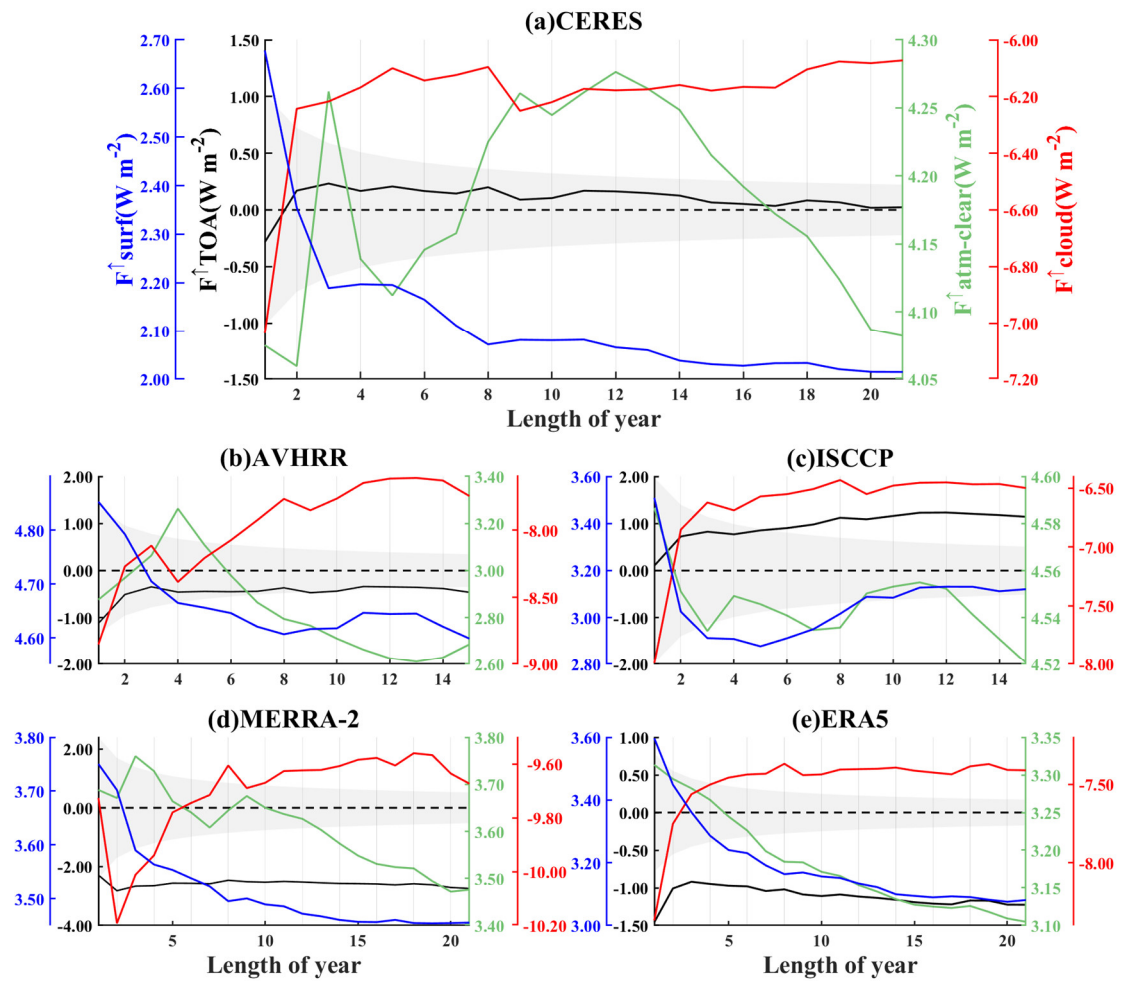


Figure 7: Cumulative annual mean for hemispheric differences of RSR and its components for (a) CERES, (b) AVHRR, (c) ISCCP, (d) MERRA-2 and (e) ERA5. That is, when Length of year=N, the hemispheric differences (NH-SH) of annual mean RSR are calculated from 2001 to 2000+N. The range of N varies due to the different record lengths of the datasets, with $1 \leq N \leq 21$ for CERES, MERRA-2 and ERA5, while for AVHRR and ISCCP, $1 \leq N \leq 15$. The black colour indicates the hemispheric difference of the total RSR, while the blue, green, and red colours correspond to the hemispheric differences of the three components, respectively (as y-axis labels in a). The shaded areas are the uncertainties of hemispheric difference of RSR for the given dataset. If the solid black line is within the shaded area, it indicates that the hemispheric symmetry in total RSR is credible within the uncertainty.

In a recent study, George and Bjorn (2021) argued pointed out that the symmetry of albedo cannot be established on an annual or sub-annual scale, but rather on larger spatial and temporal scales. It prompts us to find out what time scale for these datasets can be used for the study of hemispheric symmetry of PA. In following analysis, we use radiation datasets from different sources to investigate the appropriate time scale for studying the hemispherical symmetry of RSR. Figure 7 illustrates the variation of multi-year average hemispheric differences of RSR and its components over the cumulative length of the year (N) for different datasets, i.e. the N-year averaged hemispheric difference of RSR. ~~In a recent study, George and Bjorn (2021) argued that the symmetry of albedo cannot be established on an annual or sub-annual scale, but rather on larger spatial and temporal scales.~~ Figure 7a shows that the hemispheric differences in total RSR and its components observed by CERES are tending to stabilize over time, except for the clear-sky atmospheric component. The hemispheric asymmetry of clear-sky atmospheric component exhibits a strong perturbation over time, which may be closely related to human activities or natural perturbations, particularly the highly variable emissions of anthropogenic aerosols and irregular occurrences of large-scale volcanic eruptions and forest fires (Minnis et al., 1993; Diamond et al., 2022). ~~To better investigate the performance of hemispheric symmetry in the reflected solar radiation across different datasets, Figure S12 illustrates the variation in multi-year average hemispheric differences of the reflected radiation and its components over time. We aim to determine the timescale suitable for studying the hemispheric symmetry of PA using these datasets. Since there was no clear quantification previous studies lacked a clear definition of the PA's hemispheric symmetry of RSR in the previous studies,~~ we ~~try to~~ will discuss this issue here. Voigt et al. (2013) conducted a random division of the Earth into two halves to assess whether these random pairs exhibited hemispheric symmetry in ~~reflected solar radiation~~ RSR. The results revealed that only 3% of the random pairs demonstrated a hemispheric difference in ~~reflected radiation~~ RSR smaller than 0.1 W m^{-2} , as measured by CERES-EBAF. Furthermore, even when this criterion was extended tenfold (1 W m^{-2}), only 31% of the random pairs satisfied the hemispheric symmetry requirement. Stephens et al. (2015) noted that the multi-year averaged hemispheric difference in ~~reflected solar radiation~~ RSR between the NH and SH is less than 0.2 W m^{-2} , suggesting this as an indicator of hemispheric symmetry. Here, when we use a symmetry criterion of 0.1 W m^{-2} , CERES achieves hemispheric symmetry of ~~reflected radiation~~ RSR on a ~~1615~~-year annual mean scale, while none of the other datasets do. When we expand this symmetry criterion to 0.2 W m^{-2} ,

1235 the symmetry study application of CERES is around 9-year scale, and other datasets remain inapplicable. When held to a more conservative standard of 1 W m^{-2} , CERES achieves hemispheric symmetry every year, and AVHRR achieves it on scale of more than two years. Interestingly, the ISCCP exhibits increasing hemispheric asymmetry ~~as the time span extends with longer durations~~, only declining after a 13-year average. ~~Similar~~, ERA5 also displays a similar but more moderate increase in hemispheric asymmetry.

1240 In addition, in order to have a more rigorous standard, ~~the study we would like to~~ takes the uncertainty of the instrumental measurements into account. ~~That is, if~~ the RSR difference between ~~the solar radiation reflected from the~~ NH and SH is within the uncertainty of the measurement, it is considered as hemispherical symmetry (Diamond et al., 2022). The regional averaged monthly mean uncertainty of the ~~reflected SW radiation~~ RSR at the TOA ~~of from~~ the CERES EBAF is 2.5 W m^{-2} (Loeb et al., 2018b). ~~Considering CERES as the true values, the monthly regional mean biases of~~ AVHRR, ISCCP, MERRA-2 and ERA5 ~~have monthly regional mean biases from the CERES of~~ are 3.3 W m^{-2} , 4.8 W m^{-2} , 5.9 W m^{-2} and -1.9 W m^{-2} , respectively, which will be used to calculate their uncertainties. Here we follow the method of Jönsson and Bender (2022) to calculate the uncertainty of hemispheric difference of ~~reflected solar radiation flux~~ RSR. ~~Here, it is~~ noting that only rough calculations have been made due to the unavailability of uncertainties at different grid points around the globe. Uncertainty in the time-mean over the N-month period is scaled by a factor of $N^{-1/2}$. Then ~~there is~~ we can obtain a time series of the uncertainty in the hemispherical differences of ~~reflected radiation~~ RSR for each dataset (~~Fig. S12~~). It is clear that as time grows, the range of uncertainty shrinks. Note that if the solid black line falls within the shaded area (~~see Figure 7~~), it indicates that the ~~total reflected radiation~~ RSR exhibits credible hemispheric symmetry within the given uncertainty. ~~It is clear that The~~ the hemispherical difference of the total ~~reflected radiation~~ RSR from CERES remains well within its uncertainty range (~~not shown~~). Similarly, AVHRR ~~stays well within its~~ demonstrates good agreement with uncertainty over a 14-year timescale. ~~But~~ On the other hand, ISCCP only ~~keeps within uncertainty~~ maintains this agreement on timescales up to 5 years. The reanalyzed datasets significantly deviate from their respective uncertainty ranges. ~~In summary, AVHRR shows better consistency with CERES regarding the hemispheric symmetry of the total reflected radiation.~~

In summary, AVHRR shows better agreement with CERES in terms of the hemispheric symmetry

of RSR. Furthermore, the cumulative annual mean time series of hemispheric differences in the cloud component for ISCCP and ERA5 display similar variations to CERES (CC_ISCCP=0.96; CC_ERA5=0.95), while ISCCP exhibits a smaller bias (AE_ISCCP=0.41; AE_ERA5=1.29). However, in the term of the cumulative annual mean time series of hemispheric differences for the surface component, only ISCCP fails to reproduce the CERES observed variation, and its CC with CERES is 0.5 (insignificant), while the CCs of the other datasets are all greater than 0.95. For the cumulative annual mean of hemispheric differences in the clear-sky atmospheric component, although AVHRR, ISCCP, and MERRA-2 show similar abrupt variability patterns to CERES, indicating the irregularity of human and natural activities, they do not correlate well with CERES, with CCs of -0.63, -0.38, and 0.25, respectively. In contrast, ERA5 shows a continuous decrease trend, and correlates poorly with CERES, with a CC of -0.24, which also verifies its poor modelling ability in the clear-sky atmospheric component.

~~On the whole, if the focus is solely on studying the hemispheric symmetry of total reflected radiation, AVHRR can be chosen, although it exhibits poor performance in simulating the hemispheric differences of the components. Conversely, ISCCP can be utilized for studying the hemispheric asymmetry in the cloud component of reflected radiation. Generally, there is scope for improvement in simulating the components of reflected radiation in these datasets. Further research and algorithmic enhancements may be required to address these issues and enhance the usability and accuracy of these datasets in studies related to hemispheric symmetry.~~

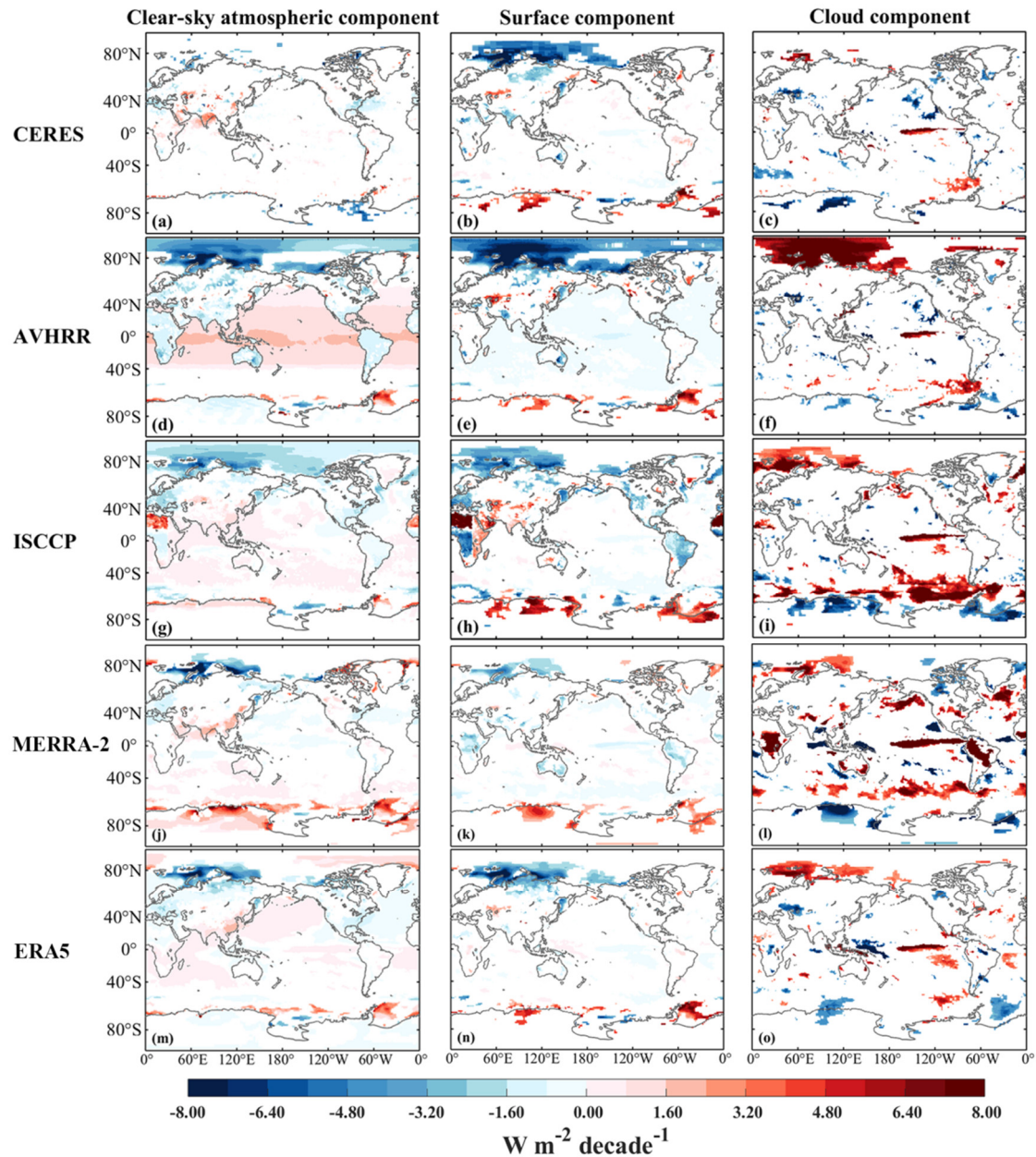


Figure 8: Trends in TOA RSR flux of the clear-sky atmospheric component (left column), surface component (centre column) and cloud component (right column) for Mar./2001-Feb./2016. (a-c) CERES, (d-f) AVHRR, (g-i) ISCCP, (j-l) MERRA-2, and (m-o) ERA5.

Figure 8 further illustrates the global distribution of the long-term trends in the RSR of three components from CERES, AVHRR, ISCCP, MERRA-2 and ERA5. Note that the trend analysis is based on de-seasonalized monthly time series from March 2001 to February 2016.

For the regional trends of clear-sky atmospheric components, there are significant differences among the five datasets. Compared to CERES, the other four datasets exhibit some spurious trends over the oceans, especially AVHRR. Such a large difference in the trend distribution under clear-sky

conditions between AVHRR and CERES may be due to different methods of estimating the mean clear-sky fluxes. The clear-sky radiative fluxes of CERES are based on clear-sky conditions only (and interpolate the collected clear-sky radiative fluxes to cloudy pixels), whereas AVHRR takes into account all the conditions (but removes the clouds) (Stengel et al., 2020). ISCCP, MERRA-2, and ERA5 all capture a significant positive trend over India well, whereas AVHRR shows the opposite trend. Over the Arctic, both AVHRR and ISCCP show widespread of significant negative trends, which are not obviously seen in CERES and reanalysis data. ISCCP suggests a significant positive trend in clear-sky atmospheric component over North Africa, which is not presented by other datasets. For trends of surface component, the ERA5 is relatively consistent with CERES over the land but exhibits more spurious signals over the oceans. Despite some similarities in trend distribution of surface components on land between AVHRR and ERA5, there are widespread spurious decreasing trends similar to that of clear-sky atmospheric components over Arctic for AVHRR. All datasets show significant negative trends over the Arctic, but with different magnitudes and ranges. ISCCP shows significant positive trends of surface component over Central Africa, with opposite trends in North Africa and South Africa. These anomalous trends may be influenced by geometry artifacts observed by satellites. The ISCCP dataset uses input parameters from a series of geostationary satellites, and the edges of satellite views may generate spurious variability (Evan et al., 2007). We selected a grid in North Africa with the strongest positive trend and examined its de-seasonalized monthly anomaly time series (Fig. S12). There is a sudden increase of RSR in July 2006 and since then there has been a persistent positive anomaly. This abrupt change explains strong trend in the RSR component in the African region. We speculate that this may be attributed to a sudden change in the geostationary observation platform (Evan et al., 2007). Over South America, ISCCP and MERRA-2 exhibit significant negative trends, which are not observed in other datasets. In addition, snow cover is a significant source of error in surface albedo in reanalysis data (Jia et al., 2023). This could be a key reason for MERRA-2's failure to capture the declining trend in surface components in northern Russia. For trends of cloud component, all datasets find a significant increase over the equatorial central-eastern Pacific. However, except for AVHRR, the other datasets fail to capture the negative trend near the east Pacific adjacent to North America. Furthermore, compared to CERES, AVHRR and ISCCP have produced many unreal trends over polar regions. And every dataset mis-estimates the trend values in most regions. This indicates that these datasets still require improvement in handling cloud

parameterization schemes, which is a significant source of uncertainty in their cloud components.

1325 In terms of interannual hemispheric trends of RSR and its components (Table S3), all four datasets fail to capture the decreasing trend in total RSR for both hemispheres, and ISCCP and MERRA-2 even show an increasing trend in both hemispheres. For three components, AVHRR significantly overestimates the positive trend in clear-sky atmospheric component and the negative trend in surface component in the NH. On the contrary, ISCCP, MERRA-2, and ERA5 fail to reproduce the decreasing trends in cloud components for both hemispheres and even show opposite trends.

1330 In summary, ~~On the whole,~~ if the focus of study is solely on the long-term changes in ~~studying the~~ hemispheric symmetry of total ~~reflected radiation~~ RSR at TOA, AVHRR is the preferred choice. However, it is not recommended to use AVHRR for decomposing the RSR into components. ~~can be chosen, although it exhibits poor performance in simulating the hemispheric differences of the components. Conversely,~~ Additionally, ISCCP can be ~~utilized~~ used to investigate long-term ~~for studying the hemispheric~~ asymmetry changes and its mechanisms in the cloud component of reflected radiation. Generally, there is scope for improvement in simulating the components of reflected radiation in these datasets. Further research and algorithmic enhancements may be required to address these issues and enhance the usability and accuracy of these datasets in studies related to hemispheric symmetry.

4 Discussion and Summary

1340 The hemispheric symmetry of ~~RSR the PA~~ is a powerful feature of the Earth-atmosphere system, and the mechanisms by which it is currently maintained remain unclear, posing a great challenge for improving the simulation of hemispheric symmetry of RSR in climate models. Numerous scholars have proposed many possible compensatory mechanisms, and many of the different mechanisms are not only limited by latitude but also have seasonal characteristics, ~~and if~~ If we resolve the energy down to monthly scales and latitudinal zones, we can gain insight into the changes of RSR at finer spatial and temporal scales and further improve the understanding of potential regional-scale mechanism for hemispheric symmetry of RSR. ~~capture more variations in the mechanisms. Accordingly based on the TOA and surface radiative flux data from CERES EBAF during March 2001 to February 2021, we build on the original interannual variability and further explore the contribution and monthly variability of different~~

1350 ~~latitudinal zones as well as the variability of the different components across latitudinal zones, and~~
~~moreover the manifestation of hemispheric symmetry for the different datasets.~~ In addition, we also
evaluate the applicability of radiation datasets with longer records in studying hemispheric symmetry
over time. The main findings~~results~~ are as follows:

1355 (1) RSR shows a decreasing trend in both hemispheres across almost all months and all latitudinal
zones, with differing primary driven factors. In the NH, the interannual hemispheric decreasing trend is
jointly influenced by decreasing trends of the three components, while in the SH, only the cloud
component exhibits a significant decreasing trend. Monthly trends indicate a slowdown in the decreasing
trend from spring to winter, with the maximum trend occurring in the spring (April in NH and October
1360 in SH). For the NH, most of the downward trend in RSR originates from 30°N-50°N, with extremes in
the 30°N-40°N. At 30°N-50°N, the trend is attributed to a significant decrease in both the cloud and clear-
sky atmospheric components. The decreasing in the clear-sky atmospheric component is due to reduced
emissions of anthropogenic sulfate aerosols from various regions and a weakening of dust activities
during spring and summer in parts of the dust belt. The decreasing trend in the cloud component is
1365 concentrated near the eastern Pacific and North Atlantic close to North America, which is may be
associated with a shift in the PDO phase from negative to positive, which leads to warmer SSTs in parts
of the eastern Pacific, thus significantly reducing low cloud cover and RSR. For the SH, the significant
decreasing trends of RSR is mainly occur in the 0°-50°S, which is entirely dominated by the significant
decreasing trend in the cloud component. This reduction in cloud component is mainly observed over the
1370 south tropical western Pacific as well as over the wider Southern Ocean, attributed to the reduction in
cloud cover. Unlike the three components of RSR in the NH, there is no significant trend in the proportion
of their contribution rates, indicating that there is no significant adjustment in the radiation budget in the
NH. The contribution rate of the clear-sky atmospheric component in the SH is increasing, while that of
the cloud component is decreasing. Notably, the contribution rate of total RSR from the 30°N-40°N to
1375 the hemisphere has significantly decreased, primarily due to a reduction in the contribution of the clear-
sky atmosphere component.~~(1) The total reflected SW radiation at the TOA shows a clear hemispheric~~
~~symmetry in the long-term trend of the annual and the multi-year average. The annual mean decreasing~~
~~trend in the NH is synergistically influenced by changes in Arctic snow and ice, reduction in~~

1380 anthropogenic aerosols at mid latitudes, and a decrease in low cloud cover in the Eastern Pacific. In
contrast, the decreasing trend in the SH is mainly due to the cloud component. The cumulative year to
year averaging of the hemispheric differences in reflected radiation and its components tend to be
constant over time, yet the clear sky atmospheric component displays great variability owing to human
activities. More cloud component contribution from 0°N-10°N and more clear sky atmospheric and
1385 surface component contribution from 10°N-60°N compared to the corresponding latitude zones in SH,
result in the dominance of NH reflected radiation at 0°-40°. However, greater surface component
contribution from higher latitude zones in the SH and significantly higher cloud contribution from 10°S-
70°S compensate for this, resulting in the reflected radiation of SH leading that of the NH in 50°-90°.
Within the latitudinal zones from the equator to 40°, the annual cycle of reflected radiation contribution
is distinguished by a high in fall/winter and a low in spring/summer, with higher contribution in the NH
1390 than in the SH. Nonetheless, beyond 50°, this pattern is reversed entirely. This feature of the annual cycle
in various latitudes is linked to that of the incident radiation and is mainly contributed by the cloud and
clear sky atmospheric component at low mid latitudes, and by the surface component at high latitudes.
At high latitudes, the peak of the surface component contribution in the NH is one month earlier than in
the SH due to surface albedo and Arctic amplification effects. From the perspective of hemispheric
1395 difference, the annual cycle of total reflected radiation and its interannual variability are almost drive
from those of cloud component contribution in mid low latitudes, and from surface and cloud
contributions in high latitude zones.—

(2) In extreme anomaly years across all latitudinal zones, the primary factor is the cloud component
1400 contribution, followed by the surface component, and then the clear sky atmospheric component. Surface
component anomalies play a larger role in extreme events in the SH, particularly in the 60°S-70°S. It is
common to observe cancellation of contribution anomalies between different components and latitudinal
zones during extreme events. The effect of cloud variability on the variation of reflected radiative
contributions of different latitudinal zones is not negligible at both low and high latitudes, for both long-
1405 term perturbations and extreme events, and is evidently influenced by large scale weather patterns such
as ENSO and PDO.

(32) According to the [DDZJCCHZ](#)-DISO assessment system, AVHRR performs best in terms of

hemispheric symmetry of RSR, followed by ERA5+ISCCP and ERA5,ISCCP, and the worst is MERRA-2. The outstanding performance of AVHRR in hemispheric difference of RSR is due to its simultaneous slight overestimation of both hemispheres, driven by offsetting biases in different components. While AVHRR performs worst in capturing the hemispheric difference of clear-sky atmospheric and surface components, its component biases in different latitude zones are in fact smaller than those of other datasets, except that they are asymmetric and therefore do not offset between two hemispheres. In contrast, ISCCP performs best in reproducing CERES-observed hemispheric differences of clear-sky atmospheric and cloud component, but shows positive bias in the cloud component in the mid-latitudes, possibly influenced by the field of view of geostationary satellites. The total RSR bias between MERRA-2 and CERES is mainly concentrated in the 20°N-20°S and 40°S-60°S, with extreme values in the summer, dominated by the large overestimation of cloud components. ERA5 is the best dataset for reproducing hemispheric difference of surface component, and is in excellent agreement with CERES in the SH. Under different symmetry criteria (0.1 W m⁻², 0.2 W m⁻², 1 W m⁻² and uncertainties of different datasets), the applicability of different datasets to hemispheric symmetry of RSRPA studies varies. CERES can achieve hemispheric symmetry at a 15-year average with the 0.1 W m⁻² criterion, and when the criterion is extended to 0.2 W m⁻² and 1 W m⁻², the years of applicability are advanced to 9-year and every year. AVHRR correlates best with CERES for the time series of hemispheric differences of total reflected radiation. AVHRR can achieve hemispheric symmetry within its uncertainty of the 14-year time scale, the multi-year mean is closest, and the hemispheric symmetry of the PA can be studied within its uncertainty on 14-year timescale. ISCCP achieves hemispheric symmetry within its uncertainty on a 5-year scale, but shows increasing hemispheric asymmetry over time. Both reanalysis datasets are far from the criterion of hemispheric symmetry of RSR. All datasets fail to capture the changes in multi-year averaged hemispheric differences of clear-sky atmospheric components as the record length increases, possibly due to a lack of data assimilation for anthropogenic aerosol emissions and large-scale biomass burning activities. In addition, all datasets struggle in capturing hemispheric and regional trends in RSR and its components. However, AVHRR does not adequately capture the hemispheric differences of individual components. ERA5 and ISCCP simulate hemispheric differences of total reflected radiation with about the same performance, while ERA5 itself is more stable. ERA5 and ISCCP simulate hemispheric differences of total reflected radiation with about the same performance, while ERA5 itself

~~is more stable. If one only wants to study cloud component, consider using ISCCP.~~

Based on long-term satellite observations, ~~our~~^{this} study and previous research have confirmed a clear decreasing trend in solar radiation reflected back into space in both hemispheres over the past two decades (Loeb et al., 2020; Stephens et al., 2022). ~~To further investigate the inter-hemispheric differences in Earth's energy balance, we also calculate the trends of outgoing longwaveLW radiation and net radiation at the TOA (figure not shown). A significant increasing trend of longwaveLW radiation emitted to space is found in the NH ($0.324 \text{ W m}^{-2} (10a)^{-1}$), while no significant trend is observed in the SH. Loeb et al. (2021b) noted that the increase in outgoing longwaveLW radiation is primarily due to the increasing global surface temperature and changes in clouds, although it is partly compensated by the increase in water vapor and trace gases. However, the overall increase in outgoing longwaveLW radiation does not outweighoffset the decrease in reflected shortwave radiationRSR, resulting in a positive trend in the net radiative flux in both hemispheres (indicating that the Earth is absorbing more energy) (Raghuraman et al., 2021). This positive trend in the Earth's energy imbalance (EEI) will exacerbate global warming, sea-level rise, increased internal heating of the oceans, and melting of snow and sea ice (IPCC, 2013; Von Schuckmann et al., 2016; Loeb et al., 2021b). Indeed, a recent study based on long-term homogenized radiosonde data indicated that the atmosphere has become increasingly more unstable in the NH during the period 1979-2020 (Chen and Dai, 2023). This trend is particularly significant as the increase in net solar energy absorption by the Earth outweighs the increase in outgoing thermal infrared radiation. Consequently, it leads to a rise in global average temperature, exacerbating the Earth's energy imbalance, global warming, sea level rise, changes in the climate system, and the melting of glaciers and permafrost (Loeb et al., 2021b).~~ Given the profound impact of these changes on the climate system, it is crucial to pay closer attention to the future evolution of PA and its symmetry. Although climate models persistently exhibit biases in simulating the ~~meanaverage~~ state of albedo symmetry from CMIP3 to CMIP6 (Crueger et al., 2023), they remain a powerful tool for generating hypotheses about the unexplained observed ~~RSR~~^{albedo} symmetry (Rugenstein and Hakuba, 2023) and projecting future evolutions and potential influencing mechanisms. For example, Rugenstein and Hakuba (2023) examined the response of modeled surface temperature and ~~PA-RSR~~ to CO₂ and found an increasing difference in surface warming between the two hemispheres under stronger carbon dioxide forcing and weaker aerosol forcing. They also proposed that the warmer hemisphere will become darker, suggesting a potential

asymmetry in albedo in the coming decades. On the other hand, Diamond et al. (2022) focused on changes in clear-sky hemispheric asymmetry under different emission scenarios simulated by their model. Their results indicated a significant shift in clear-sky albedo asymmetry throughout this century under both high and low emission scenarios, primarily driven by anthropogenic aerosol emissions and cryosphere changes. Furthermore, Jönsson and Bender (2023) investigated the evolution of hemispheric albedo differences following a sudden quadrupling of CO₂ concentration using CMIP6 coupled model simulations. They found that the initial albedo reduction in the NH may be partly compensated by a reduction in extratropical cloudiness in the SH on a much longer timescale which can be referred to as a mechanism of trans-hemispheric communication. They also highlighted that if [RSRPA](#) maintains hemispheric symmetry, compensating for cloud variations will have uncertain but significant effects on Earth's energy balance and hydrologic cycle. However, whether the hemispheric symmetry of [RSRPA](#) can be sustained indefinitely remains an open question. Therefore, it is essential to focus on investigating additional potential mechanisms of hemispheric [RSRPA](#) symmetry and future projections using model ensembles, along with observational constraints.

Data availability. The CERES_EBAF_Ed4.2 and CERES_SSF1deg products ~~is are~~ publicly available through the NASA Langley Research Center CERES ordering tool at <https://ceres.larc.nasa.gov/data/>. The ESA Cloud-cci version 3 products, AVHRR-PMv3 for this research are included in the paper: Stengel et al. (2020), or obtained through https://public.satproj.klima.dwd.de/data/ESA_Cloud_CCI/CLD_PRODUCTS/v3.0/L3C/. The ISCCP-FH data are available from the following website: <https://isccp.giss.nasa.gov/pub/flux-fh/>. The MERRA-2 datasets used in this study ~~is are~~ available from the following websites: <https://doi.org/10.5067/OU3HJDS973O0>, ~~https://doi.org/10.5067/OU3HJDS973O0~~ and <https://doi.org/10.5067/FH9A0MLJPC7N>. The ERA5 monthly averaged data on single levels from 1940 to present are available from Climate Data Store (CDS) of <https://cds.climate.copernicus.eu/cdsapp#!/dataset/reanalysis-era5-single-levels-monthly-means?tab=overview>.

Author contributions. RL and BJ organized the paper and performed related analysis. RL drew article

1495 graph and prepared the manuscript. BJ and JL conceptualized the paper and revised the whole manuscript.
| DW ~~and~~, LZ, YW and YW ~~–~~ modified the paper and provided suggestions for this study. All authors
contributed to the discussion of the results and reviewed the manuscript.

Competing interests. The contact author has declared that none of the authors has any competing
1500 interests.

Disclaimer. Publisher's note: Copernicus Publications remains neutral with regard to jurisdictional
claims in published maps and institutional affiliations.

1505 **Acknowledgements.** We would like to thank the CERES, CLOUD_CCI AVHRR, ISCCP, MERRA-2,
and ERA5 science teams for providing excellent and accessible data products that made this study
possible. We would like to acknowledge the assistance of ChatGPT in proofreading and polishing the
language of this manuscript. ChatGPT, an AI language model developed by OpenAI, helped refine the
clarity and fluency of the text. We are grateful for its contribution in improving the quality of our work.

1510 **Financial support.** This research was jointly supported by the National Science Fund for Excellent
Young Scholars (42022037), the Major Program of the National Natural Science Foundation of China
(42090030), the National Natural Science Foundation of China (42305072), and the China Postdoctoral
Science Foundation (2023M731454).

1515

References

Andersen, H., Cermak, J., Zipfel, L., and Myers, T. A.: Attribution of observed recent decrease in low
clouds over the Northeastern Pacific to cloud-controlling factors, *Geophysical Research Letters*, 49,
e2021GL096498, <https://doi.org/10.1029/2021GL096498>, 2022.

1520 ~~Avery, M. A., Davis, S. M., Rosenlof, K. H., Ye, H., and Dessler, A. E.: Large anomalies in lower
stratospheric water vapour and ice during the 2015–2016 El Niño, *Nature Geoscience*, 10, 405–409,
<https://doi.org/10.1038/NGEO2961>, 2017.~~

- Bender, F. A.-M., Rodhe, H., Charlson, R. J., Ekman, A. M., and Loeb, N.: 22 views of the global albedo—comparison between 20 GCMs and two satellites, *Tellus A: Dynamic Meteorology and Oceanography*, 58, 320-330, <https://doi.org/10.1111/j.1600-0870.2006.00181.x>, 2006.
- 1525
- Bhatti, Y. A., Revell, L. E., and McDonald, A. J.: Influences of Antarctic ozone depletion on southern ocean aerosols, *Journal of Geophysical Research: Atmospheres*, 127, e2022JD037199, <https://doi.org/10.1029/2022JD037199>, 2022.
- 1530 [Blanco, J. E., Caballero, R., Datseris, G., Stevens, B., Bony, S., Hadas, O., and Kaspi, Y.: A cloud-controlling factor perspective on the hemispheric asymmetry of extratropical cloud albedo, *Journal of climate*, 36, 1793-1804, <https://doi.org/10.1175/JCLI-D-22-0410.1>, 2023.](#)
- [Betts, R. A.: Offset of the potential carbon sink from boreal forestation by decreases in surface albedo, *Nature*, 408, 187-190, <https://doi.org/10.1038/35041545>, 2000.](#)
- 1535 Boudala, F. S. and Milbrandt, J. A.: Evaluations of the Climatologies of Three Latest Cloud Satellite Products Based on Passive Sensors (ISCCP-H, Two CERES) against the CALIPSO-GOCCP, *Remote Sensing*, 13, 5150, <https://doi.org/10.3390/rs13245150>, 2021.
- 1540 [Buchard, V., Randles, C., Da Silva, A., Darmenov, A., Colarco, P., Govindaraju, R., Ferrare, R., Hair, J., Beyersdorf, A., and Ziemba, L.: The MERRA-2 aerosol reanalysis, 1980 onward. Part II: Evaluation and case studies, *Journal of Climate*, 30, 6851-6872, <https://doi.org/10.1175/JCLI-D-16-0613.1>, 2017.](#)
- Budyko, M. I.: The effect of solar radiation variations on the climate of the Earth, *tellus*, 21, 611-619, <https://doi.org/10.3402/tellusa.v21i5.10109>, 1969.
- 1545
- Cao, Y., Liang, S., He, T., and Chen, X.: Evaluation of four reanalysis surface albedo data sets in Arctic using a satellite product, *IEEE Geoscience and Remote Sensing Letters*, 13, 384-388, <https://doi.org/10.1109/LGRS.2016.2515159>, 2016.
- 1550 [Chen, F., Wang, D., Zhang, Y., Zhou, Y., and Chen, C.: Intercomparisons and Evaluations of Satellite-Derived Arctic Sea Ice Thickness Products, *Remote Sensing*, 16, 508, <https://doi.org/10.3390/rs16030508>, 2024.](#)

Chen, J. and Dai, A.: The atmosphere has become increasingly unstable during 1979–2020 over the Northern Hemisphere, *Geophysical Research Letters*, 50, e2023GL106125, <https://doi.org/10.1029/2023GL106125>, 2023.

1555 [Cole-Dai, J.: Volcanoes and climate, *Wiley Interdisciplinary Reviews: Climate Change*, 1, 824-839, <https://doi.org/10.1002/wcc.76>, 2010.](#)

Crueger, T., Schmidt, H., and Stevens, B.: Hemispheric albedo asymmetries across three phases of CMIP, *Journal of Climate*, 1-34, <https://doi.org/10.1175/JCLI-D-22-0923.1>, 2023.

1560 [Cui, T., Qing, S., Wei, T., Mu, B., Xiao, Y., Chen, Y., Bao, Y., and Zhang, J.: Decade-low aerosol levels over the Bohai and Yellow Seas amid the COVID-19 lockdown, *International Journal of Applied Earth Observation and Geoinformation*, 112, 102905, <https://doi.org/10.1016/j.jag.2022.102905>, 2022.](#)

1565 [Datseris, G. and Stevens, B.: Earth's albedo and its symmetry, *AGU Advances*, 2, e2021AV000440, <https://doi.org/10.1029/2021AV000440>, 2021.](#) [Deng, C., Li, J., Li, J., Li, R., Zhang, W., Zhao, Y., Zhao, Y., and Jian, B.: Long term changes in the diurnal cycle of total cloud cover over the Tibetan Plateau, *Atmospheric Research*, 106992, <https://doi.org/10.1016/j.atmosres.2023.106992>, 2023.](#)

1570 Devasthale, A. and Karlsson, K.-G.: Decadal Stability and Trends in the Global Cloud Amount and Cloud Top Temperature in the Satellite-Based Climate Data Records, *Remote Sensing*, 15, 3819, <https://doi.org/10.3390/rs15153819>, 2023.

1575 [Diamond, M. S., Gristey, J. J., Kay, J. E., and Feingold, G.: Anthropogenic aerosol and cryosphere changes drive Earth's strong but transient clear-sky hemispheric albedo asymmetry, *Commun Earth Environ*, 3, 206, <https://doi.org/10.1038/s43247-022-00546-y>, 2022.](#)

Dolinar, E. K., Dong, X., and Xi, B.: Evaluation and intercomparison of clouds, precipitation, and radiation budgets in recent reanalyses using satellite-surface observations, *Climate Dynamics*, 46, 2123-2144, <https://doi.org/10.1007/s00382-015-2693-z>, 2016.

1580 [Engström, A., Bender, F. A. M., Wood, R., and Charlson, R. J.: Evaluation of Hemispheric Asymmetries in Marine Cloud Radiative Properties, *Journal of Climate*, 30, 4131-4147,](#)

<https://doi.org/10.1175/jcli-d-16-0263.1>, 2017.

[Evan, A. T., Heidinger, A. K., and Vimont, D. J.: Arguments against a physical long-term trend in global ISCCP cloud amounts, *Geophysical Research Letters*, 34, <https://doi.org/10.1029/2006GL028083>, 2007.](#)

1585 [Fan, H., Yang, X., Zhao, C., Yang, Y., and Shen, Z.: Spatiotemporal variation characteristics of global fires and their emissions, *Atmospheric Chemistry and Physics*, 23, 7781-7798, <https://doi.org/10.5194/acp-23-7781-2023>, 2023.](#)

Fu, Q., Cribb, M., Barker, H., Krueger, S., and Grossman, A.: Cloud geometry effects on atmospheric solar absorption, *Journal of the atmospheric sciences*, 57, 1156-1168, [https://doi.org/10.1175/1520-0469\(2000\)057<1156:CGEOAS>2.0.CO;2](https://doi.org/10.1175/1520-0469(2000)057<1156:CGEOAS>2.0.CO;2), 2000.

1590

Gelaro, R., McCarty, W., Suárez, M. J., Todling, R., Molod, A., Takacs, L., Randles, C. A., Darmenov, A., Bosilovich, M. G., and Reichle, R.: The modern-era retrospective analysis for research and applications, version 2 (MERRA-2), *Journal of climate*, 30, 5419-5454, <https://doi.org/10.1175/JCLI-D-16-0758.1>, 2017.

1595 [George, D. and Bjorn, S.: Earth's Albedo and Its Symmetry, *AGU Advances*, 2, <https://doi.org/10.1029/2021AV000440>, 2021.](#)

[Gruber, A.: Fluctuations in the position of the ITCZ in the Atlantic and Pacific Oceans, *Journal of Atmospheric Sciences*, 29, 193-197, \[https://doi.org/10.1175/1520-0469\\(1972\\)029<0193:FITPOT>2.0.CO;2\]\(https://doi.org/10.1175/1520-0469\(1972\)029<0193:FITPOT>2.0.CO;2\), 1972.](#)

1600 [Gui, K., Che, H., Zheng, Y., Zhao, H., Yao, W., Li, L., Zhang, L., Wang, H., Wang, Y., and Zhang, X.: Three-dimensional climatology, trends, and meteorological drivers of global and regional tropospheric type-dependent aerosols: insights from 13 years \(2007–2019\) of CALIOP observations, *Atmospheric Chemistry and Physics*, 21, 15309-15336, <https://doi.org/10.5194/acp-21-15309-2021>, 2021.](#)

1605 [Hadas, O., Datsieris, G., Blanco, J., Bony, S., Caballero, R., Stevens, B., and Kaspi, Y.: The role of baroclinic activity in controlling Earth's albedo in the present and future climates, *Proceedings of the National Academy of Sciences*, 120, e2208778120, <https://doi.org/10.1073/pnas.2208778120>, 2023.](#)

[He, Y., Wang, K., and Feng, F.: Improvement of ERA5 over ERA-Interim in simulating surface incident](#)

- 1610 [solar radiation throughout China, Journal of Climate, 34, 3853-3867, https://doi.org/10.1175/JCLI-D-20-0300.1, 2021.](https://doi.org/10.1175/JCLI-D-20-0300.1)
- Hersbach, H., Bell, B., Berrisford, P., Hirahara, S., Horányi, A., Muñoz-Sabater, J., Nicolas, J., Peubey, C., Radu, R., and Schepers, D.: The ERA5 global reanalysis, Quarterly Journal of the Royal Meteorological Society, 146, 1999-2049, <https://doi.org/10.1002/qj.3803>, 2020.
- 1615 Hinkelman, L. M.: The global radiative energy budget in MERRA and MERRA-2: Evaluation with respect to CERES EBAF data, Journal of Climate, 32, 1973-1994, <https://doi.org/10.1175/JCLI-D-18-0445.1>, 2019.
- [Hirsch, E. and Koren, I.: Record-breaking aerosol levels explained by smoke injection into the stratosphere, Science, 371, 1269-1274, https://doi.org/10.1126/science.abe1415, 2021.](https://doi.org/10.1126/science.abe1415)
- 1620 Hollmann, R., Merchant, C. J., Saunders, R., Downy, C., Buchwitz, M., Cazenave, A., Chuvieco, E., Defourny, P., de Leeuw, G., and Forsberg, R.: The ESA climate change initiative: Satellite data records for essential climate variables, Bulletin of the American Meteorological Society, 94, 1541-1552, <https://doi.org/10.1175/BAMS-D-11-00254.1>, 2013.
- [Hu, Y. and Stamnes, K.: An accurate parameterization of the radiative properties of water clouds suitable for use in climate models, Journal of climate, 6, 728-742, https://doi.org/10.1175/1520-0442\(1993\)006<0728:AAPOTR>2.0.CO;2, 1993.](https://doi.org/10.1175/1520-0442(1993)006<0728:AAPOTR>2.0.CO;2)
- 1625 ~~[Hu, Y. and Stamnes, K.: An accurate parameterization of the radiative properties of water clouds suitable for use in climate models, Journal of climate, 6, 728-742, https://doi.org/10.1175/1520-0442\(1993\)006<0728:AAPOTR>2.0.CO;2, 1993.](https://doi.org/10.1175/1520-0442(1993)006<0728:AAPOTR>2.0.CO;2)~~
- Hu, Y., Li, D., and Liu, J.: Abrupt seasonal variation of the ITCZ and the Hadley circulation, Geophysical research letters, 34, <https://doi.org/10.1029/2007GL030950>, 2007, 2007.
- [Hu, Z. Z., Kumar, A., Huang, B., Xue, Y., Wang, W., and Jha, B.: Persistent atmospheric and oceanic anomalies in the North Atlantic from summer 2009 to summer 2010, Journal of Climate, 24, 5812-5830, https://doi.org/10.1175/2011JCLI4213.1, 2011.](https://doi.org/10.1175/2011JCLI4213.1)
- 1630 ~~[Hu, Z. Z., Kumar, A., Huang, B., Xue, Y., Wang, W., and Jha, B.: Persistent atmospheric and oceanic anomalies in the North Atlantic from summer 2009 to summer 2010, Journal of Climate, 24, 5812-5830, https://doi.org/10.1175/2011JCLI4213.1, 2011.](https://doi.org/10.1175/2011JCLI4213.1)~~
- Hu, Z., Chen, X., Zhou, Q., Chen, D., and Li, J.: DISO: A rethink of Taylor diagram, International Journal of Climatology, 39, 2825-2832, <https://doi.org/10.1002/joc.5972>, 2019.
- Hu, Z., Chen, D., Chen, X., Zhou, Q., Peng, Y., Li, J., and Sang, Y.: CCHZ-DISO: A Timely New
- 1635 Assessment System for Data Quality or Model Performance From Da Dao Zhi Jian, Geophysical Research Letters, 49, e2022GL100681, <https://doi.org/10.1029/2022GL100681>, 2022.
- [Huang, B., L'Heureux, M., Hu, Z. Z., and Zhang, H. M.: Ranking the strongest ENSO events while incorporating SST uncertainty, Geophysical Research Letters, 43, 9165-9172,](https://doi.org/10.1029/2022GL100681)

<https://doi.org/10.1002/2016GL070888>, 2016.

1640 [Huang, J. p., Guan, X. d., and Ji, F.: Enhanced cold season warming in semi-arid regions, Atmospheric Chemistry and Physics, 12, 5391–5398, <https://doi.org/10.5194/acp-12-5391-2012>, 2012.](#)

IPCC, A.: Climate change 2013: the physical science basis, Contribution of working group I to the fifth assessment report of the intergovernmental panel on climate change, 1535, 2013.

1645 [Jenkins, M. T., Dai, A., and Deser, C.: Seasonal Variations and Spatial Patterns of Arctic Cloud Changes in Association with Sea Ice Loss during 1950–2019 in ERA5, Journal of Climate, 37, 735–754, <https://doi.org/10.1175/JCLI-D-23-0117.1>, 2024.](#)

[Jia, A., Wang, D., Liang, S., Peng, J., and Yu, Y.: Global daily actual and snow-free blue-sky land surface albedo climatology from 20-year MODIS products, Journal of Geophysical Research: Atmospheres, 127, e2021JD035987, <https://doi.org/10.1029/2021JD035987>, 2022.](#)

1650 [Jia, A., Wang, D., Liang, S., Peng, J., and Yu, Y.: Improved cloudy-sky snow albedo estimates using passive microwave and VIIRS data, ISPRS Journal of Photogrammetry and Remote Sensing, 196, 340–355, <https://doi.org/10.1016/j.isprsjprs.2023.01.004>, 2023.](#)

1655 [Jian, B., Li, J., Wang, G., He, Y., Han, Y., Zhang, M., and Huang, J.: The Impacts of Atmospheric and Surface Parameters on Long-Term Variations in the Planetary Albedo, Journal of Climate, 31, 8705–8718, <https://doi.org/10.1175/jcli-d-17-0848.1>, 2018.](#)

Jiang, H., Yang, Y., Bai, Y., and Wang, H.: Evaluation of the total, direct, and diffuse solar radiations from the ERA5 reanalysis data in China, IEEE Geoscience and Remote Sensing Letters, 17, 47–51, <https://doi.org/10.1109/LGRS.2019.2916410>, 2019.

1660 [Jiang, H., Yang, Y., Wang, H., Bai, Y., and Bai, Y.: Surface diffuse solar radiation determined by reanalysis and satellite over East Asia: evaluation and comparison, Remote sensing, 12, 1387, <https://doi.org/10.3390/rs12091387>, 2020.](#)

1665 [Jiao, P., Wang, J., Chen, X., Ruan, J., Ye, X., and Alavi, A. H.: Next-generation remote sensing and prediction of sand and dust storms: State-of-the-art and future trends, International Journal of Remote Sensing, 42, 5277–5316, <https://doi.org/10.1080/01431161.2021.1912433>, 2021.](#) [Jiménez-Muñoz, J.-C., Mattar, C., Barichivich, J., Santamaría-Artigas, A., Takahashi, K., Malhi, Y., Sobrino, J. A., and Schrier, G. v. d.: Record-breaking warming and extreme drought in the Amazon rainforest](#)

during the course of El Niño 2015–2016, *Scientific reports*, 6, 33130,
<https://doi.org/10.1038/srep33130>, 2016.

1670 Johnson, G. C., Lyman, J. M., and Loeb, N. G.: Improving estimates of Earth's energy imbalance, *Nature Climate Change*, 6, 639-640, <https://doi.org/10.1038/nclimate3043>, 2016.

Jönsson, A. and Bender, F. A.-M.: Persistence and variability of Earth's interhemispheric albedo symmetry in 19 years of CERES EBAF observations, *Journal of Climate*, 35, 249-268, <https://doi.org/10.1175/JCLI-D-20-0970.1>, 2022.

1675 Jönsson, A. R. and Bender, F. A.-M.: The implications of maintaining Earth's hemispheric albedo symmetry for shortwave radiative feedbacks, *Earth System Dynamics*, 14, 345-365, <https://doi.org/10.5194/esd-14-345-2023>, 2023.

Kalmár, T., Pieczka, I., and Pongrácz, R.: A sensitivity analysis of the different setups of the RegCM4. 5 model for the Carpathian region, *International Journal of Climatology*, 41, E1180-E1201, <https://doi.org/10.1002/joc.6761>, 2021.

Kato, S., Loeb, N. G., Rose, F. G., Doelling, D. R., Rutan, D. A., Caldwell, T. E., Yu, L., and Weller, R. A.: Surface irradiances consistent with CERES-derived top-of-atmosphere shortwave and longwave irradiances, *Journal of Climate*, 26, 2719-2740, <https://doi.org/10.1175/JCLI-D-12-00436.1>, 2013.

1685 Kato, S., Rose, F. G., Rutan, D. A., Thorsen, T. J., Loeb, N. G., Doelling, D. R., Huang, X., Smith, W. L., Su, W., and Ham, S.-H.: Surface irradiances of edition 4.0 clouds and the earth's radiant energy system (CERES) energy balanced and filled (EBAF) data product, *Journal of Climate*, 31, 4501-4527, <https://doi.org/10.1175/JCLI-D-17-0523.1>, 2018.

1690 [Kuma, P., McDonald, A. J., Morgenstern, O., Alexander, S. P., Cassano, J. J., Garrett, S., Halla, J., Hartery, S., Harvey, M. J., and Parsons, S.: Evaluation of Southern Ocean cloud in the HadGEM3 general circulation model and MERRA-2 reanalysis using ship-based observations, *Atmospheric Chemistry and Physics*, 20, 6607-6630, <https://doi.org/10.5194/acp-20-6607-2020>, 2020.](#)

[Khaykin, S., Legras, B., Bucci, S., Sellitto, P., Isaksen, L., Tencé, F., Bekki, S., Bourassa, A., Rieger, L., and Zawada, D.: The 2019/20 Australian wildfires generated a persistent smoke charged vortex rising up to 35 km altitude, *Communications Earth & Environment*, 1, 22, <https://doi.org/10.1038/s43247-020-00022-5>, 2020.](#)

1695 [Kopplitz, S. N., Mickle, L. J., Marlier, M. E., Buonocore, J. J., Kim, P. S., Liu, T., Sulprizio, M. P.,](#)

- DeFries, R. S., Jacob, D. J., and Schwartz, J.: Public health impacts of the severe haze in Equatorial Asia in September–October 2015: demonstration of a new framework for informing fire management strategies to reduce downwind smoke exposure, *Environmental Research Letters*, 11, 094023, <https://doi.org/10.1088/1748-9326/11/9/094023>, 2016.
- 1700
- Letu, H., Nagao, T. M., Nakajima, T. Y., Riedi, J., Ishimoto, H., Baran, A. J., Shang, H., Sekiguchi, M., and Kikuchi, M.: Ice cloud properties from Himawari 8/AHI next-generation geostationary satellite: Capability of the AHI to monitor the DC cloud generation process, *IEEE Transactions on Geoscience and Remote Sensing*, 57, 3229–3239, <https://doi.org/10.1109/TGRS.2018.2882803>, 2018.
- 1705
- Letu, H., Ma, R., Nakajima, T. Y., Shi, C., Hashimoto, M., Nagao, T. M., Baran, A. J., Nakajima, T., Xu, J., and Wang, T.: Surface Solar Radiation Compositions Observed from Himawari 8/9 and Fengyun-4 Series, *Bulletin of the American Meteorological Society*, 104, E1772–E1789, <https://doi.org/10.1175/BAMS-D-22-0154.1>, 2023.
- 1710
- Li, J., Mao, J., and Wang, F.: Comparative study of five current reanalyses in characterizing total cloud fraction and top-of-the-atmosphere cloud radiative effects over the Asian monsoon region, *International Journal of Climatology*, 37, 5047–5067, <https://doi.org/10.1002/joc.5143>, 2017.
- Li, M., Shen, F., and Sun, X.: 2019–2020 Australian bushfire air particulate pollution and impact on the South Pacific Ocean, *Scientific Reports*, 11, 12288, <https://doi.org/10.1038/s41598-021-91547-y>, 2021.
- 1715
- Li, R., Mei, X., Chen, L., Wang, L., Wang, Z., and Jing, Y.: Long-term (2005–2017) view of atmospheric pollutants in Central China using multiple satellite observations, *Remote Sensing*, 12, 1041, <https://doi.org/10.3390/rs12061041>, 2020.
- Li, J., Lv, Q., Jian, B., Zhang, M., Zhao, C., Fu, Q., Kawamoto, K., and Zhang, H.: The impact of atmospheric stability and wind shear on vertical cloud overlap over the Tibetan Plateau, *Atmospheric Chemistry and Physics*, 18, 7329–7343, <https://doi.org/10.5194/acp-18-7329-2018>, 2018.
- 1720
- Li, M., Letu, H., Peng, Y., Ishimoto, H., Lin, Y., Nakajima, T. Y., Baran, A. J., Guo, Z., Lei, Y., and Shi, J.: Investigation of ice cloud modeling capabilities for the irregularly shaped Voronoi ice scattering models in climate simulations, *Atmospheric Chemistry and Physics*, 22, 4809–4825,
- 1725

<https://doi.org/10.5194/acp-22-4809-2022>, 2022.

Li, Z. X. and Le Treut, H.: Cloud radiation feedbacks in a general circulation model and their dependence on cloud modelling assumptions, *Climate Dynamics*, 7, 133–139, <https://doi.org/10.1007/BF00211155>, 1992.

1730 Li, Z., Yang, X., and Tang, H.: Evaluation of the hourly ERA5 radiation product and its relationship with aerosols over China, *Atmospheric Research*, 294, 106941, <https://doi.org/10.1016/j.atmosres.2023.106941>, 2023.

1735 Lim, E. P. and Hendon, H. H.: Causes and predictability of the negative Indian Ocean Dipole and its impact on La Niña during 2016, *Scientific reports*, 7, 1–11, <https://doi.org/10.1038/s41598-017-12674-z>, 2017.

Lim, E. P., Hendon, H. H., Arblaster, J. M., Chung, C., Moise, A. F., Hope, P., Young, G., and Zhao, M.: Interaction of the recent 50 year SST trend and La Niña 2010: amplification of the Southern Annular Mode and Australian springtime rainfall, *Climate dynamics*, 47, 2273–2291, <https://doi.org/10.1007/s00382-015-2963-9>, 2016.

1740 Lim, Y. K., Kovach, R. M., Pawson, S., and Vernieres, G.: The 2015/16 El Niño event in context of the MERRA-2 reanalysis: A comparison of the tropical Pacific with 1982/83 and 1997/98, *Journal of climate*, 30, 4819–4842, <https://doi.org/10.1175/JCLI-D-16-0800.1>, 2017.

Lim, Y.-K., Wu, D. L., Kim, K.-M., and Lee, J. N.: An Investigation on Seasonal and Diurnal Cycles of TOA Shortwave Radiations from DSCOVR/EPIC, CERES, MERRA-2, and ERA5, *Remote Sensing*, 13, 4595, <https://doi.org/10.3390/rs13224595>, 2021.

Loeb, N. G., Su, W., Bellouin, N., and Ming, Y.: Changes in clear-sky shortwave aerosol direct radiative effects since 2002, *Journal of Geophysical Research: Atmospheres*, 126, e2020JD034090, <https://doi.org/10.1029/2020JD034090>, 2021a.

1750 Loeb, N. G., Wielicki, B. A., Rose, F. G., and Doelling, D. R.: Variability in global top-of-atmosphere shortwave radiation between 2000 and 2005, *Geophysical research letters*, 34, <https://doi.org/10.1029/2006GL028196>, 2007.

Loeb, N. G., Thorsen, T. J., Norris, J. R., Wang, H., and Su, W.: Changes in Earth's energy budget during and after the “pause” in global warming: An observational perspective, *Climate*, 6, 62, <https://doi.org/10.3390/cli6030062>, 2018a.

- 1755 Loeb, N. G., Johnson, G. C., Thorsen, T. J., Lyman, J. M., Rose, F. G., and Kato, S.: Satellite and ocean data reveal marked increase in Earth's heating rate, *Geophysical Research Letters*, 48, e2021GL093047, <https://doi.org/10.1029/2021GL093047>, 2021b.
- Loeb, N. G., Priestley, K. J., Kratz, D. P., Geier, E. B., Green, R. N., Wielicki, B. A., Hinton, P. O. R., and Nolan, S. K.: Determination of unfiltered radiances from the Clouds and the Earth's Radiant Energy System instrument, *Journal of Applied Meteorology*, 40, 822-835, [https://doi.org/10.1175/1520-0450\(2001\)040<0822:DOURFT>2.0.CO;2](https://doi.org/10.1175/1520-0450(2001)040<0822:DOURFT>2.0.CO;2), 2001.
- 1760 Loeb, N. G., Wielicki, B. A., Doelling, D. R., Smith, G. L., Keyes, D. F., Kato, S., Manalo-Smith, N., and Wong, T.: Toward optimal closure of the Earth's top-of-atmosphere radiation budget, *Journal of Climate*, 22, 748-766, <https://doi.org/10.1175/2008JCLI2637.1>, 2009.
- 1765 Loeb, N. G., Mayer, M., Kato, S., Fasullo, J. T., Zuo, H., Senan, R., Lyman, J. M., Johnson, G. C., and Balmaseda, M.: Evaluating twenty-year trends in Earth's energy flows from observations and reanalyses, *Journal of Geophysical Research: Atmospheres*, 127, e2022JD036686, <https://doi.org/10.1029/2022JD036686>, 2022.
- Loeb, N. G., Doelling, D. R., Wang, H., Su, W., Nguyen, C., Corbett, J. G., Liang, L., Mitrescu, C., Rose, F. G., and Kato, S.: Clouds and the earth's radiant energy system (CERES) energy balanced and filled (EBAF) top-of-atmosphere (TOA) edition-4.0 data product, *Journal of Climate*, 31, 895-918, <https://doi.org/10.1175/JCLI-D-17-0208.1>, 2018b.
- 1770 Loeb, N. G., Wang, H., Allan, R. P., Andrews, T., Armour, K., Cole, J. N., Dufresne, J. L., Forster, P., Gettelman, A., and Guo, H.: New generation of climate models track recent unprecedented changes in Earth's radiation budget observed by CERES, *Geophysical Research Letters*, 47, e2019GL086705, <https://doi.org/10.1029/2019GL086705>, 2020.
- 1775
- Marchand, R., Ackerman, T., Smyth, M., and Rossow, W. B.: A review of cloud top height and optical depth histograms from MISR, ISCCP, and MODIS, *Journal of Geophysical Research: Atmospheres*, 115, <https://doi.org/10.1029/2009JD013422>, 2010.
- 1780
- Miinalainen, T., Kokkola, H., Lehtinen, K. E., and Kühn, T.: Comparing the radiative forcings of the anthropogenic aerosol emissions from Chile and Mexico, *Journal of Geophysical Research: Atmospheres*, 126, e2020JD033364, <https://doi.org/10.1080/16000889.2020.1821512>, 2021.

1785 Mika, R., Yu, K. A., Antti, L., Kalle, N., Otto, H., Kimmo, R., Timo, V., and Ari, L.: The Arctic has warmed nearly four times faster than the globe since 1979, *Communications Earth & Environment*, 3, <https://doi.org/10.1038/s43247-022-00498-3>, 2022.

[Minnis, P., Harrison, E. F., Stowe, L. L., Gibson, G., Denn, F. M., Doelling, D., and Smith Jr, W.: Radiative climate forcing by the Mount Pinatubo eruption, *Science*, 259, 1411-1415, <https://doi.org/10.1126/science.259.5100.1411>, 1993.](#)

1790 [Minnis, P., Sun Mack, S., Chen, Y., Chang, F. L., Yost, C. R., Smith, W. L., Heck, P. W., Arduini, R. F., Bedka, S. T., and Yi, Y.: CERES MODIS cloud product retrievals for edition 4 — Part I: Algorithm changes, *IEEE Transactions on Geoscience and Remote Sensing*, 59, 2744-2780, <https://doi.org/10.1109/TGRS.2020.3008866>, 2020.](#)

1795 Noël, B., Van De Berg, W., Van Meijgaard, E., Kuipers Munneke, P., Van De Wal, R., and Van Den Broeke, M.: Evaluation of the updated regional climate model RACMO2. 3: summer snowfall impact on the Greenland Ice Sheet, *The Cryosphere*, 9, 1831-1844, <https://doi.org/10.5194/tc-9-1831-2015>, 2015.

[Norris, J. R. and Evan, A. T.: Empirical removal of artifacts from the ISCCP and PATMOS-x satellite cloud records, *Journal of Atmospheric and Oceanic Technology*, 32, 691-702, <https://doi.org/10.1175/JTECH-D-14-00058.1>, 2015.](#)

1800 North, G. R., Cahalan, R. F., and Coakley Jr, J. A.: Energy balance climate models, *Reviews of Geophysics*, 19, 91-121, <https://doi.org/10.1029/RG019i001p00091>, 1981.

Pang, G., Chen, D., Wang, X., and Lai, H.-W.: Spatiotemporal variations of land surface albedo and associated influencing factors on the Tibetan Plateau, *Science of the Total Environment*, 804, 150100, <https://doi.org/10.1016/j.scitotenv.2021.150100>, 2022.

1805 [Pu, W., Cui, J., Wu, D., Shi, T., Chen, Y., Xing, Y., Zhou, Y., and Wang, X.: Unprecedented snow darkening and melting in New Zealand due to 2019–2020 Australian wildfires, *Fundamental Research*, 1, 224-231, \[10.1016/j.fmre.2021.04.001\]\(https://doi.org/10.1016/j.fmre.2021.04.001\), 2021.](#)

[Qu, X. and Hall, A.: Surface contribution to planetary albedo variability in cryosphere regions, *Journal of Climate*, 18, 5239-5252, <https://doi.org/10.1175/JCLI3555.1>, 2005.](#)

1810 Quaas, J., Jia, H., Smith, C., Albright, A. L., Aas, W., Bellouin, N., Boucher, O., Doutriaux-Boucher, M., Forster, P. M., and Grosvenor, D.: Robust evidence for reversal of the trend in aerosol effective

climate forcing, *Atmospheric Chemistry and Physics*, 22, 12221-12239, <https://doi.org/10.5194/acp-22-12221-2022>, 2022.

1815 Raghuraman, S. P., Paynter, D., and Ramaswamy, V.: Anthropogenic forcing and response yield observed positive trend in Earth's energy imbalance, *Nature communications*, 12, 4577, <https://doi.org/10.1038/s41467-021-24544-4>, 2021.

1820 ~~Riihela, A., Bright, R. M., and Anttila, K.: Recent strengthening of snow and ice albedo feedback driven by Antarctic sea ice loss, *Nature Geoscience*, 14, 832-836, <https://doi.org/10.1038/s41561-021-00841-x>, 2021.~~

Rugenstein, M. and Hakuba, M.: Connecting hemispheric asymmetries of planetary albedo and surface temperature, *Geophysical Research Letters*, 50, e2022GL101802, <https://doi.org/10.1029/2022GL101802>, 2023.

1825 ~~Saavedra, F. A., Kampf, S. K., Fassnacht, S. R., and Sibold, J. S.: A snow climatology of the Andes Mountains from MODIS snow cover data, *International Journal of Climatology*, 37, 1526-1539, <https://doi.org/10.1002/joc.4795>, 2017.~~

~~Sandholt, I., Rasmussen, K., and Andersen, J.: A simple interpretation of the surface temperature/vegetation index space for assessment of surface moisture status, *Remote Sensing of environment*, 79, 213-224, [https://doi.org/10.1016/S0034-4257\(01\)00274-7](https://doi.org/10.1016/S0034-4257(01)00274-7), 2002.~~

1830 Schiffer, R. A. and Rossow, W. B.: The International Satellite Cloud Climatology Project (ISCCP): The first project of the world climate research programme, *Bulletin of the American Meteorological Society*, 64, 779-784, <https://doi.org/10.1175/1520-0477-64.7.779>, 1983.

Schmeisser, L., Hinkelman, L. M., and Ackerman, T. P.: Evaluation of radiation and clouds from five reanalysis products in the northeast Pacific Ocean, *Journal of Geophysical Research: Atmospheres*, 123, 7238-7253, <https://doi.org/10.1029/2018JD028805>, 2018.

1835 ~~Seinfeld, J. H., Bretherton, C., Carslaw, K. S., Coe, H., DeMott, P. J., Dunlea, E. J., Feingold, G., Ghan, S., Guenther, A. B., and Kahn, R.: Improving our fundamental understanding of the role of aerosol-cloud interactions in the climate system, *Proceedings of the National Academy of Sciences*, 113, 5781-5790, <https://doi.org/10.1073/pnas.1514043113>, 2016.~~

1840 ~~Shao, Y., Klose, M., and Wyrwoll, K. H.: Recent global dust trend and connections to climate forcing, *Journal of Geophysical Research: Atmospheres*, 118, 11,107-111,118,~~

<https://doi.org/10.1002/jgrd.50836>, 2013.

1845 [Shi, L., Zhang, J., Yao, F., Zhang, D., and Guo, H.: Drivers to dust emissions over dust belt from 1980 to 2018 and their variation in two global warming phases, *Science of The Total Environment*, 767, 144860, <https://doi.org/10.1016/j.scitotenv.2020.144860>, 2021.](#)
[Shikwambana, L., Xongo, K., Mashalane, M., and Mhangara, P.: Climatic and Vegetation Response Patterns over South Africa during the 2010/2011 and 2015/2016 Strong ENSO Phases, *Atmosphere*, 14, 416, <https://doi.org/10.3390/atmos14020416>, 2023.](#)

1850 Stengel, M., Stapelberg, S., Sus, O., Finkensieper, S., Würzler, B., Philipp, D., Hollmann, R., Poulsen, C., Christensen, M., and McGarragh, G.: Cloud_cci Advanced Very High Resolution Radiometer post meridiem (AVHRR-PM) dataset version 3: 35-year climatology of global cloud and radiation properties, *Earth System Science Data*, 12, 41-60, <https://doi.org/10.5194/essd-12-41-2020>, 2020.

1855 Stephens, G. L., O'Brien, D., Webster, P. J., Pilewski, P., Kato, S., and Li, J.-I.: The albedo of Earth, *Reviews of Geophysics*, 53, 141-163, <https://doi.org/10.1002/2014rg000449>, 2015.

Stephens, G. L., Hakuba, M. Z., Kato, S., Gettelman, A., Dufresne, J.-L., Andrews, T., Cole, J. N., Willen, U., and Mauritsen, T.: The changing nature of Earth's reflected sunlight, *Proceedings of the Royal Society A*, 478, 20220053, <https://doi.org/10.1098/rspa.2022.0053>, 2022.

1860 Su, W., Corbett, J., Eitzen, Z., and Liang, L.: Next-generation angular distribution models for top-of-atmosphere radiative flux calculation from CERES instruments: Methodology, *Atmospheric Measurement Techniques*, 8, 611-632, <https://doi.org/10.5194/amt-8-611-2015>, 2015.

Sus, O., Stengel, M., Stapelberg, S., McGarragh, G., Poulsen, C., Povey, A. C., Schlundt, C., Thomas, G., Christensen, M., and Proud, S.: The Community Cloud retrieval for CLimate (CC4CL)–Part 1:<?xmltex\break?> A framework applied to multiple satellite imaging sensors, *Atmospheric Measurement Techniques*, 11, 3373-3396, <https://doi.org/10.5194/amt-11-3373-2018>, 2018.

[Tang, Z., Tian, J., Zhang, Y., Zhang, X., Zhang, J., Ma, N., Li, X., and Song, P.: Anthropogenic aerosols dominated the decreased solar radiation in eastern China over the last five decades, *Journal of Cleaner Production*, 380, 135150, <https://doi.org/10.1016/j.jclepro.2022.135150>, 2022.](#)

1870 [Tao, M., Wang, L., Chen, L., Wang, Z., and Tao, J.: Reversal of aerosol properties in Eastern China with rapid decline of anthropogenic emissions, *Remote Sensing*, 12, 523,](#)

<https://doi.org/10.3390/rs12030523>, 2020.

[Trollet, M., Walawender, J. P., Bourlès, B., Boilley, A., Trentmann, J., Blanc, P., Lefèvre, M., and Wald, L.: Downwelling surface solar irradiance in the tropical Atlantic Ocean: a comparison of re-analyses and satellite-derived data sets to PIRATA measurements, *Ocean Science*, 14, 1021-1056, <https://doi.org/10.5194/os-14-1021-2018>, 2018.](#)

Verlinden, K. L., Thompson, D. W., and Stephens, G. L.: The three-dimensional distribution of clouds over the Southern Hemisphere high latitudes, *Journal of Climate*, 24, 5799-5811, <https://doi.org/10.1175/2011JCLI3922.1>, 2011.

Voigt, A., Stevens, B., Bader, J., and Mauritsen, T.: The observed hemispheric symmetry in reflected shortwave irradiance, *Journal of Climate*, 26, 468-477, <https://doi.org/10.1175/JCLI-D-12-00132.1>, 2013.

Voigt, A., Stevens, B., Bader, J., and Mauritsen, T.: Compensation of hemispheric albedo asymmetries by shifts of the ITCZ and tropical clouds, *Journal of Climate*, 27, 1029-1045, <https://doi.org/10.1175/JCLI-D-13-00205.1>, 2014.

Von Schuckmann, K., Palmer, M., Trenberth, K. E., Cazenave, A., Chambers, D., Champollion, N., Hansen, J., Josey, S., Loeb, N., and Mathieu, P.-P.: An imperative to monitor Earth's energy imbalance, *Nature Climate Change*, 6, 138-144, <https://doi.org/10.1038/NCLIMATE2876>, 2016.

~~[Wang, G. and Cai, W.: Two year consecutive concurrences of positive Indian Ocean Dipole and Central Pacific El Niño preconditioned the 2019/2020 Australian “black summer” bushfires, *Geoscience Letters*, 7, 1-9, <https://doi.org/10.1186/s40562-020-00168-2>, 2020.](#)~~

~~[Waliser, D. E. and Gautier, C.: A satellite-derived climatology of the ITCZ, *Journal of climate*, 6, 2162-2174, \[https://doi.org/10.1175/1520-0442\\(1993\\)006<2162:ASDCOT>2.0.CO;2\]\(https://doi.org/10.1175/1520-0442\(1993\)006<2162:ASDCOT>2.0.CO;2\), 1993.](#)~~

Wang, Y., Huang, X., Liang, H., Sun, Y., Feng, Q., and Liang, T.: Tracking snow variations in the Northern Hemisphere using multi-source remote sensing data (2000–2015), *Remote Sensing*, 10, 136, <https://doi.org/10.3390/rs10010136>, 2018.

Wang, Y., Wang, M., Zhang, R., Ghan, S. J., Lin, Y., Hu, J., Pan, B., Levy, M., Jiang, J. H., and Molina, M. J.: Assessing the effects of anthropogenic aerosols on Pacific storm track using a multiscale global climate model, *Proceedings of the National Academy of Sciences*, 111, 6894-6899, <https://doi.org/10.1073/pnas.1403364111>, 2014.

- 1900 Wielicki, B. A., Barkstrom, B. R., Harrison, E. F., Lee III, R. B., Smith, G. L., and Cooper, J. E.: Clouds and the Earth's Radiant Energy System (CERES): An earth observing system experiment, *Bulletin of the American Meteorological Society*, 77, 853-868, [https://doi.org/10.1175/1520-0477\(1996\)077<0853:CATERE>2.0.CO;2](https://doi.org/10.1175/1520-0477(1996)077<0853:CATERE>2.0.CO;2), 1996.
- 1905 Wielicki, B. A., Wong, T., Loeb, N., Minnis, P., Priestley, K., and Kandel, R.: Changes in Earth's albedo measured by satellite, *Science*, 308, 825-825, <https://doi.org/10.1126/science.1106484>, 2005.
- [Wright, J. S., Sun, X., Konopka, P., Krüger, K., Legras, B., Molod, A. M., Tegtmeier, S., Zhang, G. J., and Zhao, X.: Differences in tropical high clouds among reanalyses: origins and radiative impacts, *Atmospheric Chemistry and Physics*, 20, 8989-9030, <https://doi.org/10.5194/acp-20-8989-2020>, 2020.](https://doi.org/10.5194/acp-20-8989-2020)
- 1910 Xiao, Y., Ke, C.-Q., Shen, X., Cai, Y., and Li, H.: What drives the decrease of glacier surface albedo in High Mountain Asia in the past two decades?, *Science of The Total Environment*, 863, 160945, <https://doi.org/10.1016/j.scitotenv.2022.160945>, 2023.
- [Yang, K., Wang, Z., Luo, T., Liu, X., and Wu, M.: Upper troposphere dust belt formation processes vary seasonally and spatially in the Northern Hemisphere, *Communications Earth & Environment*, 3, 24, <https://doi.org/10.1038/s43247-022-00353-5>, 2022.](https://doi.org/10.1038/s43247-022-00353-5)
- 1915 Yang, X., Zhao, C., Yang, Y., and Fan, H.: Long-term multi-source data analysis about the characteristics of aerosol optical properties and types over Australia, *Atmospheric Chemistry and Physics*, 21, 3803-3825, <https://doi.org/10.5194/acp-21-3803-2021>, 2021.
- ~~[Yang, Y., Zhao, C., and Fan, H.: Spatiotemporal distributions of cloud properties over China based on Himawari 8 advanced Himawari imager data, *Atmospheric Research*, 240, 104927, <https://doi.org/10.1016/j.atmosres.2020.104927>, 2020.](https://doi.org/10.1016/j.atmosres.2020.104927)~~
- 1920 Yao, B., Liu, C., Yin, Y., Liu, Z., Shi, C., Iwabuchi, H., and Weng, F.: Evaluation of cloud properties from reanalyses over East Asia with a radiance-based approach, *Atmospheric Measurement Techniques*, 13, 1033-1049, <https://doi.org/10.5194/amt-13-1033-2020>, 2020.
- 1925 Young, A. H., Knapp, K. R., Inamdar, A., Hankins, W., and Rossow, W. B.: The international satellite cloud climatology project H-Series climate data record product, *Earth System Science Data*, 10, 583-593, <https://doi.org/10.5194/essd-10-583-2018>, 2018.

- 1930 [Yu, H., Yang, Y., Wang, H., Tan, Q., Chin, M., Levy, R. C., Remer, L. A., Smith, S. J., Yuan, T., and Shi, Y.: Interannual variability and trends of combustion aerosol and dust in major continental outflows revealed by MODIS retrievals and CAM5 simulations during 2003–2017, *Atmospheric Chemistry and Physics*, 20, 139-161, <https://doi.org/10.5194/acp-20-139-2020>, 2020.](#)
- 1935 [Zhang, R., Li, G., Fan, J., Wu, D. L., and Molina, M. J.: Intensification of Pacific storm track linked to Asian pollution, *Proceedings of the National Academy of Sciences*, 104, 5295-5299, <https://doi.org/10.1073/pnas.0700618104>, 2007.](#)
- Zhang, Y., Rossow, W. B., Laciš, A. A., and Oinas, V.: Calculation, evaluation and application of long-term, global radiative flux Datasets at ISCCP: Past and present, in: *Studies of Cloud, Convection and Precipitation Processes Using Satellite Observations*, World Scientific, 151-177, https://doi.org/10.1142/9789811256912_0009, 2023.
- 1940 [Zhao, B., Jiang, J. H., Gu, Y., Diner, D., Worden, J., Liou, K.-N., Su, H., Xing, J., Garay, M., and Huang, L.: Decadal-scale trends in regional aerosol particle properties and their linkage to emission changes, *Environmental Research Letters*, 12, 054021, <https://doi.org/10.1088/1748-9326/aa6cb2>, 2017.](#)
- 1945 [Zhao, C., Chen, Y., Li, J., Letu, H., Su, Y., Chen, T., and Wu, X.: Fifteen year statistical analysis of cloud characteristics over China using Terra and Aqua Moderate Resolution Imaging Spectroradiometer observations, *International Journal of Climatology*, 39, 2612–2629, <https://doi.org/10.1002/joc.5975>, 2019.](#)
- [Zhao, Y., Xin, Z., and Ding, G.: Spatiotemporal variation in the occurrence of sand-dust events and its influencing factors in the Beijing-Tianjin Sand Source Region, China, 1982–2013, *Regional environmental change*, 18, 2433-2444, <https://doi.org/10.1007/s10113-018-1365-z>, 2018.](#)
- 1950 [Zhao, Y., Li, J., Zhang, L., Deng, C., Li, Y., Jian, B., and Huang, J.: Diurnal cycles of cloud cover and its vertical distribution over the Tibetan Plateau revealed by satellite observations, reanalysis datasets, and CMIP6 outputs, *Atmospheric Chemistry and Physics*, 23, 743–769, <https://doi.org/10.5194/acp-23-743-2023>, 2023.](#)
- 1955 [Zhao, Y., Zhao, Y., Li, J., Wang, Y., Jian, B., Zhang, M., and Huang, J.: Evaluating cloud radiative effect from CMIP6 and two satellite datasets over the Tibetan Plateau based on CERES observation, *Climate Dynamics*, 1-20, <https://doi.org/10.1007/s00382-021-05991-7>, 2022.](#)
- [Zhou, Q., Chen, D., Hu, Z., and Chen, X.: Decompositions of Taylor diagram and DISO performance criteria, *International Journal of Climatology*, 41, 5726-5732, <https://doi.org/10.1002/joc.7149>,](#)

2021.

[Zhou, Y., Wu, T., Zhou, Y., Zhang, J., Zhang, F., Su, X., Jie, W., Zhao, H., Zhang, Y., and Wang, J.: Can global warming bring more dust?, *Climate dynamics*, 61, 2693-2715, <https://doi.org/10.1007/s00382-023-06706-w>, 2023.](#)

1960